Spring 2014

Development of a NURBS-based particulate dynamics framework for modeling circulating cells

Venkat Keshav Chivukula
University of Iowa

DEVELOPMENT OF A NURBS-BASED PARTICULATE DYNAMICS FRAMEWORK FOR MODELING CIRCULATING CELLS

by

Venkat Keshav Chivukula

A thesis submitted in partial fulfillment
of the requirements for the Doctor of
Philosophy degree in Biomedical Engineering
in the Graduate College of
The University of Iowa

May 2014

Thesis Supervisor: Assistant Professor Sarah C. Vigmostad

Graduate College
The University of Iowa
Iowa City, Iowa

CERTIFICATE OF APPROVAL

_____

PH.D. THESIS

_____

This is to certify that the Ph.D. thesis of

Venkat Keshav Chivukula

has been approved by the Examining Committee
for the thesis requirement for the Doctor of Philosophy
degree in Biomedical Engineering at the May 2014 graduation.

Thesis Committee: _____
Sarah C. Vigmostad, Thesis Supervisor

_____
HS Udaykumar

_____
Jia Lu

_____
Michael Henry

_____
ML Raghavan

_____
Edward Sander

To Tata and Avva

The more you know, the more you know you don't know

Aristotle

ACKNOWLEDGMENTS

This dissertation marks the culmination of my three and a half year journey in Iowa City. It is said that every day is a learning experience in life, and that could not be farther from the truth during my journey. However, these values and lessons would not have been properly assimilated and identified if it were not for the guidance and support of my advising committee and my fantastic colleagues in 2424 SC. Dr.HS Udaykumar was instrumental in guiding and encouraging me for the entire duration of my stay. Dr. Jia Lu provided me with a platform to communicate effectively and learn by asking the right questions in the quest for determining the path to be taken. The continued encouragement from Dr.Raghavan buoyed my enthusiasm for research, while the conversations with Dr.Sander proved extremely insightful. Dr.Henry was a constant source of energy, encouragement and enthusiasm for the experimental project. In addition, I was blessed to have the support, guidance and constant communication from Dr.Sarah Vigmostad. Her support and guidance was unparalleled.

I would also like to take this opportunity to thank Dr.KB Chandran, without whose support and encouragement I would not have been able to come to Iowa City and embark upon my PhD. I would also like to thank my lab mates John Mousel, Seth Dillard, Vishwanath Somashekar, Mehrdad Farahani, Anil Kapahi, Nirmal Rai, Oishik Sen, Ehsan, Liza Shrestha and Piyusha Gade for making my journey memorable and full of fun. I would also like to thank my family for their unwavering support and encouragement and their immense presence in my life everyday despite being halfway around the world. A special note of gratitude goes to my grandparents, who shaped my childhood and without whom I would not be the person I am today. Last but not the least, I would like to extend my deepest gratitude to my wife Deepti Jain for tolerating me and bearing with me for the past six years, all while successfully traversing the path to a PhD herself. And of course, my thanks to God for making everything possible.

ABSTRACT

The objective of this work is to develop a novel 3-D biological particulate dynamics framework to simulate blood flow in the micro circulation. This entails the amalgamation of concepts from various fields namely blood flow dynamics, solid mechanics, fluid-structure interaction and computational data structures. It is envisioned that this project will serve as a harbinger for implementing a multi-scale simulation model with applications in a vast array of situations from blood flows in heart valves to studying cancer metastasis. The primary motivation for this work stems from the need for establishing a simple, effective and holistic framework for performing blood flow simulations, taking into account the extremely 3-D nature of flow, the particle interactions and fluid structure interaction between blood and its constituent elements. Many current models to simulate blood cells rely on finite element methods which render large scale simulations extremely computationally intensive. The development of a framework for simulating blood flow is tied together with achieving a framework for performing an investigation of cancer metastasis. Cancer initially develops at a primary site and spreads through the body to secondary sites using the circulatory systems of the body – the blood circulatory system and the lymphatic system. It is known that all the cancer cells that enter into the circulation do not survive the harsh environment, though the exact cause of this is still undetermined. Moreover, the mechanical properties of cancer cells are not well documented and appropriate computational models require that experiments be conducted to determine the same. Thus the end goal of this work is to establish a system to analyze and simulate 3-D blood particulate dynamics, including cancer cells, from a holistic standpoint in order to understand more about the phenomenon of blood flow as a whole, and cancer metastasis in particular.

TABLE OF CONTENTS

LIST OF TABLES

LIST OF FIGURES

CHAPTER 1

MOTIVATION

1.1 Introduction

The objective of this work is to develop a novel 3-D biological particulate dynamics framework to simulate blood flow in the micro circulation. This entails the amalgamation of concepts from various fields namely blood flow dynamics, solid mechanics, fluid-structure interaction and computational data structures. It is envisioned that this project will serve as a harbinger for implementing a multi-scale simulation model with applications in a vast array of situations from blood flows in heart valves to studying cancer metastasis. The primary motivation for this work stems from the need for establishing a simple, effective and holistic framework for performing blood flow simulations, taking into account the extremely 3-D nature of flow, the particle interactions and fluid structure interaction between blood and its constituent elements. Many current models to simulate blood cells rely on finite element methods which render large scale simulations extremely computationally intensive. The development of a framework for simulating blood flow is tied together with achieving a framework for performing an investigation of cancer metastasis. Cancer initially develops at a primary site and spreads through the body to secondary sites using the circulatory systems of the body – the blood circulatory system and the lymphatic system. It is known that all the cancer cells that enter into the circulation do not survive the harsh environment, though the exact cause of this is still undetermined. Moreover, the mechanical properties of cancer cells are not well documented and appropriate computational models require that experiments be conducted to determine the same. Thus the end goal of this work is to establish a system to analyze and simulate 3-D blood particulate dynamics, including cancer cells, from a holistic standpoint in order to understand more about the phenomenon of blood flow as a whole, and cancer metastasis in particular.

1.2 Blood and its constituents – a brief overview

The purpose of blood is provide oxygen and nutrients to and remove waste products from all parts of the body; it achieves this immense task by circulating through the heart to arteries, arterioles, capillaries, venules, veins and finally back to the heart. From the heart the deoxygenated blood is sent to the lungs where it releases carbon dioxide and absorbs oxygen, following which it returns to the heart from where it is circulated to all parts of the body through the aforementioned loop. Blood is not a homogeneous fluid, but a suspension of primarily three types of particulates – red blood cells (RBC) or erythrocytes, white blood cells (WBC) or leukocytes and platelets or thrombocytes. They each have their own unique function, and together form a highly efficient ecosystem, performing multiple functions such as delivering nutrients, removing wastes and protecting the circulatory pathways along with combating infections. These particulates together are called formed elements, and they are suspended in a fluid called plasma. More than 95% of blood particulates are RBCs [1]. The formed elements together constitute about 45% of the blood, while plasma contributes towards approximately 55%. The leukocytes and platelets make up 4% of the cells in the circulatory system. Plasma is about 90% water and contains three major proteins – albumin, fibrinogen and globulin. Plasma can be assumed to be a Newtonian fluid with a viscosity of 1.2 cP at normal blood temperature [2], however blood itself cannot be thought of as Newtonian due to its extremely high density particulate nature.

The typical shape of a RBC is biconcave while the WBC and platelets can be assumed to be spheroids, though the platelet is considerably smaller than either a RBC or a [1]. An image of a RBC, a platelet and a WBC is shown in Figure 1-1. The RBC, as described above is a biconcave disk with a diameter of around 8μ and a thickness of around 2μ. The WBC can vary from having a spheroid shape of around 8 μ in diameter to 16 μ in diameter. The platelet is typically around 2 μ in diameter, and is considered to be a spheroid for all practical purposes in this work. The amount of blood cells in a given

volume is given by its hematocrit, and as mentioned earlier, RBCs make up about 45% by volume of a given sample of fluid. Knowing that the typical human has about 5.5 Litres of blood in the body, this amounts to about 3.5 Litres comprised of RBCs alone. Thus there are roughly about 2.5×10^{13} RBCs in the human body at any given point of time. This corresponds to over a million blood cells in one drop of human blood [1]. These RBCs traverse through circulatory pathways ranging from O(cm) – arteries to O(μm) – capillaries; i.e. they traverse though pathways that are three orders of magnitude apart, all in a span of a couple of minutes. Due to this extreme nature of travel of the RBC in the circulatory system, investigating the nature of blood flow is both extremely important and extremely challenging. A brief review of blood flow research will be given in the next chapter.

1.3 The mechanisms of cancer metastasis – an overview

Cancer is extremely dangerous primarily due to its ability to spread (metastasize) to secondary locations through the process of metastasis. A common school of thought about the initialization of metastasis is the seed and soil theory proposed by Paget[3], where it was proposed that cancer cells – the seed- will metastasize under specific conditions depending on the surrounding organs – the soil. Despite being proposed in 1889, Paget's theory is still considered to be a viable explanation, though additional explanations have been proposed which relate metastasis with mechanical loading conditions of the tissue surrounding the site of primary cancer. Once a cancer is initiated at a primary site, various mechanisms are set into motion which lead to its growth, proliferation and ultimately its spread to secondary locations. The major steps in cancer metastasis (shown in Figure 1-2) are as follows:

1. Primary Tumor: This is the stage where the tumor initiates and starts growing at a primary site.

2. Proliferation and Angiogenesis: The tumor begins to spread and this requires a supply of more nutrients, which are obtained by the formation of new blood vessels (vascularization).
3. Detatchment: The now proliferated tumor spreads and moves towards a point of entry into the circulation – both lymphatic and blood circulation are pathways. Lymphatic channels and thin walled venules provide the least resistance to the invading tumors.
4. Circulation and transport: After gaining access to the circulatory system, the tumors now circulate, interacting with the elements in the blood circulation – namely platelets, red blood cells, lymphocytes, etc. These circulating tumor cells are transported through the body via the circulatory system.
5. Extravasation: Tumor cells adhere to vessel walls and undergo extravasation – they move from the circulatory system into the tissue surrounding the circulatory vessels.
6. Proliferation into secondary sites: The tumor cells now establish a conducive environment and lead to further angiogenesis, thereby completing the metastasis process.

The focus of the current work for investigating cancer metastasis is Step 4 where the cancer cells traverse the circulation to spread to secondary areas.

1.4 Objectives

This work consists of both experimental and computational aspects. The computational aspect involves development of a framework for novel 3-D modeling of blood particulates. The experiments seek to investigate and characterize the response of epithelial prostate cancer cells to mechanical stimuli, while simultaneously seeking to provide material property values to be used in the aforementioned simulations.

This research will address the following objectives:

OBJ-I. To develop and validate a modeling approach that efficiently captures the complexities of individual blood cell dynamics

OBJ-II. To characterize the material properties of epithelial cancer cells in order to model ensembles of cancer cells along with blood cells

OBJ-III. To implement a cost-effective framework that captures the interactions of multiple cells

OBJ-IV. To determine how cancer cell properties impact their behavior in the circulation

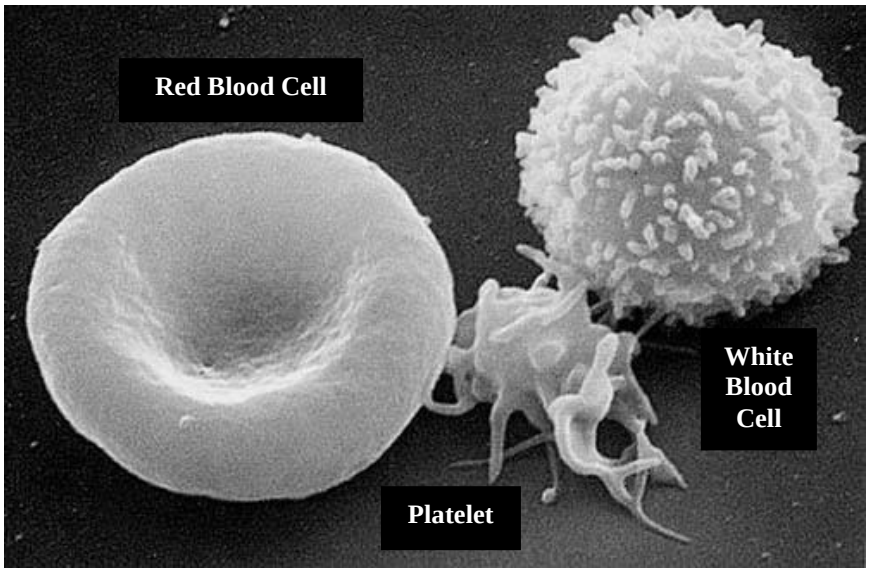

Figure 1-1: Scanning Electron Microscope image of a Red Blood Cell, Platelet and White Blood Cell showing the different morphologies for each. The Red Blood Cell is biconcave in shape while the White Blood Cell ranges from being spherical to highly irregular. The platelet changes its shape based on its level of activation. (Electron Microscopy Facility at the National Cancer Institute at Frederick)

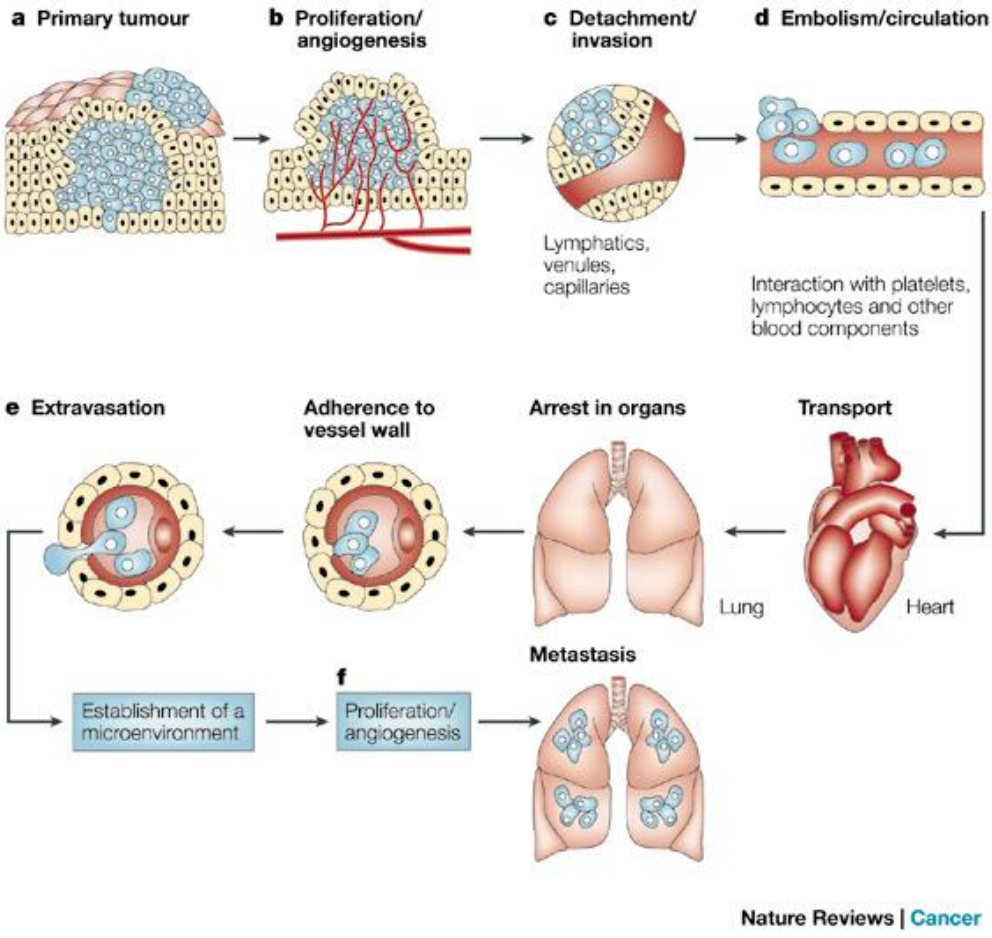

Figure 1-2: Steps involved in cancer metastasis[4]. One of the objectives of this research is to investigate cancer metastasis (d) when the cancer cells enter the circulation and interact with other cells in the blood to gain more knowledge about the physics of cancer.

CHAPTER 2

NOVEL MODELING OF INDIVIDUAL BLOOD CELLS

2.1 Introduction

Human blood is a suspension of particulates – mainly red blood cells, white blood cells and platelets. The behavior of blood at the visible scale (hereafter called the macro-scale) is a manifestation of the intricate interaction of blood particulates at the particulate scale (hereafter called micro-scale). Thus in order to more realistically simulate the behavior of blood, the particulate nature of blood has to be acknowledged. However, achieving physiologically realistic simulations is non-trivial, as a single drop of blood contains in excess of 1 million particulates [1]. Over the past few decades, researchers have employed various methodologies to simulate blood, with the methods spanning the spectrum from macro to micro-scale. A brief overview of past work in the field of micro-scale blood simulation is provided in the next section. The motivation for novel particulate models is then explained followed by a detailed description of the current modeling technique. The models are tested in benchmark cases and the chapter is concluded with a brief discussion on the utility of the proposed methodology for blood simulation.

2.2 Modeling and Simulating Blood : A Brief Review

2.2.1 Continuum Models (macro-scale)

Arteries in the human body range from *O(cm)* to *O(μm)*. This three-fold change in the magnitude of arteries through which blood flows entail different modeling philosophies. The simplest method of simulating blood flow is by assuming that it is a homogeneous fluid with constant properties (viz. density and viscosity). There have been multiple studies in the past that make the case for assuming blood to be Newtonian under

certain flow conditions [2,5,6]. However, as this research focuses on the micro-scale models of blood flow, the macro-scale models are not presented here.

2.2.2 Meso-Scale Models

The meso-scale models for blood cells focus on individual blood cells per se, but typically does not involve complete resolution of the RBC deformation. These models only strive to capture the general type of deformations the RBCs undergo, while attempting to achieve interaction between the cell and its surrounding fluid. Hence these models can be said to be precursors for completely resolved fluid structure interaction models of blood cells. These models are applicable in medium sized arteries (100μm - 500μm or so). Typical behavioral characteristics of the RBCs include flipping or tumbling and tank treading [7][8] .Moreover, blood at this size scale can no longer be approximated by a homogeneous fluid and the particulate nature of blood comes into play. One of the most significant phenomenon observed is the Fahraeus-Lindqvist effect [9]which is the migration of the RBCs away from the vessel walls and towards the central region while there exists a cell-free zone close to the arterial walls, thereby changing the apparent viscosity of blood in the tube.

Initial meso-scale simulations involving blood cells treated blood as rigid particles, as is the case of the study done by Sun and Munn in 2005 [10] They implemented a Lattice-Boltzmann model for RBCs which were approximated as rigid disks. The Fahraeus-Lindqvist effect was observed, and influence of the presence of a single white blood cell (WBC) on the 2-dimensional RBC dynamics was examined. The presence of a WBC significantly altered the flow dynamics due mainly to its large size compared to the RBCs. This alteration was more pronounced in approximations of smaller conduits than larger ones. It was also acknowledged that deformable WBCs should reduce the effect of the presence of a WBC in physiological conditions. Meso-scale simulations involving deformable RBCs in a 2-dimensional setting was performed

by Bagchi in 2007 [11]. In this study, the immersed boundary framework [12] was utilized without the use of a separate particle-interaction model for simulating up to 2500 cells. RBCs were modeled as deformable 2-dimensional elastic membrane encapsulated particles whose membrane mechanics was governed by the neo-Hookean law. The phenomenon of tumbling and tank treading were observed for simulations of individual cells. Simulations of multiple cells (upto 2500 cells) were performed under a parabolic flow profile and the formation of a cell-free layer was observed. Other studies have looked at the behavior of blood cells in both 2D and 3D [13] and have been able to capture the general flow dynamics for blood cells in arteries; however in order to study phenomena like thrombosis and cancer metastasis, resolving blood particulates in high fidelity becomes necessary so that the intricate and complex interactions and dynamics can be captured.

2.2.3 Micro-scale Models

The particulate behavior of blood is best understood by simulating the actual RBCs with high fidelity – i.e. with enough resolution so as to capture not only the RBC deformation but also the effect of the deformation on the surrounding fluid. This is important to achieve a better understanding of the fluid-structure interaction problem at hand.

An example of a 2-dimensional of micro-scale simulation is the study by AlMomani et al in 2008 [14] where the RBCs and platelets were modeled as elliptical pseudo-rigid particles and spherical rigid particles respectively in a 2-dimensional framework. Here, particle-particle interactions were factored in and a fluid-structure interaction problem was solved using the level set method initially introduced by Sethian [15] coupled with the immersed boundary method introduced by Peskin [12]. Tendencies of RBCs to migrate towards the central core and for platelets to migrate towards the wall were observed. This study was important in that although the particles were not fully

deformable and the study was 2-dimensional, both RBCs and platelets interacting with the fluid were simulated.

While 2-dimensional simulations are a good early step in investigating blood flow, it is only the 3-dimensional simulations that would ultimately lead to a better understanding of the particulate nature of blood. This is because blood is a suspension of different kinds of particles such as red blood cells, platelets, white blood cells, etc as mentioned earlier; the interaction of all these particles is extremely 3-dimensional in nature. As mentioned before, blood vessels vary from *O(cm)* to *O(μm),* hence the nature of deformation of the blood constituents become more extreme in the smaller arterioles and capillaries, which would need high-fidelity models. However, simulating the deformation of even a single RBC in a 3-dimensional realm proved extremely challenging, as evidenced by the numerous studies attempted [16–22] and the numerous methods to do so developed over the past few decades [16,18,23–27].

The basic approach to 3-dimensional modeling of RBCs began with modeling RBCs as barely deformable spherical or elliptical membrane-encapsulated capsules [28][29]. The membrane was initially modeled as elastic in nature with viscous effects being included in later models. Deformation of the capsules were modeled using perturbation methods in linear Stokes flow (very low Reynolds number). Despite the simplicity of the model and the restriction in flow conditions, some phenomenon such as tank treading was observed. Around the same time, in 1977, Peskin [12] introduced the Immersed Boundary Method(IBM) which was an effective method to treat the fluid as an Eulerian entity and any immersed solid such as a heart valve or a RBC as a Lagrangian entity, with communication between the two occurring in the transfer of velocities from Eulerian to the Lagrangian mesh and forces being transferred in the reverse direction. Multiple attempts at using the IBM for performing 3-dimensional simulations were made. Eggleton in 1998 [30] performed simulations for a capsule model (as explained above) in simple shear flow using various constitutive laws for the behavior of the elastic

membrane. Bagchi followed his 2-dimensional study with a 3-dimensional study in 2009 [31] which modeled RBCs as 3-dimensional, fully deformable particles governed by the Neo-Hookean membrane law. Additional studies were published which simulated high resolution deformations for single cells using the IBM framework by Pozrikidis in 2003 [21]. All of the above studies used the finite element method (FEM) for modeling blood cells. Advancement in computational power has led to more 3-D simulations over the past decade [31,32]; however achieving physiologically realistic simulations of large systems of multiple deformable blood-borne cells, especially in the highly dynamic environment of the microcirculation is still a challenge [23]. Recent advances in modeling RBCs include the development of the Immersed Finite Element Method (IFEM) in around 2004 by Zhang et al [33]. It was a modified version of the IBM in that the solid (Lagrangian) mesh actually occupied volume in the fluid grid. In 2005, Zhang et al presented the application of the IFEM towards simulating a small number of RBCs in shear flows and in flow inside an arteriole. In 2010, Dodson and Dimitrakopoulos [34] published their work on simulating erythrocytes using a cytoskeleton based continuum model. They modified the well-known Skalak law [35] by including a localized adaptive pre-stress parameter which allowed local area dilatation but prohibited global area dilatation in the membrane behavior of the RBC. Kloppel and Wall in 2011 [36] proposed a hybrid model comprised of both the lipid bilayer and the spectrin cytoskeleton underneath. They modeled the effect of the aforementioned components by introducing a combination of two materials along the thickness – an upper element representing the lipid bilayer and the lower element representing the cytoskeleton. The behavior of the cell was a result of the combined response of both the materials models. The studies mentioned in this paragraph highlight the advances being made in the field of single and multiple RBC simulations in a 3-dimensional framework.

2.3 Proposed Modeling Approach

Over the years, barring a few exceptions [21,37], the vast majority of blood particulate models at the micro-scale were FEM based, which required the use of *O(1000)* – or more often *O(10,000)* elements [30–32,38] for a single cell. This makes the calculations highly computationally intensive, especially when attempting to simulate multiple cells. Furthermore, most FEM approaches use lower-order elements, which negatively affect accuracy [39]. In the current approach, a novel method is proposed for the modeling and analysis of RBC dynamics at the micro-scale using the power of isogeometric modeling and analysis, specifically using Non-Uniform Rational B-Splines (NURBS). The underlying principle is based on the well-known B-splines, but allows far greater ability to model and deform an entity [40,41]. Moreover, we invoke the concept of isogeometric analysis which has proven to be a powerful tool in the realm of biological applications [42–44]. This combination provides us with a novel method to both model and analyze the deformation of RBCs in the human circulation. Through NURBS-based modeling we can represent a geometrically accurate model and perform stress analysis using the same geometric framework. Additionally, due to the inherent geometric smoothness of the NURBS representation, models can be simulated using relatively few elements as compared with traditional FEM-based methods. For instance, a circle (in 2D) can be represented using as few as four surface points using a quadratic NURBS curve [40]. Moreover, NURBS possesses an inherent advantage for contact and particle interactions, which lends itself as an ideal candidate for simulating blood flow dynamics of individual cells [45–48]. While NURBS has been used extensively in the CAD community, it is only in the past decade that it has found applications in the biomedical field [42,43,49]. While attempts have been made to apply the principle of isogeometric modeling to describe spherical cells [37], to the best knowledge of the authors, this is the first attempt to apply NURBS modeling to biological cells, especially biconcave cells in 3-D. This framework is generic in nature, and can be applied to modeling blood-borne

particulates of various shapes, for future applications of simulating flows with multiple types of particulates.

2.4 NURBS Background and Overview of Geometric Modeling using Isogeometric Principles

2.4.1 Knot Vectors

NURBS are composed primarily of B-Splines, which in turn are built up from knot vectors. A knot vector is a means of denoting specific points along the parameteric direction. Any curve can be described by points on the curve either in Cartesian space or in parameteric space (along the curve). It is essentially a set of co-ordinates in the parameteric space, composed of individual values called "knots". $U = \{u_0, u_1, \dots, u_m\}$ is the *knot vector* which is a nondecreasing sequence of real numbers $u_i \leq u_{i+1}, i = 0, \dots, m-1$. The u_i are called *knots*. These form the building blocks of B-splines and consequently, NURBS. The basic idea behind knots in parameteric space is shown in Figure 2-1, where s is a co-ordinate measured along the curve and takes on the values from 0.0 at the beginning of the curve till 1.0 at the end of the curve. The curve can also be represented along the traditional Cartesian x-direction where, for instance, it spans 10 units. One of the most commonly used parameterisations is that of a circle, where any point on a circle is represented by a traditional (x,y) pair and also with a polar (r,θ) pair.

2.4.2 B-Spline Basis Functions

The knot values in the knot vector described earlier form the building blocks for basis functions. Basis functions, or blending functions as they are more commonly known are used to smoothly blend functions across a set of points. These blending functions can be of different degrees, based on requirement. The first order (or 0-degree) blending functions are simply step functions which either take on the values 0 if consecutive knot values are the same, or 1 if consecutive knot values are different. Blending functions of

higher orders are constructed from the 0-degree blending functions. Any blending function at a particular point i of degree p is denoted by $N_{i,p}$. As these functions are always associated at a knot point with a specific value of the knot, u, B-Spline Basis functions denoted as $N_{i,p}(u)$ which describes an i-th basis function N of degree p at the point u. $N_{i,p}(u)$ is defined as:

$$N_{i,0}(u) = \begin{cases} 1 & if\ u_i \leq u < u_{i+1} \\ 0 & otherwise \end{cases} \tag{2.1}$$

$$N_{i,p}(u) = \frac{u - u_i}{u_{i+p} - u_i} N_{i,p-1}(u) + \frac{u_{i+p+1} - u}{u_{i+p+1} - u_{i+1}} N_{i+1,p-1}(u) \tag{2.2}$$

Here, $N_{i,0}(u)$ is a step function which is unity only on the half open interval $u \in [u_i, u_{i+1})$. For degree $p > 0$, the basis functions are simply linear combinations of two (p-1)-degree basis functions. This is depicted in Figure 2-2 [39].

The basis functions are piecewise-polynomials, and there is a triangular dependence of basis functions as evident from the definition in (2.1), as is shown in Figure 2-2 [40]. The manner in which the knot vector U is defined has a profound impact on the values of the basis functions [40]. Note that the knot vector can have multiple knots of the same value, but U has to be a *non-decreasing* set of real numbers. The knot vector may be comprised of knots which are uniformly spaced or randomly spaced. The former is known as a "uniform" knot vector and the latter is called a "non-uniform" knot vector, or alternately periodic and non-periodic knot vectors. The derivatives of the B-Spline Basis functions can also be determined, and they are also linear combinations of the basis functions [40].

2.4.3 B-spline Curves and Surfaces

In order to describe a B-spline curve, it is necessary to have points in Cartesian space that denotes the nature of the curve. These points effectively "control" how a curve is described, and hence are called *control points*. With the aid of knots, basis functions

and control points, a B-spline curve can now be defined. A *p-th* degree B-spline curve is defined by

$$\boldsymbol{C}(u) = \sum_{i=0}^{n} N_{i,p}(u)\, \boldsymbol{P_i} \quad a \leq u \leq b \tag{2.3}$$

$$U = \{a, \dots, a, u_{p+1}, \dots, u_{m-p-1}, b, \dots, b\} \tag{2.4}$$

where $\{\boldsymbol{P_i}\}$ are the control points and the $\{ N_{i,p}(u) \}$ are the *p-th* degree B-spline basis functions defined in (2.2). Reiterating, $\{\boldsymbol{P_i}\}$ are called control points, as they control the shape of the curve. They may or may not lie directly on the curve – they simply provide a path for the curve to meander. The polygon formed by the set of control points is called the control polygon. A simple B-spline curve is shown in Figure 2-3.

The number of knots, the number of control points and the degree of the curve are enough to specify any B-spline curve and they are related by

$$m = n + p + 1 \tag{2.5}$$

where $m + 1$ is the number of knots, $n + 1$ is the number of control points and p is the degree of the B-spline entity.

The B-spline curves trace the general shape of the control polygon, with the distinct feature of local control: moving a specific control points will only affect the curve in the region $[\, u_i, u_{i+p+1} \,)$, as $N_{i,p} = 0$ when u does not belong to $[\, u_i, u_{i+p+1} \,)$. Furthermore, the same control polygon can yield very different curves, as shown in Figure 2-4. In the figure, the curve starts at control point $\boldsymbol{P_0}$ and ends at $\boldsymbol{P_4}$. The knots are in the parametric direction u along the curve; and as depicted, the control points do not lie on the actual curve, but rather forms the boundary (polygon) along which the curve exists. The logical extension of the B-spline curves are B-spline surfaces, which is essentially a tensor product of two one-dimensional B-spline basis functions in two parametric directions. It is worthwhile to note that the B-spline curves, and surfaces, are invariant under affine transformations.

2.4.4 NURBS Curves, Surfaces and Solids

The development of NURBS was motivated by the requirement to have higher levels of local control over the shape of the curve or surface as compared to simple B-spline curves and surfaces. The addition of weight factors in the basis function definition provided this added level of control, leading to the development of the Non-Uniform Rational B-spline (NURBS) family of curves and surfaces.

A *p-th* degree NURBS curve is defined by

$$\boldsymbol{C}(u) = \frac{\sum_{i=0}^{n} N_{i,p}(u)\, w_i\, \boldsymbol{P_i}}{\sum_{i=0}^{n} N_{i,p}(u)\, w_i} \quad a \leq u \leq b \tag{2.6}$$

$$U = \{a, \dots, a, u_{p+1}, \dots, u_{m-p-1}, b, \dots, b\} \tag{2.7}$$

Where the $\{\boldsymbol{P_i}\}$ are the control points as defined above, and the $w_i$are the weights ($w_i > 0$) – every control point has a weight associated with it. The knot vector definition remains the same. A concise way of defining the NURBS basis functions (also called rational basis functions because of the weights) is

$$R_{i,p}(u) = \frac{N_{i,p}(u)\, w_i}{\sum_{j=0}^{n} N_{j,p}(u)\, w_j} \tag{2.8}$$

$$\boldsymbol{C}(u) = \sum_{i=0}^{n} R_{i,p}(u)\ \boldsymbol{P_i} \tag{2.9}$$

The definition shown in (2.9) is analogous to the definition of B-spline curves in (2.3), in that the $R_{i,p}(u)$ replaces the B-spline basis functions. Though all the curves shown are the same cubic curve, modifying the weights associated with control point $\boldsymbol{P_3}$ results in dramatically different curves. Setting the weight of $\boldsymbol{P_3}$ to be 0 essentially negates the presence of that point in the formulation.

It is worthwhile to note that the same basic properties of the B-spline basis functions hold true for the NURBS basis functions as well; because the NURBS basis functions are just modified versions of the former. Another important property to be kept in mind is the partition of unity property :

$$\sum_{i=0}^{n} R_{i,p}(u) = 1 \; for\; all\; u \in [a, b] \tag{2.10}$$

Setting the weights $w_i = 1$ will result in the NURBS curves (2.8),(2.9) transforming into the B-spline curves in (2.3).The weights provide additional control over the shape of the curves, as mentioned earlier. Increasing the weights results in the curve approaching the control point associated with the weight. This will be made clearer in the following sections. Similar to the extension of B-spline curves to B-spline surfaces, the definition of NURBS curves is extended defining NURBS surfaces.

A NURBS surface of degree p in the u-direction and degree q in the v-direction is a piecewise rational function of the form

$$\boldsymbol{S}(u,v) = \frac{\sum_{i=0}^{n}\sum_{j=0}^{m} N_{i,p}(u)N_{j,q}(v)\, w_{i,j}\, \boldsymbol{P_{i,j}}}{\sum_{i=0}^{n}\sum_{j=0}^{m} N_{i,p}(u)N_{j,q}(v)\, w_{i,j}} \quad a \le u \le b\,, c \le v \le d \tag{2.11}$$

The $\{\boldsymbol{P_{i,j}}\}$ form a bi-directional control net (in 3-D space), and $\{\boldsymbol{w_{i,j}}\}$ are the weights associated with the control points. This definition can be simplified by introducing the piecewise rational basis functions as before:

$$R_{i,j}(u,v) = \frac{N_{i,p}(u)N_{j,q}(v)\, w_{i,j}}{\sum_{i=0}^{n}\sum_{j=0}^{m} N_{i,p}(u)N_{j,q}(v)\, w_{i,j}} \tag{2.12}$$

$$\boldsymbol{S}(u,v) = \sum_{i=0}^{n}\sum_{i=0}^{n} R_{i,j}(u,v)\ \boldsymbol{P_{i,j}} \tag{2.13}$$

A simple NURBS surface is shown in Figure 2-5.

The NURBS surfaces can be further extended into NURBS solids, which are basically tensor products of three one-dimensional basis functions. A NURBS surface of degree *p* in the *u*-direction, degree *q* in the *v*-direction and degree *r* in the *w*-direction is a piecewise rational function of the form

$$\boldsymbol{S}(u,v,w) = \frac{\sum_{i=0}^{n}\sum_{j=0}^{m}\sum_{k=0}^{l} N_{i,p}(u)N_{j,q}(v)\, N_{k,r}(w)\, W_{i,j,k}\, \boldsymbol{P_{i,j,k}}}{\sum_{i=0}^{n}\sum_{j=0}^{m}\sum_{k=0}^{l} N_{i,p}(u)N_{j,q}(v)\, N_{k,r}(w)\, W_{i,j,k}} \tag{2.14}$$

$$a \le u \le b\,, c \le v \le d, e \le w \le f \tag{2.15}$$

Here, $\{\boldsymbol{P_{i,j,k}}\}$ forms a tri-directional control net (in 3-D space) and $\{\boldsymbol{W_{i,j,k}}\}$ are the weights associated with the respective control points. The three dimensional parametric NURBS solid definition can also be cast in the concise form, similar to (2.13).

2.4.5 Creating NURBS Models of Red Blood Cells (RBC)

2.4.5.1 One-Dimensional RBC Model

A RBC is characterized by its biconcave discoid shape when at rest, as this shape provides for roughly 37% more surface area as compared to a sphere enclosing the same interior volume. This helps the RBC perform its oxygen and nutrient transport-exchange function very effectively, while also being able to undergo very large deformations in order to travel through the microcirculation while performing its functions. The NURBS curve model for the RBC cross section is shown in Figure 2-6. In Figure 2-6, the NURBS curve is shown in black. The blue dashed line is a representation of the bioncave shape using the equations defined in the paper by Pozrikidis on modeling RBCs [21]. The red points denote the locations of the control points, while the red polygon is the control polygon. As noted earlier, the control points need not lie on the actual curve, it only prescribes the direction and extent of the NURBS curve. There are 40 control points in all for the complete NURBS biconcave shape, and the curve is a cubic curve (i.e. degree = 3). The weights were all set equal to 1 for simplicity, and can be changed at any time in the model to effect a change in any given portion of the cell. The NURBS models (curve, surface and solids) were created in a NURBS geometric modeling software RHINOCEROS 4.0® (McNeel &Associates, Seattle,WA), hereafter abbreviates as RHINO, stored as an IGS file and were then read by an in-house developed FORTRAN program which extracted the NURBS data (control points, knot points, weights) and re-created the NURBS geometries for further modifications and interfacing with the fluid.

2.4.5.2 Two-Dimensional NURBS Model

The next step is to extend the 1-D NURBS model to a 2-D NURBS model. Note that the 1-D NURBS model is in the 2-D space in the traditional Cartesian sense. Similarly, the 2-D NURBS model is 3-D in the Cartesian space. The RBC model will have nodes and surface points in 3-D space with each point having a *(x,y,z)* co-ordinate

representation in the Cartesian space, while also simultaneously possessing a *(u,v)* co-ordinate representation in the NURBS space. The rendered 2-D NURBS RBC model is shown in Figure 2-7. This is a NURBS surface following the definition in equation (2.13), with two independent knot vectors U and V. Both the U and V directions are bi-cubic, and they have 25 and 17 knots respectively. The model is created by initially modeling one half of the NURBS curve shown in Figure 2-6 and rotating it 360 degrees to form a surface of rotation. The *knot mesh* which is formed by the intersection of the 2 knot lines is shown by black lines across the RBC surface. The wireframe image of only the knot mesh and the control points is shown in Figure 2-7(b), and the side view is shown in Figure 2-7(c). There are 273 control points for the RBC. The knot mesh gives rise to *knot elements*, of which there are 180. The intersection of the knot meshes in the U and the V directions are called nodes, and there are 209 total nodes including overlapping nodes. The number of independent nodes in the RBC model shown in figure 3 is 172.

As can be seen, there is a stark difference in the number of elements and nodes required to obtain a physiologically accurate representation of a RBC as compared to traditional finite element methods (FEM). This difference is highlighted in Figure 2-9, where the coarsest model created in this research, with 84 elements is compared with the finest model created with 6400 elements. Figure 2-8(a) shows the finest model with 6400 elements with the knots shown on the left and a smooth render on the right. Figure 2-8(b) shows the coarsest model with 84 elements with knots shown on the left and a smooth render on the right. This highlights one of the unique and novel features of this research – the same smoothness and accuracy can be obtained with as few as 84 elements or as fine as 6400 elements. Refining or coarsening the model does not impact the geometry of the model, unlike traditional methods (such as FEM) used to model RBCs like finite element method (FEM), where coarsening the model leads to a substantial loss in geometrical resolution. This is shown in Figure 2-9 where the coarsest model (84 elements) is shown

alongside finite element models obtained from [50] [51]. It can be clearly seen that in order to obtain a smooth representation, Mills et al.[51] used 23,867 elements.

2.4.5.3 Three-Dimensional RBC Model

The extension of the 2-D NURBS RBC model into the 3-D NURBS RBC model is straightforward in theory. However, creating a 3-D NURBS model requires some modifications and includes more than simple extrusion of a surface into a solid. 3-D NURBS solids require 3 knot vector directions – U,V along the surface and the W-direction perpendicular to the surface into the solid (along the thickness). Since the physiological structure of the RBC consists of a lipid bilayer membrane of finite thickness, it is necessary to re-create the membrane structure in RHINO for the 3-D NURBS model. For the creation of the NURBS solid, a two-step process was implemented. The first step comprised of creating a fixed number of layers, or 2-D NURBS surfaces depending on the degree of the W-direction NURBS connectivity desired. It was decided to incorporate a quadratic connectivity for the thickness direction, as this would provide the flexibility required for the deforming of the membrane. Keeping in mind the relation between the knots and degree of the connectivity desired, this elicited creating three 2-D NURBS surfaces from relation (2.13). This was done such that the nodes of all surfaces were in the direction of the surface normal at the node locations - the surface definition adhered to the preservation of the local normal at every node point. The thickness of the surfaces along the transverse direction to the membrane was decided based on the ratio of the physiological thickness of the lipid bilayer to the diameter. This ensured a physiologically accurate representation of the RBC. The 3-D NURBS RBC model is shown in Figure 2-10.

Figure 2-7 shows the side-view of the three surfaces comprising the RBC model. Figure 2-7(b) and Figure 2-7(c) show the enlarged view of the selected regions of the three layers in the transverse directions. This was then stored as in IGS file and was

supplied to the FORTRAN code. The second step of creating the 3-D NURBS solid occurs here in the FORTRAN code. The three surfaces are identified as inputs to a subroutine which has the quadratic knots stored for the W-direction. The solid is made one element thick – i.e. the element spans the thickness of the membrane. The three layers are required as input due to the quadratic element requirement as mentioned before. The number of layers would be different for elements of higher orders. Using the three surfaces as an input, along with the knot vector and the weights provided, the 3-D NURBS solid mesh is created. The number of elements stay the same as in the 2-D surface mesh – there are 180 elements that comprise the RBC. However, in the case of the 3-D NURBS solid, the elements are 3-D elements which have a *cubic x cubic x quadratic* nature. The number of control points triple to 819 control points (273 control points per layer). The U- and the V-direction knot vectors and weights remain the same as the 2-D case. The number of nodes also remain the same – 209 total nodes, 173 distinct nodes. Thus the 3-D RBC is comprised of 180 3-D elements and 172 nodes, shown in Figure 2-10. A flowchart depicting the general modeling process is shown in Figure 2-11.

2.5 NURBS-based Membrane Mechanics Modeling

In order to obtain the stress developed in the cell membrane, it is necessary to deform it based on appropriate boundary / interface conditions. The process of obtaining information from the surrounding fluid, calculating membrane forces and interfacing with the fluid to communicate the forces is part of a methodology termed as (**N**)URBS (**M**)echanics or **NM** Modeling Methodology. Thus computing a single time step broadly entails the following sub-steps:

For Time Step $\mathbf{t}^n$:

NM-I. Determine Boundary Conditions to be applied to the NURBS entity

NM-II. Apply the Boundary Conditions obtained in NM-I to the NURBS entity

NM-III. Characterize deformation of NURBS entity

NM-IV. Determine entity-specific Membrane restoring forces

NM-V. Communicate the presence of membrane forces to surrounding fluid

Repeat for Time Step $\mathbf{t}^{n+1}$.

NM-I which deals with determination of boundary conditions to be applied to the NURBS entity depends on the technique chosen for fluid-structure interaction. Consequently, the choice of interaction technique also dictates the manner in which information about the force generated in the NURBS membrane will be communicated to the fluid (i.e. Step NM-V). Steps NM-I and NM-V will be described in a following chapter and for the purposes of this chapter, it is assumed that the boundary conditions are known *apriori*. This section of Chapter 2 focuses on Steps NM-II to NM-IV.

2.5.1 NM-II: Applying Boundary Conditions to NURBS entity

In order to perform the membrane mechanics of the cell, it is necessary to first deform the cell by application of appropriate boundary conditions. Any boundary condition such as velocity, acceleration, force, etc. cannot be directly applied to the surface of the cell due to the NURBS formulation. The surface points are points which are bought to existence by a combination of control points and blending functions. Hence any manipulation to the surface has to be performed through the control points. This section describes a methodology to apply a specific boundary condition, i.e. velocity to the surface of the cell through the control points.

Applying a velocity is essentially the same as applying a displacement (since the time step size is known) and hence this is akin to applying an essential or Dirichlet boundary condition. In the NURBS Book[40], Piegl and Tiller provide a means of moving a control point based on a known displacement at a surface point. This method is only applicable to one or at most two to three points, as the method only takes into account a displacement specified at one or two neighboring surface points and only moved the control point with the most influence over that surface point(s). In the case of the cell, the entire cell has to be moved, and hence another technique has to be applied which achieves satisfactory motion for all the points. Multiple different approaches exist ranging from simple least squares [52,53], modified least squares [54] to constrained optimization and energy minimization [55]. The approach adopted here is the basic least squares approach, chosen for its relative simplicity and versatility. Moreover, many of the other methods build upon the least squares framework, and thus the implementation in this research can be adopted to reflect modifications in the least squares approach.

This section deals with the details of the least squares method for obtaining an equivalent displacement at the control points such that the surface points are displaced satisfying the applied boundary condition. This is necessary as the control points may or may not lie on the surface, a fact that is highlighted in Figure 2-7. In the figure, the control points are not on the surface of the RBC. On NURBS solids and surfaces, the positions of the surface points are "controlled" by the control points. To effect a motion of the NURBS object (irrespective of a curve, surface or solid), the control points have to be moved. But as the control points themselves are not situated on the actual surface and are elsewhere in the surrounding space, the velocities applied to the control points are different than the velocities of the fluid points in the proximity of the control points in space. The velocities applied to the control points are not necessarily the velocities of the surface points directly, as each control point has varying influence on a number of surface points. This essentially poses an interpolation problem where the least squares

method for interpolating values to the control points should satisfy the necessary boundary condition specification on the surface points.

In the least squares method, the underlying principles of any NURBS object is preserved, i.e. the contribution of the control points to the surface points in the form of the blending functions is factored into the formulation. The implementation of this formulation is described for a NURBS surface rather than a NURBS solid due to the manner of construction of the NURBS solid described earlier. The solid can be envisioned as multiple surfaces atop one another and connected across the thickness, maintaining surface normal vectors at every point. Hence in order to displace a NURBS solid created in this fashion, it is sufficient to determine the displacement of one of the surfaces, and simply displace the remaining surfaces by the same amount. This also functions to preserve the incompressibility of the membrane material. For the purposes of the current research, incompressibility of the membrane is a fundamental assumption that is followed. However, the creation of a 3-D NURBS solid lends itself to the future implementation of varying thickness across the membranes, if so desired, by simply displacing the multiple surfaces by varying amounts depending on the differential displacements to be applied.

Recall that any point on a NURBS surface was denoted by equation (2.13), and is reproduced here:

$$\boldsymbol{S}(u,v) = \sum_{i=0}^{n}\sum_{i=0}^{n} R_{i,j}(u,v)\ \boldsymbol{P_{i,j}} \tag{2.16}$$

where $R_{i,j}(u,v)$ are the shape functions (or basis functions) for a 2-D NURBS formulation, which in turn is derived from a tensor product of two 1-D NURBS basis functions. It is clear that for every control point $\boldsymbol{P_{i,j}}$ there exists a set of shape functions $R_{i,j}$. Equation (2.16) is the equation for a particular point on the surface. Here, the number of effective control points having influence over any surface point is $n = p + 1$ $in\ each\ parameteric\ direction$ where p is the degree of the surface in that particular

direction. For a NURBS surface, there are a total of $(p+1)*(q+1)$ influencing control points for every surface point, where p and q are the degrees in the u and the v parametric directions.

The displacement field around the surface points (also called knot points) is known from the fluid surrounding the surface points. This known displacement field is denoted in (2.17):

$$\boldsymbol{U_{known}} = \boldsymbol{U}(\overline{\boldsymbol{X}}) \tag{2.17}$$

where $\bar{\boldsymbol{X}}$ is the location of the knot points (or surface points) in 3-D Cartesian space. The method of determining the actual displacement field $\boldsymbol{U_{known}}$ will be explained in more detail in Chapter 6 which deals with the FSI. For the purposes of this chapter, it is assumed to be known a priori. Once the specified displacements of the knot points are known, the required parameters to be calculated can now be stated, shown in (2.18):

$$\boldsymbol{U_{calc}} = \sum_{i=0}^{n}\sum_{i=0}^{n} R_{i,j}(u,v)\ \boldsymbol{dP_{i,j}} \tag{2.18}$$

where $\boldsymbol{U_{calc}}$ is the actual displacement field which will be calculated based on the displacements prescribed at the control points $\boldsymbol{dP_{i,j}}$. This can be set up in terms of the least squares formulation, where the error in the actual (known) and calculated knot point displacement is to be minimized, i.e.

$$Minimize: \ \varepsilon = \int (U_{known} - U_{calc})^2\, dS \tag{2.19}$$

The minimization function is calculated over the entire surface, element by element. This lends itself nicely to the actual NURBS formulation, as this can be performed easily over discrete elements and can be assembled together as a sum of element contributions. Following the approaches mentioned in [54], the formulation can be written as:

$$\left[\int_{element} R_{ij}R_{ji}\, dS\right][U_{calc}] = \left[\int_{element} R_{ij}[U_{known}]\, dS\right] \tag{2.20}$$

$$\left[\int_{element} R_{ij}R_{ji}\, dS\right] = K_{ij} = [RR^T] \tag{2.21}$$

$$\left[\int_{element} R_{ij}[U_{known}]\, dS\right] = Q_i = [R][U_{known}] \tag{2.22}$$

The final form of (2.22) can be written in a canonical form as a standard matrix equation:

$$[K][U_{calc}] = [Q] \tag{2.23}$$

where [K] can be thought of as a "stiffness" matrix and [Q] can be thought of as a "force" matrix from a traditional FEM perspective. This is solved using a LU decomposition algorithm [56]. It is worthwhile mentioning here that although the displacement field is a vector (3-D), it can be treated as a system of discrete scalar component equations, as there is no coupling between the components. This is shown in (2.24), and this is done on a local level (element-by-element) after which the global matrices are assembled and solved. A schematic of the methodology for boundary condition interpolation is shown in Figure 2-12.

$$[K]\begin{bmatrix} \vdots & \vdots & \vdots \\ U_{calc_x} & U_{calc_y} & U_{calc_z} \\ \vdots & \vdots & \vdots \end{bmatrix} = \begin{bmatrix} \vdots & \vdots & \vdots \\ Q_x & Q_y & Q_z \\ \vdots & \vdots & \vdots \end{bmatrix} \tag{2.24}$$

2.5.2 NM-III: Characterization of the Deformation of the NURBS entity using Isogeometric Analysis

Once the boundary conditions are specified, the position and configuration of the RBC is updated. This causes the RBC to deform according to the surrounding flow field, which leads to development of stresses within the membrane. This section describes the calculation of the membrane forces after updating the configuration of the RBC. Note that the method described to update the position of the RBC did so for the middle surface. The control points for the upper and lower surfaces are updated using the displacement values of corresponding control points for the middle surface, as the control point "net" is located along the local surface normal. In order to determine the stress distribution over the NURBS RBC surface, the displacements of the nodes are first calculated. This is followed by utilizing the shape functions (element interpolation functions) to determine

the displacements of the integration points (Gauss Quadrature points) over the surface. The displacements of the integration points will then be used to determine the strains and subsequently, the membrane forces. A 2x2 quadrature was used due to the bicubic description of the surface of the RBC.

Recall the 3-D NURBS solid definition from (2.14), which can be recast into the concise form.

$$\boldsymbol{S}(u,v,w) = \frac{\sum_{i=0}^{n}\sum_{j=0}^{m}\sum_{k=0}^{l} N_{i,p}(u)N_{j,q}(v)\,N_{k,r}(w)\,W_{i,j,k}\,\boldsymbol{P_{i,j,k}}}{\sum_{i=0}^{n}\sum_{j=0}^{m}\sum_{k=0}^{l} N_{i,p}(u)N_{j,q}(v)\,N_{k,r}(w)\,W_{i,j,k}} \tag{2.25}$$

$$R_{i,j,k}(u,v,w) = \frac{N_{i,p}(u)N_{j,q}(v)N_{k,r}(w)\;\;W_{i,j,k}}{\sum_{i=0}^{n}\sum_{j=0}^{m}\sum_{k=0}^{l} N_{i,p}(u)N_{j,q}(v)\,N_{k,r}(w)\,W_{i,j,k}} \tag{2.26}$$

$$\boldsymbol{S}(u,v,w) = \sum_{i=0}^{n}\sum_{j=0}^{m}\sum_{k=0}^{l} R_{i,j,k}(u,v,w)\;\;\boldsymbol{P_{i,j,k}} \tag{2.27}$$

Thus the 3-D rational function $R_{i,j,k}(u,v,w)$ which is a representation of all the NURBS basis functions is comprised of 3 individual, 1-D NURBS basis functions. Dropping the scalars - the weights and the denominator for convenience, we have:

$$R = Nu \cdot Nv \cdot Nw \tag{2.28}$$

where $Nu = N_{i,p}(u)\,, Nv = N_{j,q}(v)\,, Nw = N_{k,r}(w)$

The derivatives of the rational function **R** with respect to the parametric directions *u*,*v* and *w* are given by (using the classical chain rule of differentiation):

$$\frac{\partial R}{\partial u} = Nu_{,u} \cdot Nv \cdot Nw \tag{2.29}$$

$$\frac{\partial R}{\partial v} = Nu \cdot Nv_{,v} \cdot Nw \tag{2.30}$$

$$\frac{\partial R}{\partial w} = Nu \cdot Nv \cdot Nw_{,w} \tag{2.31}$$

However, it is evident that R can also be represented in terms of the Cartesian co-ordinates:- $R = R(x,y,z) = R(x(u,v,w), y(u,v,w), z(u,v,w))$.

The conventional Jacobian representation follows:

$$\begin{pmatrix} \frac{\partial R}{\partial u} \\ \frac{\partial R}{\partial v} \\ \frac{\partial R}{\partial w} \end{pmatrix} = \boldsymbol{J} \begin{pmatrix} \frac{\partial R}{\partial x} \\ \frac{\partial R}{\partial y} \\ \frac{\partial R}{\partial z} \end{pmatrix} \quad , \quad \boldsymbol{J} = \begin{bmatrix} \frac{\partial x}{\partial u} & \frac{\partial y}{\partial u} & \frac{\partial z}{\partial u} \\ \frac{\partial x}{\partial v} & \frac{\partial y}{\partial v} & \frac{\partial z}{\partial v} \\ \frac{\partial x}{\partial w} & \frac{\partial y}{\partial w} & \frac{\partial z}{\partial w} \end{bmatrix} = \boldsymbol{Jacobian} \tag{2.32}$$

The derivatives with respect to the Cartesian co-ordinates can be obtained as J is invertible.

$$\begin{pmatrix} \frac{\partial R}{\partial x} \\ \frac{\partial R}{\partial y} \\ \frac{\partial R}{\partial z} \end{pmatrix} = \boldsymbol{J^{-T}} \begin{pmatrix} \frac{\partial R}{\partial u} \\ \frac{\partial R}{\partial v} \\ \frac{\partial R}{\partial w} \end{pmatrix} \tag{2.33}$$

The above calculations are performed for the reference configuration of the RBC. Mathematically, the reference configuration can be described as:

$$\boldsymbol{X}(u,v,w) = \sum_{i=0}^{n} \sum_{j=0}^{m} \sum_{k=0}^{l} R_{i,j,k}(u,v,w)\ \boldsymbol{P_{i,j,k}} \tag{2.34}$$

Similarly, the current (deformed) configuration of the RBC can be obtained:

$$\boldsymbol{x}(u,v,w) = \sum_{i=0}^{n} \sum_{j=0}^{m} \sum_{k=0}^{l} R_{i,j,k}(u,v,w)\ \boldsymbol{p_{i,j,k}} \tag{2.35}$$

The deformation gradient can now be expressed mathematically as:

$$\boldsymbol{F} = \frac{\partial \boldsymbol{x}}{\partial \boldsymbol{X}} = \sum_{i=0}^{n} \sum_{j=0}^{m} \sum_{k=0}^{l} \boldsymbol{x} \otimes \nabla R_{i,j,k} \tag{2.36}$$

where ∇R is the referential gradient of the shape function, obtained in (*), and $\otimes$ denotes the standard tensor product. The deformation gradient is now used to obtain the right$[\boldsymbol{C}]$ and left$[\boldsymbol{B}]$ deformation tensors

$$[\boldsymbol{C}] = F^T F \tag{2.37}$$

$$[\boldsymbol{B}] = F F^T \tag{2.38}$$

Once the deformation gradient has been determined, the next step is to quantify the extent of deformation in terms of the restoring forces set up in the membrane.

2.5.3 NM-IV: Determine Entity-Specific Membrane Restoring Forces using Constitutive Relations

Upon obtaining the deformation gradient and the stretch tensors, a constitutive model can now be implemented to determine the membrane restoring force based on the kind of NURBS entity – eg. RBC, leukocyte, etc. The modular implementation of the membrane mechanics analysis procedure enables the use of many different constitutive models to describe the behavior of the membrane depending on the entity in question. For the purposes of describing the method of determining membrane forces, the case of the RBC is examined. Skalak et al in 1973 [35] proposed a membrane strain energy function for RBC membranes which incorporated a penalty term based on area dilatation of the membrane. The RBC is known to be highly deformable, while at the same time the membrane area does not dilate by more than ~4% [57]. In this study, for the ease of implementation and to aid comparison to literature, the neo-Hookean model is also employed due to its prolific use in the research community for simulations involving red blood cells [11,21,30,31]. The Skalak and neo-Hookean models are shown in (2.39) and (2.40).

$$W = \frac{E_b}{4}\left(\frac{1}{2}{I_1}^2 + I_1 - I_2\right) + \frac{E_c}{8}{I_2}^2 \tag{2.39}$$

$$W = \frac{E_b}{6}\left(\frac{1}{I_2} + I_1\right) \tag{2.40}$$

where I_1 and I_2 are the invariants, and W is the strain energy density function. The factors $E_b = 0.005\ dyn/cm$ and $E_c = 5 - 100\ dyn/cm$ are membrane material properties. E_c is a property which introduces a penalty for area dilatation, i.e. very large tensions are introduced when area dilatation increases beyond physiologically possible values.

The membrane tension is obtained using the material's strain energy density function and measures of the deformation of the surface.

$$[\boldsymbol{\tau}] = \frac{2}{\lambda_1\lambda_2}\frac{\partial W}{\partial I_1}[\boldsymbol{B}] + 2\lambda_1\lambda_2\frac{\partial W}{\partial I_2}(\bar{\boldsymbol{I}} - \bar{\boldsymbol{n}}.\bar{\boldsymbol{n}}) \tag{2.41}$$

where λ_1, λ_2 are the principal stretches, $[\boldsymbol{B}]$ is the left Cauchy deformation tensor, $\bar{\boldsymbol{I}}$ is the identity matrix and $\bar{\boldsymbol{n}}$ is the outward unit normal from the surface at a particular integration point.

It is important to note at this point that the in-plane membrane tension only gives the instantaneous tension at the gauss-integration points of the membrane. The forces that are to be transmitted to the fluid are obtained from calculating the gradient of the in-plane tension values over the surface. The method used to obtain the nodal forces follow that suggested in [58].

The forces which are to be transmitted to the fluid can be expressed mathematically as:

$$\boldsymbol{f_i} = \nabla.\tau \tag{2.42}$$

In (2.42), ∇ denotes surface divergence. As each element is evaluated for the aforementioned parameters and the in-plane tension tensor is obtained at each gauss integration point, the force that is developed in that element is distributed to all the control points that are influencing that element. The number of control points influencing a particular element is given by the type of element (i.e. the degree). Since the example shown above is a $(3\ X\ 3\ X\ 2)$ (i.e. cubic by cubic by quadratic element), the number of influencing control points per element is $(3+1)*(3+1)*(2+1) = 48$. Hence every element has 48 shape functions contributing towards its definition and operation. Recall that the combined shape function at any location is a product of the individual shape functions in the three parametric directions, and that the derivatives of the shape functions with respect to the Cartesian co-ordinate system are given in (2.33).

The nodal forces are obtained as follows [58]:

$$\boldsymbol{f_i} = \int R_{i,j}\boldsymbol{\tau_{ij}}\ dV = \int [\boldsymbol{R'}][\boldsymbol{\tau_{11}}\ \boldsymbol{\tau_{22}}\ \boldsymbol{\tau_{33}}\ \boldsymbol{\tau_{12}}\ \boldsymbol{\tau_{13}}\ \boldsymbol{\tau_{23}}]^T\ dV \tag{2.43}$$

where the matrix $[\boldsymbol{R'}]$ is the nodal strain-displacement matrix, as described in [58]

$$[\boldsymbol{R}'] = \begin{bmatrix} \frac{\partial R}{\partial x} & 0 & 0 & \frac{\partial R}{\partial y} & 0 & \frac{\partial R}{\partial z} \\ 0 & \frac{\partial R}{\partial y} & 0 & \frac{\partial R}{\partial x} & \frac{\partial R}{\partial z} & 0 \\ 0 & 0 & \frac{\partial R}{\partial z} & 0 & \frac{\partial R}{\partial y} & \frac{\partial R}{\partial x} \end{bmatrix} \tag{2.44}$$

The summation of the resultant force(i.e. vector sum) is taken over all the control points. It is this force that is felt by the fluid surrounding the NURBS entity, and the method to distribute the membrane forces to the surrounding fluid will be described in a later chapter.

2.6 Validation of NURBS Isogeometric Modeling Technique

NURBS models were created for spherical and biconcave cells. The spherical models consisted of 176-9000 NURBS elements while the biconcave models consisted of 220-6400 NURBS elements, shown in Figure 2-19. Prior to interfacing with the fluid, basic tests were performed on the NURBS models to ensure and test that the coarse models were able to capture the deformations accurately. Towards this end, the NURBS models were subjected to known flow fields which were analytically prescribed. The prescribed flow fields were then used to interpolate the boundary conditions on the NURBS models, thereby deforming them and the deformation was quantified.

2.6.1 The Patch Test

Prior to testing the spherical and biconcave models, a patch test was conducted on a NURBS patch. A patch test verifies the integrity of the model to capture responses to deformation. It also tests mesh quality, information exchange across different elements and is a standard test used in the modeling community for testing meshes. Though a majority of the applications of this test in the community are on FEM based meshes, the standard patch test can be used to test the quality of an entity meshed using other methods as well.

A NURBS patch in the form of a square sheet with finite thickness was created for this purpose. Two different meshes were created – a coarse and a fine mesh. The side of the square sheet was 10 units and the thickness was 1 unit. The coarse mesh had 9 NURBS elements and the fine mesh had 36 NURBS elements. Note however, that the dimensions of the sheet are immaterial to the purpose of the test. It is essential, however, that the patch created has at least one internal element, i.e., an element that is contained entirely in the interior of the patch and is not exposed to any of the boundaries. For details, please refer [58].

There are multiple methods to administer a patch test. A common way in FEM is to prescribe an arbitrary linear displacement field and measure the calculated membrane stresses and/or displacements. A simpler way for non-FEM approaches is to specify a linear displacement field and check the forces obtained at the nodes. In a linear or bilinear displacement field, the internal elements should have zero force. The latter test was adopted, as it corresponded with the nature of calculations expected from the procedure (i.e. displacements being specified and the resulting the membrane forces are computed).

A (i) linear and (ii) a bilinear displacement field were prescribed to the control points of the NURBS Patch for both meshes. The membrane forces was obtained and plotted at the nodes. As the bilinear field specified was symmetric in both x and y-directions, this resulted in a symmetric force distribution being computed over the patch. The lower left corner of the patch coincides with the origin (0,0), and this has the effect of anchoring the patch down at that point (no displacement). As a result, the specified bilinear field effectively tries to stretch the patch evenly in both directions. The interior of this patch should give rise to zero strains and should not have any force calculated. As expected, the internal nodes had zero force associated with the internal elements for both meshes, as is shown in Figure 2-13. This demonstrated that the NURBS methodology was implemented successfully.

2.6.2 Verification of Boundary Condition Application to the NURBS entity (NM-II)

2.6.2.1 Poiseuille Flow

After the patch test, the least squares method for applying boundary conditions was tested by imparting a Poiseuille flow profile to a biconcave RBC. The flow was prescribed analytically on four RBC meshes with elements ranging from N=84 to N=6400. Large deformation was prescribed over a single time step in order to investigate extreme deformations. The flow-field prescribed analytically is given below:

$$V_x = 0,\ V_y = 0,\ V_z = \mathrm{Q} * (x^2 + y^2) \tag{2.45}$$

where V_x, V_y and V_z are the components of the velocity vector in the three Cartesian directions, Q is a constant and x, y are the locations of the surface points in space. The orientation of the model was such that the x, y directions were assumed to be in the radial directions and the z direction was along the length of the capillary. The deformation was executed in one time step. During the timestep, NM-II – NM-IV were all executed: NH-II, the least squares calculation was used to determine control point displacements; NM-III, the deformation gradient was determined and NM-IV, the membrane forces were calculated, as described above. This was done not only to determine the time taken for calculating the aforementioned quantities for different meshes, but also to compare the membrane forces meshes of varying densities. Two different values of Q were used - a lower and a higher value to determine the effect of large deformations on the accuracy of the approach. Because the flow-field was analytically prescribed, the membrane deformation was compared with the correct, known locations of the surface points, and thuswas used for comparison. The RMS error was calculated between the exact and obtained locations of the surface points to determine the performance of the least squares approach across the various meshes.

The deformed shapes for the coarse and fine RBC models is shown in Figure 2-14 for a high value of Q. Even the coarse model captures the deformation very accurately, with the two deformed meshes almost overlapping. There is no loss of geometric integrity with the coarse mesh due to the high order (cubic) nature of the NURBS surface. Figure 2-15 shows the comparison of the analytical and computed locations of several arbitrary points on the surface for both the coarse and fine meshes. In both cases, the exact and calculated locations overlap. Figure 2-16 shows the RMS error across the two meshes tested for a high value of Q. The coarse mesh had the largest error of 0.7% and the error reduced to less than 0.1% for finer meshes. For the case with lower Q, the largest error was ~ 0.3% for the coarsest mesh. This showed that not only does the coarsest mesh accurately capture the deformation, but that there is no loss of geometric integrity as the mesh is coarsened, depicting the utility of using a NURBS approach.

2.6.2.2 Straining Flow

The RBC was also subjected to a straining flow. The flow-field prescribed was:

$$V_x = \frac{1}{2} * \mathrm{Q} * x\,,\ V_y = -\frac{1}{4} * \mathrm{Q} * y,\ V_z = -\frac{1}{4} * \mathrm{Q} * z \tag{2.46}$$

where the symbols have the same meaning as explained earlier. The flow-field was prescribed was incompressible, hence the values of the coefficients. Here too, a large value of Q was prescribed to the same meshes used for the Poiseuille flow case. Figure 2-18 shows the deformed shapes after one time step. As the flow-field was 3-D in nature instead of the simpler paraboloid profile of Poiseuille flow, the RMS error was ~1% for the coarsest mesh but reduced to < 0.2% for finer meshes. Moreover the deformation prescribed was an extreme case for a single time step and hence the performance of the least squares approach was deemed satisfactory. The strongest feature of this exercise was the geometric integrity that was maintained even for highly coarse meshes.

2.6.3 Verifying Isogeometric Analysis Approach (NM-III and NM-IV)

After the application of boundary conditions was verified satisfactorily, the NURBS isogoemetric analysis method described in detail in section 2.5.2 and 2.5.3 was examined by prescribing analytical deformation fields to spherical and biconcave models . The spherical model was incorporated as it was envisioned to use spheres for platelets, white blood cells and cancer cells. As mentioned earlier, the spherical models were created with NURBS meshes ranging from 176 – 9000. The most basic test carried out for a sphere was an uniform expansion test. The expanding flow-field was analytically prescribed such that the sphere expands uniformly in all directions. This simulated the application of a uniform isotropic tension over the entire sphere. The expansion test was carried out for the two coarsest meshes for a sphere, with 176 and 640 NURBS elements respectively. The forces obtained at the nodes on the surface of the sphere is shown in Figure 2-20. Since the finer of the two aforementioned meshes had roughly double the mesh density across both the latitude and longitude, the forces for the finer mesh were divided by a factor of 4 for comparison. While inexact, the purpose of this test was to investigate not only the values but more importantly the force distribution across the surface. As expected, there is a uniformly outward directed force across the entire sphere. The magnitudes of the forces are dependent on the size of the NURBS elements. As the NURBS elements are irregularly sized, the force values are not the same across the entire surface, with the values being highest near the equator on account of the largest elements and conversely being the lowest near the poles on account of the smallest elements present there. However the force distribution across both meshes were the same, which proved that the coarse meshes can efficiently replicate the applied deformation compared to finer meshes. The maxima and minima of the forces also match very well across both meshes.

A straining profile was also applied to the same spherical models. The straining profiles were similar to the flow-field prescribed to investigate the behavior of an RBC in the previous section. Figure 2-21 shows the force distribution for the two spherical models. The mesh is also shown for convenience and to highlight the coarseness of the model. The locations of the maxima and minima are very accurately replicated and the values of the maximum and minimum forces also match closely. Figure 2-21 shows the direction of the forces at the surface points. It can be clearly seen that the direction of forces are the same for both the coarser and finer meshes, with the finer mesh evidently containing a greater density of nodes and hence force vectors.

Similarly, the straining flow-field was prescribed on RBC models to determine the force distribution in the membrane, and also verify that zero area dilatation which is a property of RBCs was being appropriately enforced. In order to test the models, a coarse and fine mesh were chosen such that they could be better compared with each other. Though the coarsest RBC model had 84 elements, the other models created contained a more even node distribution and two such meshes were chosen for comparison. The coarse mesh contained 440 NURBS elements and the fine mesh contained 1680 NURBS elements. The force distribution on the RBC models subjected to a straining flow-field is shown in Figure 2-22. As can be seen, the distributions are very similar, with the locations of maxima and minima replicated by the coarse mesh. Figure 2-22 shows the force vectors for both aforementioned meshes. The RBC models were also subjected to a Poiseuille flow-field similar to that prescribed in the earlier sections. The force distribution and force vector directions are shown in Figure 2-23. It is clearly seen that the coarse models replicate and agree with the force distributions computed for the finer mesh, thereby showing that the NURBS approach could be used as a viable alternative to traditional FEM-based approaches.

2.7 Summary and Discussion

In this chapter a novel modeling approach was proposed using NURBS. The motivation behind the development of this methodology was to overcome the drawbacks of using traditional FEM-based approaches (high computational cost per cell, point-by-point searching algorithms for contact modeling, potential communication costs during parallel processing) which stem from the large number of elements necessary to represent a cell such as a RBC. Various 3D NURBS models for both biconcave and spherical cells were presented, with detailed information on achieving deformation of the NURBS entities using the least squares approach, as well as performing NURBS based isogeometric analysis using constitutive models. The main difference between traditional FEM-based approaches and the NURBS approach is the ability to represent the exact geometry using very few NURBS elements and to apply the isogeometric concept for analysis using the same NURBS basis functions used for creating the said geometry. This makes NURBS-based isogeometric analysis a holistic simulation approach, with the basis functions being used for representing the geometry, effecting deformation and performing stress analysis. It was clearly seen that extremely coarse meshes still captured the geometry of the entities of interest – namely the biconcave and spherical shapes of the cells, with the ability to use as coarse as 84 elements for representing the complex biconcave shape of the erythrocyte. As mentioned in [39], the NURBS based system is a very versatile and homogeneous system compared to high order FEM systems, an advantage which could be used effectively in performing analysis of the deformation based on constitutive models. While NURBS-based geometric modeling has found applications in the biomedical industry only over the past decade [42,43], the advantages of using NURBS-based isogeometric analysis had been recognized earlier to model the deformations of various structures and entities which were typically modeled using FEM [39,40] and hence there is a wealth of knowledge available in implementing and incorporating NURBS approaches in modeling biological cells. After accurately

describing NURBS models of a characteristic biconcave RBC, methods were implemented to impart deformation of a NURBS entity using a least squares approach. This was necessitated by the control points not necessarily lying on the NURBS surface. While the least squares scheme implemented here is a global scheme, local schemes may be employed in the future to reduce computational cost and time [59]. A comprehensive description of the isogeometric membrane mechanics analysis approach was also presented and described. The membrane mechanics approach is an implementation of the methodology presented in [58], and can be improved or changed in the future based on need. A modular approach has been implemented here which enables the use of multiple constitutive models for describing the membrane mechanics [22]. The neo-hookean and Skalak models have been implemented in this work. The least squares approach was tested and validated for canonical flow-fields which were prescribed analytically. The RMS error for a biconcave RBC was ~1% or less based on the extent of deformation prescribed for the coarsest mesh tested containing 84 elements. The membrane mechanics analysis was tested first by performing a basic patch test and subsequently by subjecting spherical and biconcave models to canonical flows. The coarse models for both spherical and biconcave models performed very well by efficiently capturing the force distributions and the range of forces for all cases studied. Thus the NURBS approach makes a strong case for potentially being used as a viable alternative for FEM-based methods. Moreover a very strong advantage of NURBS over other approaches lies in the ability to implement efficient contact algorithms to simulate multiple particle interactions [45,47], where the coarse nature of NURBS models would aid in faster computations for simulating large number of biological cells.

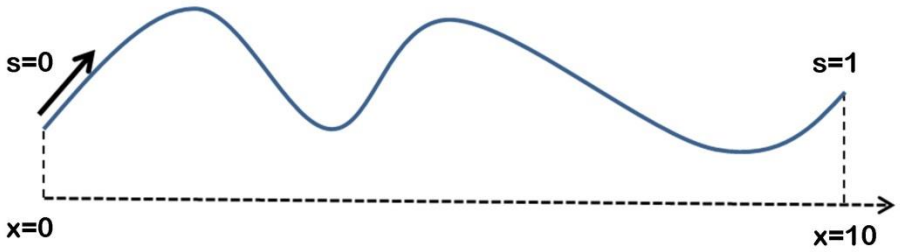

Figure 2-1: Example curve showing two techniques to describe the geometry – (i) Parametric description where the parameter 's' is described along the curve, s=0 at the start of the curve and s=1 at the end of the curve, and (ii) Regular Cartesian system where the curve spans a length of 10 units in the typical x-direction.

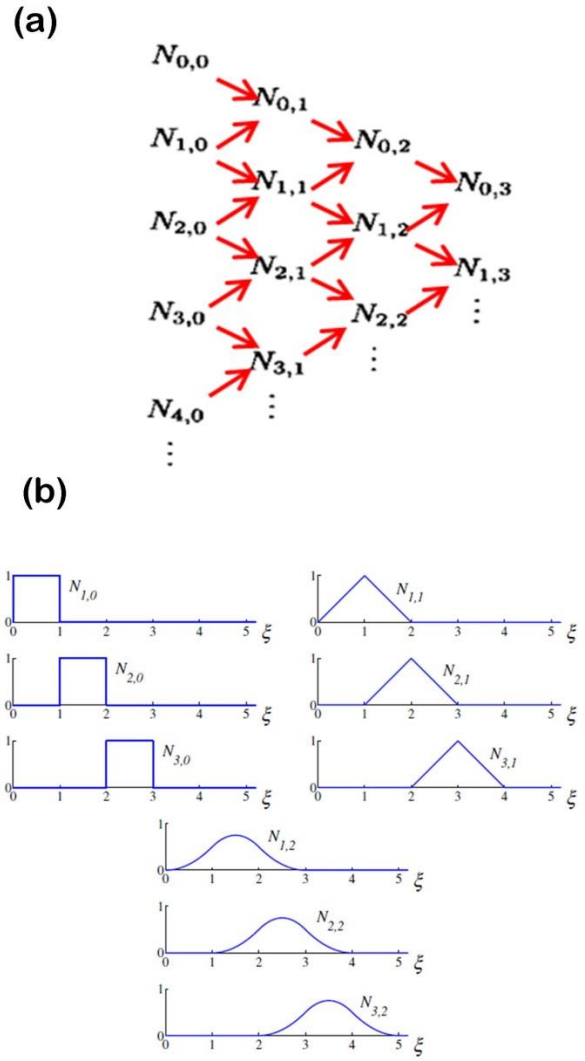

Figure 2-2: Example of B-Spline basis function determination (a) Typical information flow to construct basis functions of 1st, 2nd and 3rd order using triangular information flow system [40] (b) Typical basis functions of 1st(square), 2nd (triangular) and 3rd (parabolic) order [39].

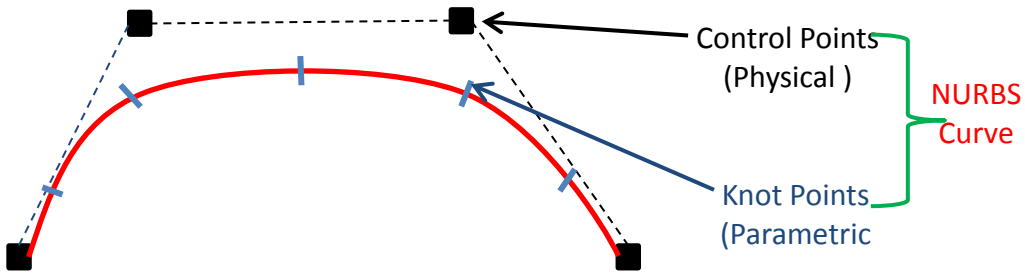

Figure 2-3: Basic B-Spline Curve showing locations of control points (black squares), control polygon which specifies the boundary within which the curve lies (dotted lines), knot points specified along the length of the curve (blue markers) and the resulting NURBS curve (red).

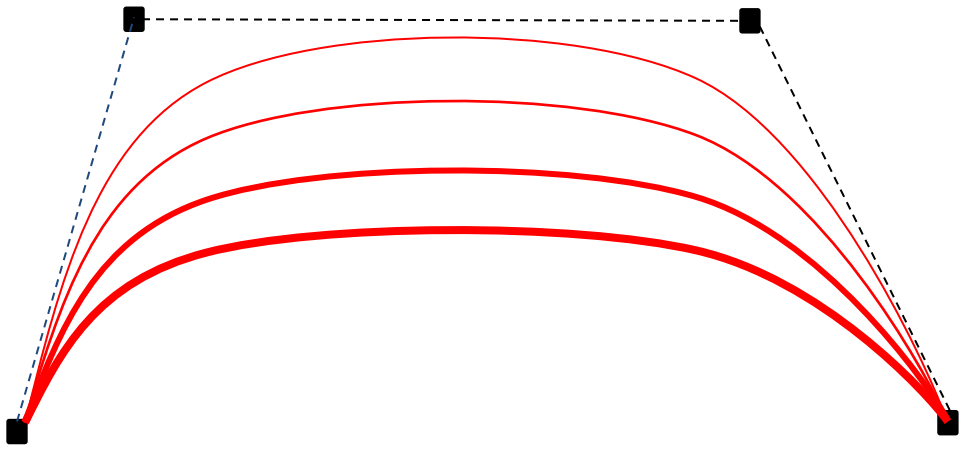

Figure 2-4: Representation of B-spline curves of increasing degrees for same control polygon. The same control points and control polygon can be used to create curves of increasing degree and reducing tortuosity. The degree of the curve increases with increasing thickness(red lines).

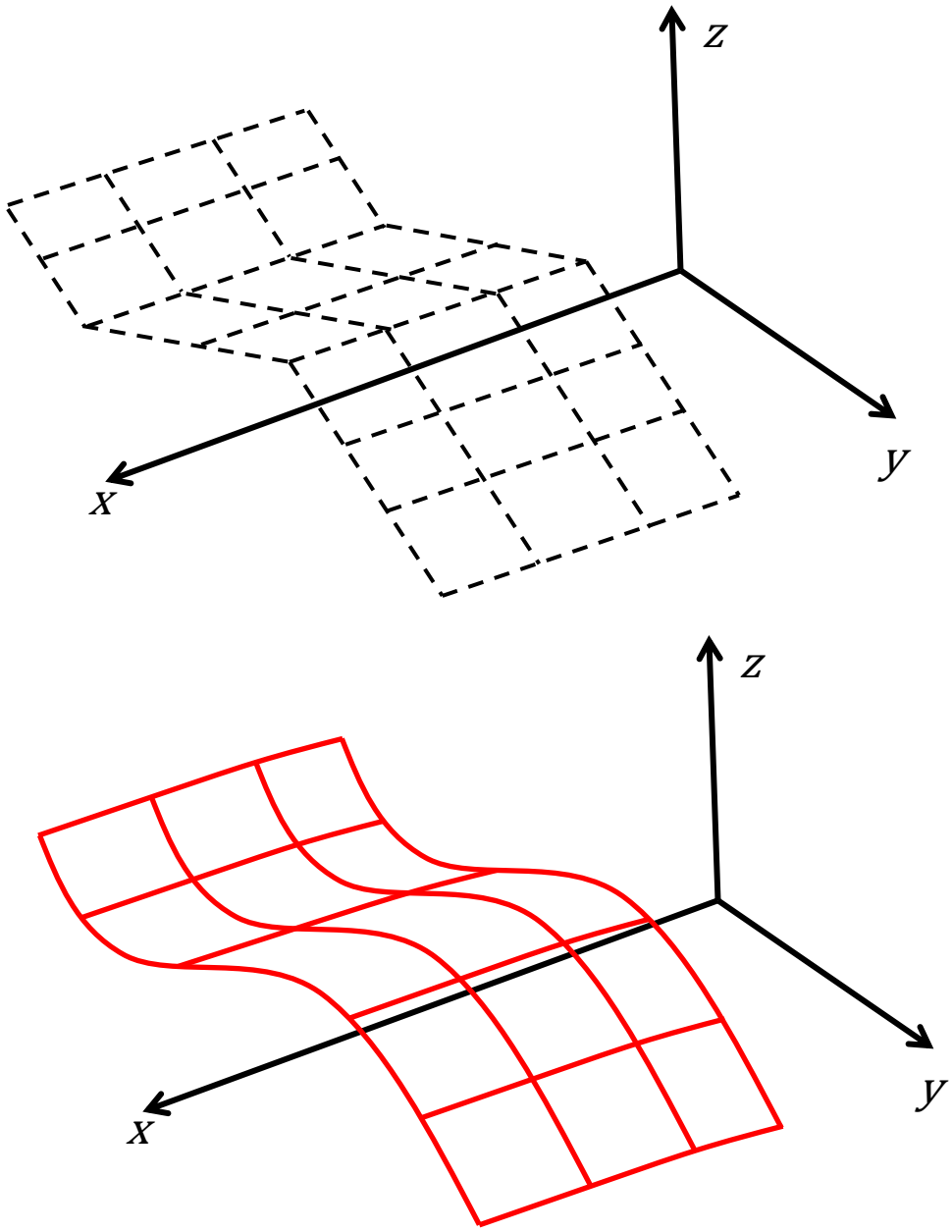

Figure 2-5: Bidirectional control point net in 3-D space and corresponding 2-D NURBS surface. The NURBS surface is 2-D in the NURBS space but 3-D in the Cartesian space.

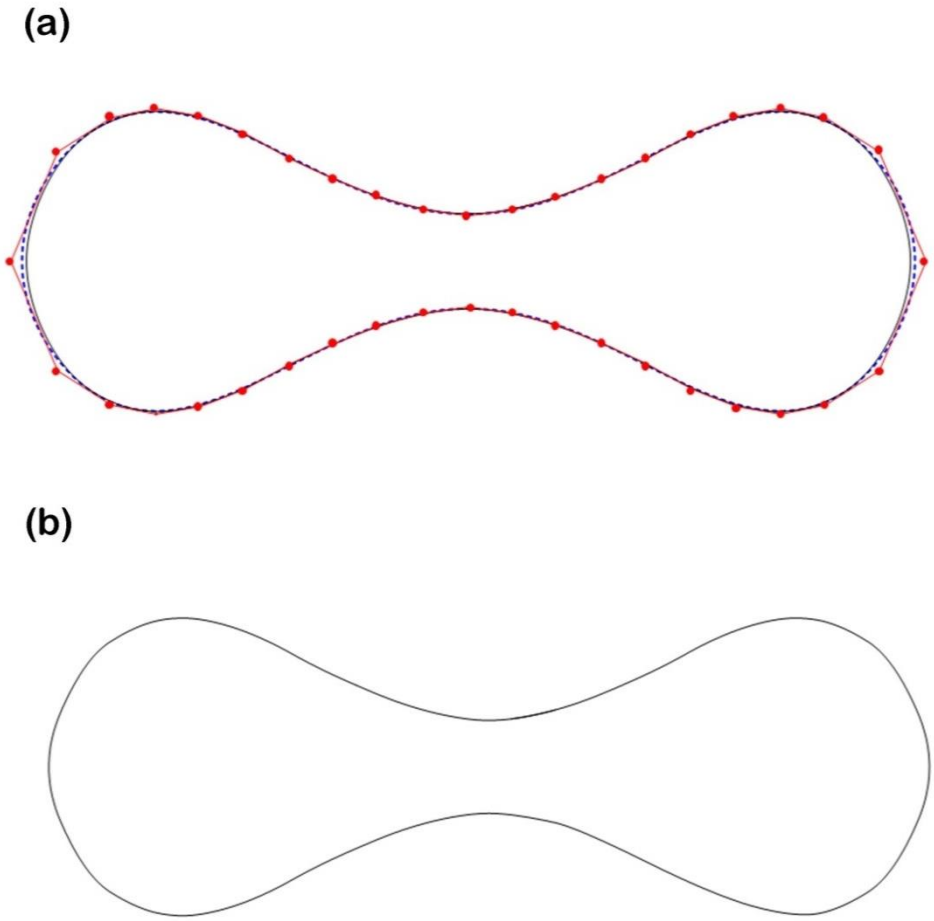

Figure 2-6: 1-D NURBS RBC model (a) 1-D RBC model based on an equation for biconcave shape in [21]. Red points are control points, the black solid line is the resulting 1-D NURBS curve and the dotted blue curve is the shape prescribed in [21] .(b) 1-D NURBS biconcave RBC shape from (a) shown without control points for clarity.

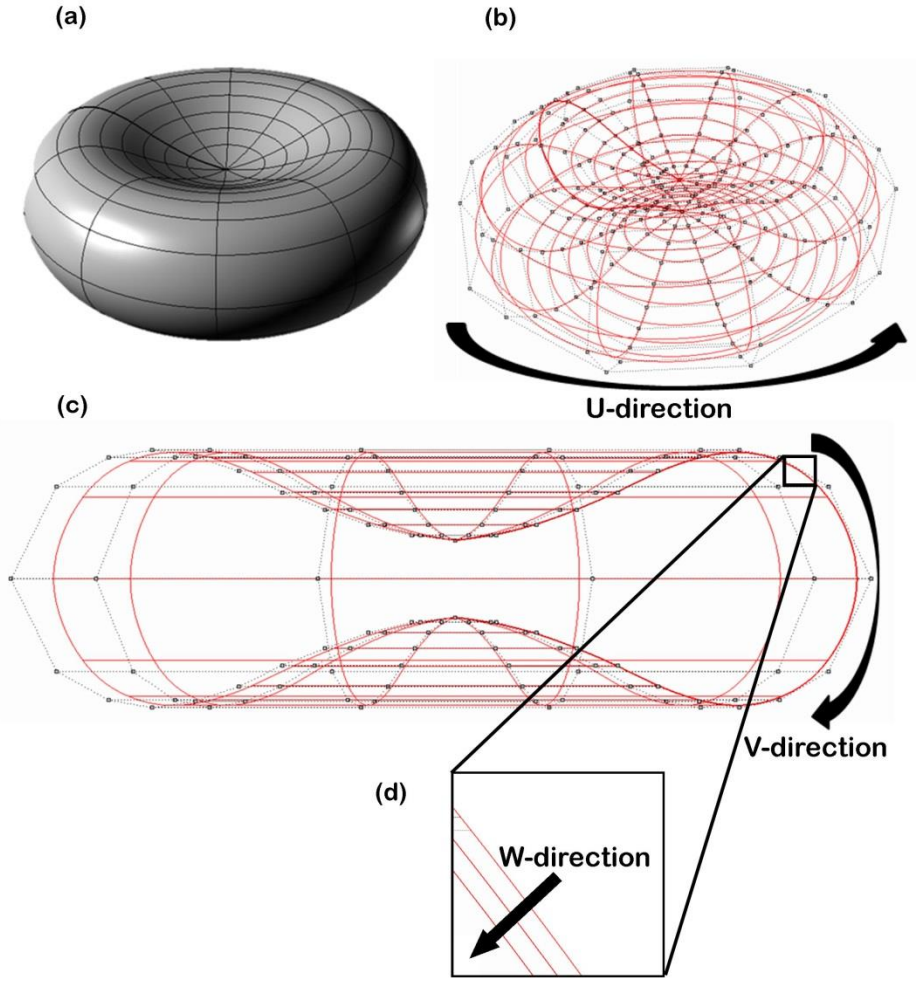

Figure 2-7: 3D NURBS RBC model (a) Shaded view with knot mesh (black lines) shown (b) Wireframe view, depicting knot mesh(red) and control points(black spheres) (c) Transverse wireframe view (d) Parametric direction along thickness. The three parametric directions are also shown.

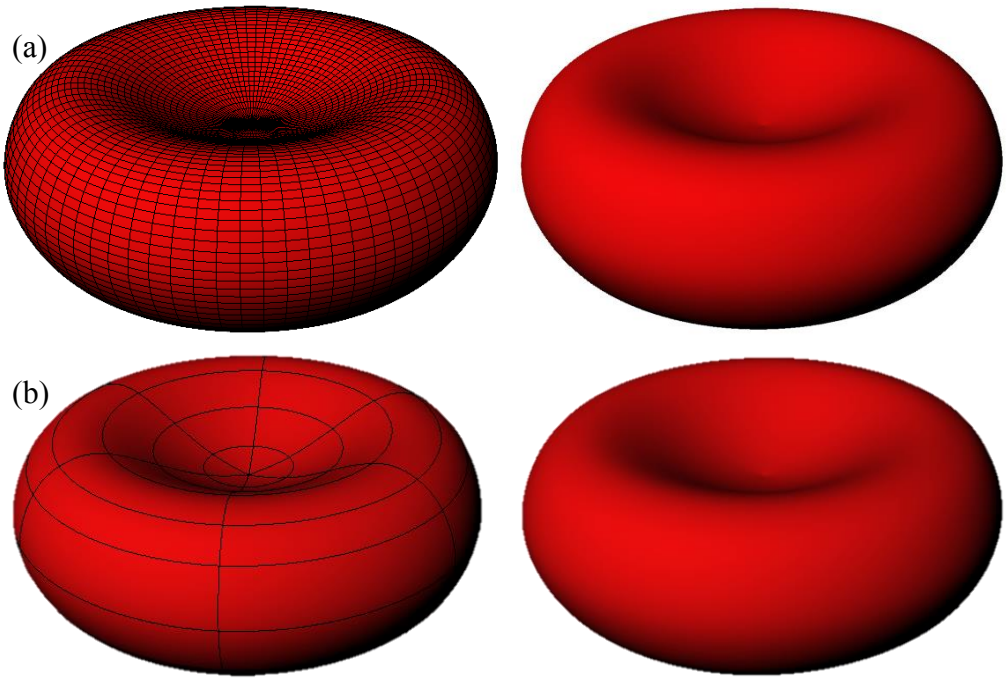

Figure 2-8: Fine and coarse RBC models (a) finest models with 6400 elements (left) and smooth render (right) (b) Coarsest model with 84 elements (left) and corresponding render (right).

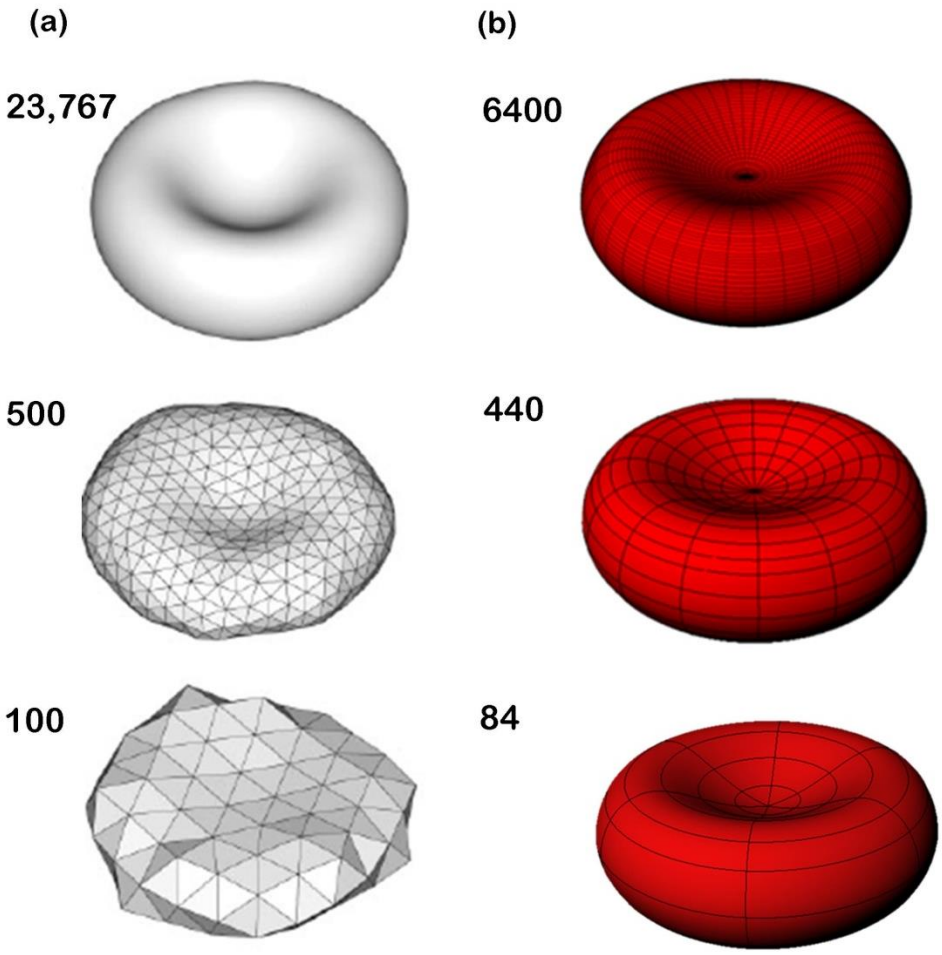

Figure 2-9: Example of preservation of geometry using isogeometric modeling as compared with a loss of geometric information using traditional FEM modeling as the mesh coarsens (from finest –TOP to coarsest –BOTTOM) (a) Various RBC FEM models [60] (b) Various RBC NURBS models created in present research. Numbers to the left of the models denote number of elements.

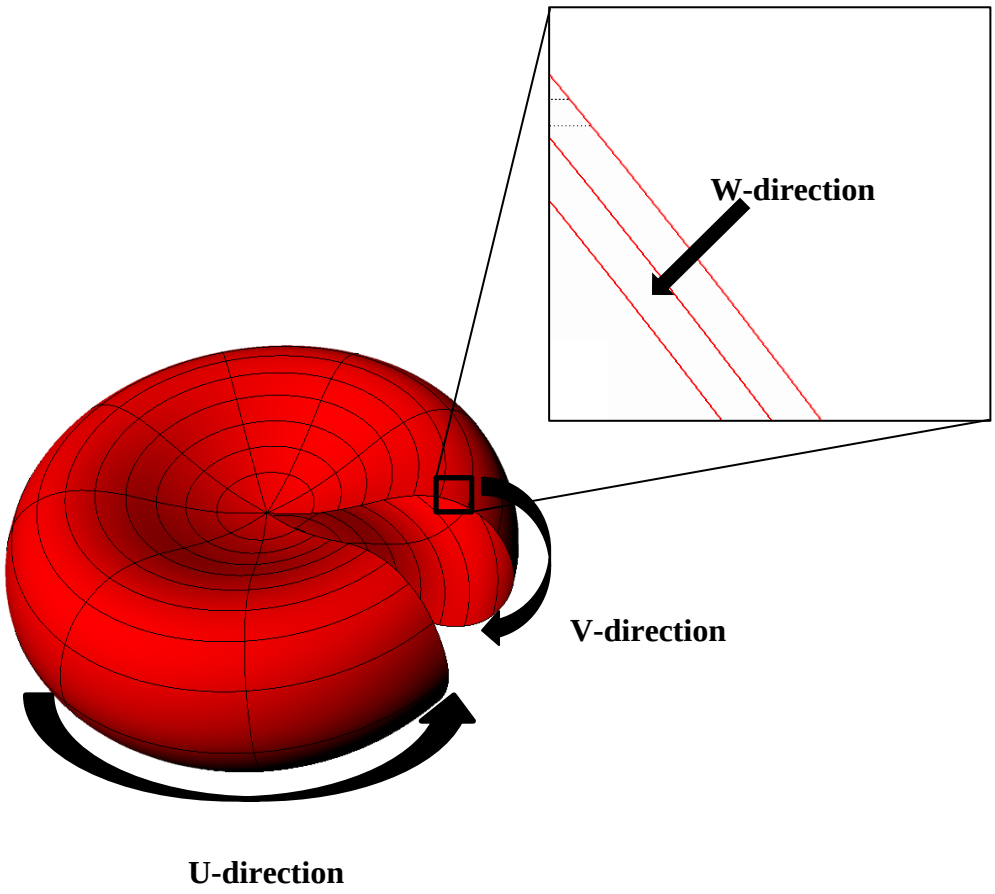

Figure 2-10: 3-D view of bi-cubic NURBS RBC solid model with a portion cut away to show thickness layers for quadratic connectivity across the thickness (inset). The three parametric directions are shown by solid black arrows.

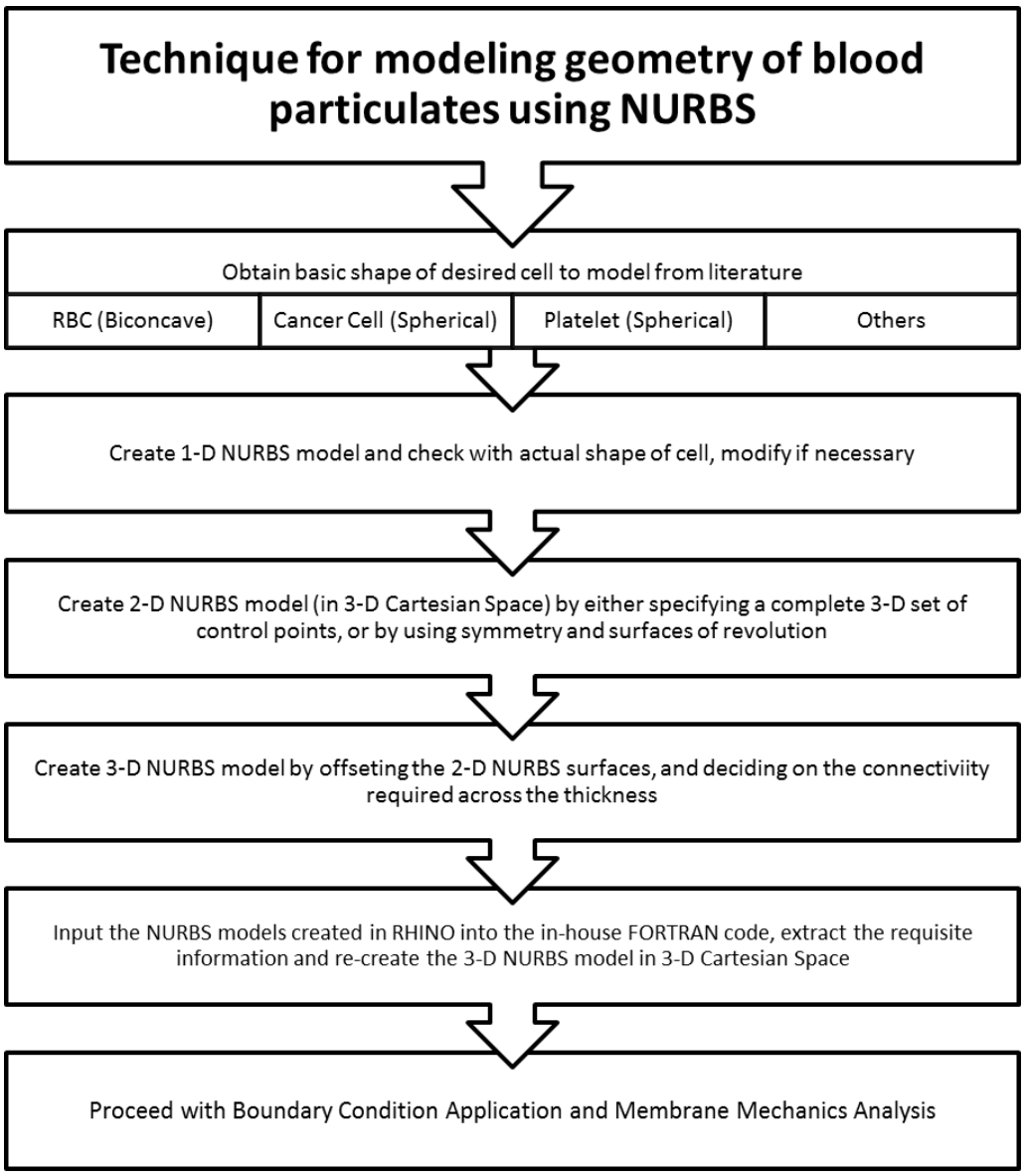

Figure 2-11: Procedure to create geometric models of blood particulates using NURBS.

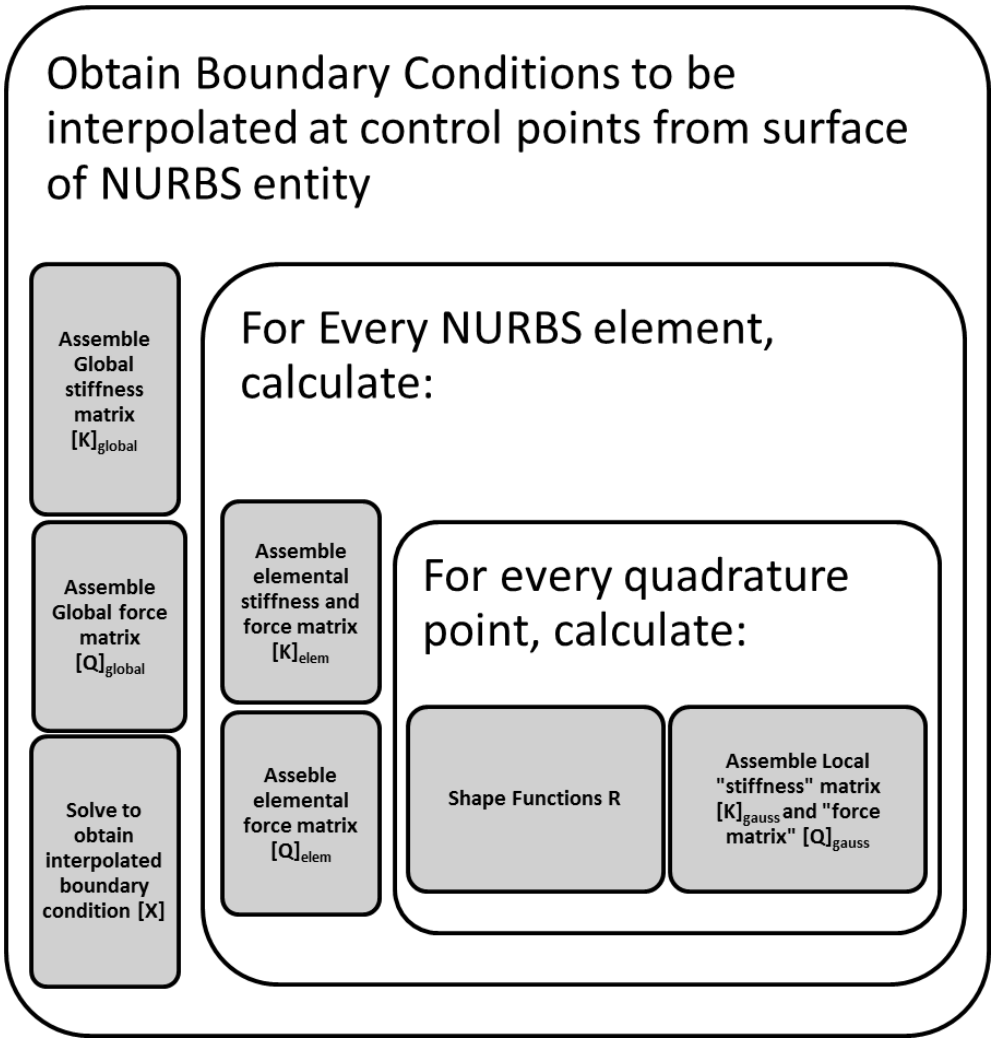

Figure 2-12: General procedure to obtain boundary conditions by interpolating from surface of NURBS entity and applying to control points.

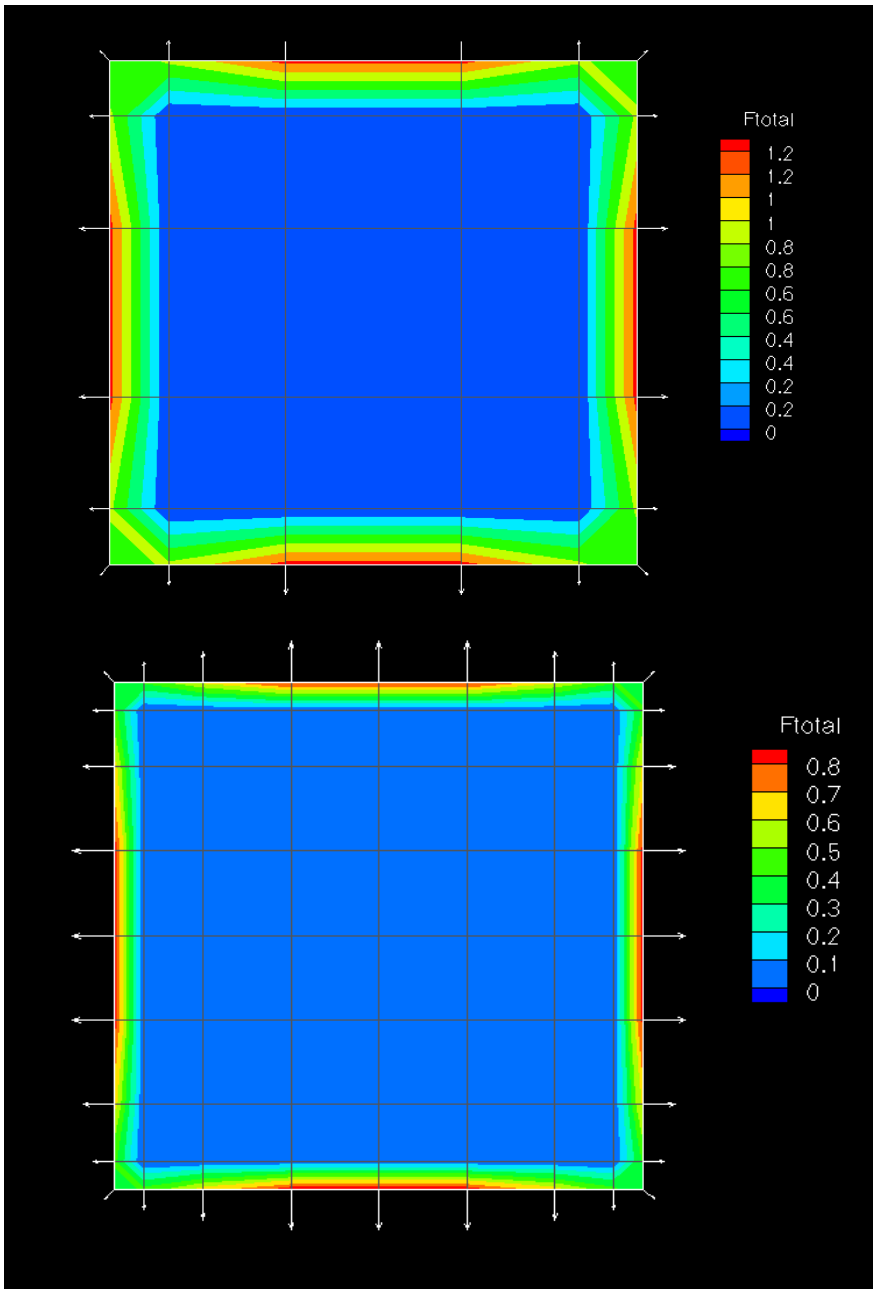

Figure 2-13: NURBS patch test for coarse and fine patches showing zero force for internal elements when subjected to a bilinear displacement field.

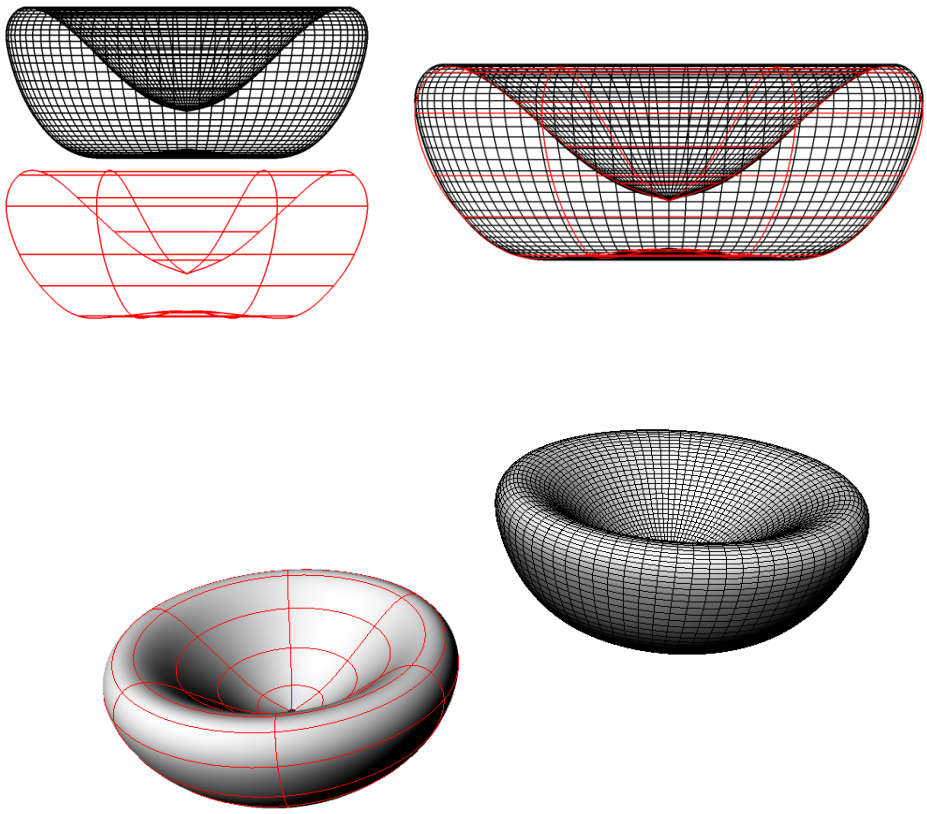

Figure 2-14: Comparison between deformed shapes for coarse (red) mesh with 84 elements and fine (black) mesh with 6400 elements when subjected to analytically prescribed parabolic flow field. The cereal-bowl shape attained is clearly seen, with the deformed shape attained by the fine mesh.

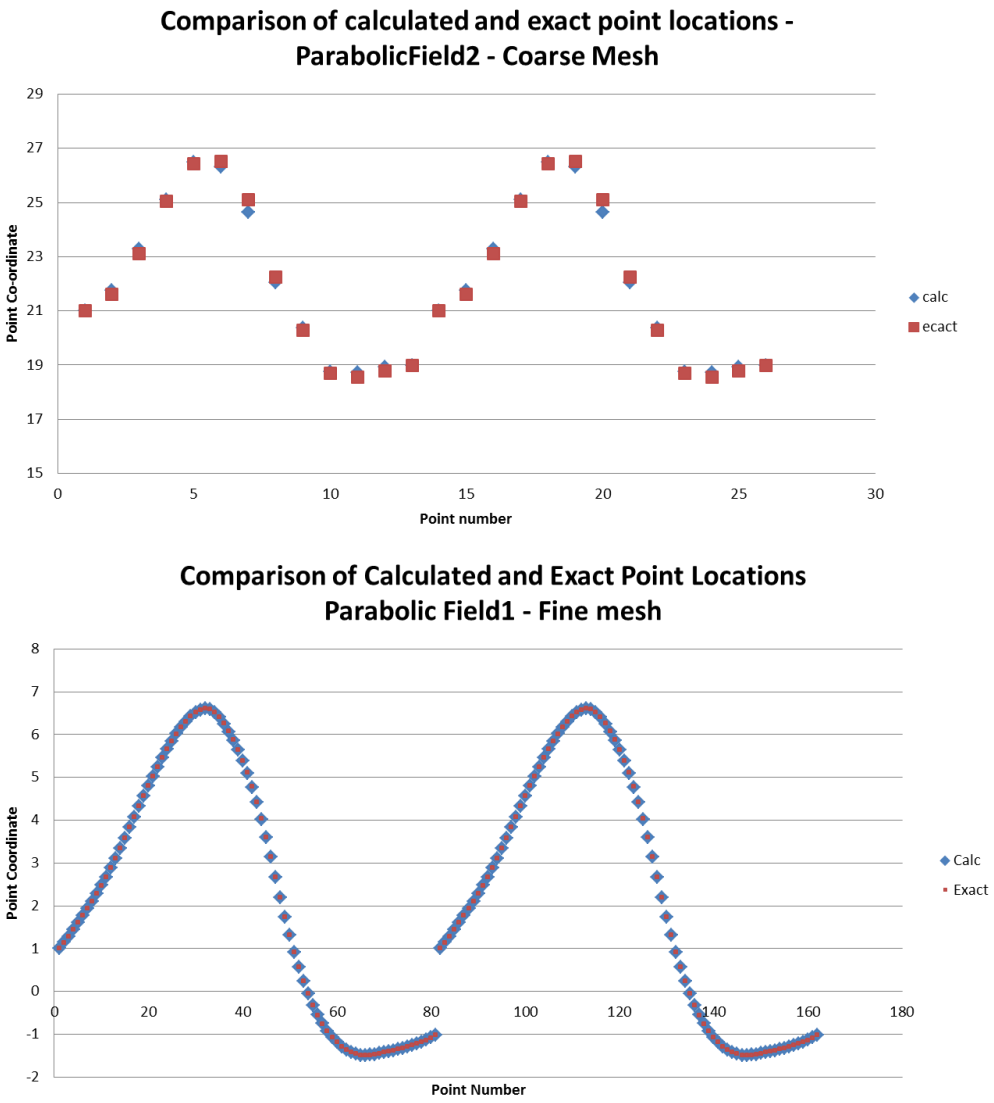

Figure 2-15: Comparing between the exact and calculated locations of surface points to verify least squares interpolation procedure for boundary condition application (Top) Coarse Mesh with 84 elements (Bottom) Fine mesh with 6400 elements.

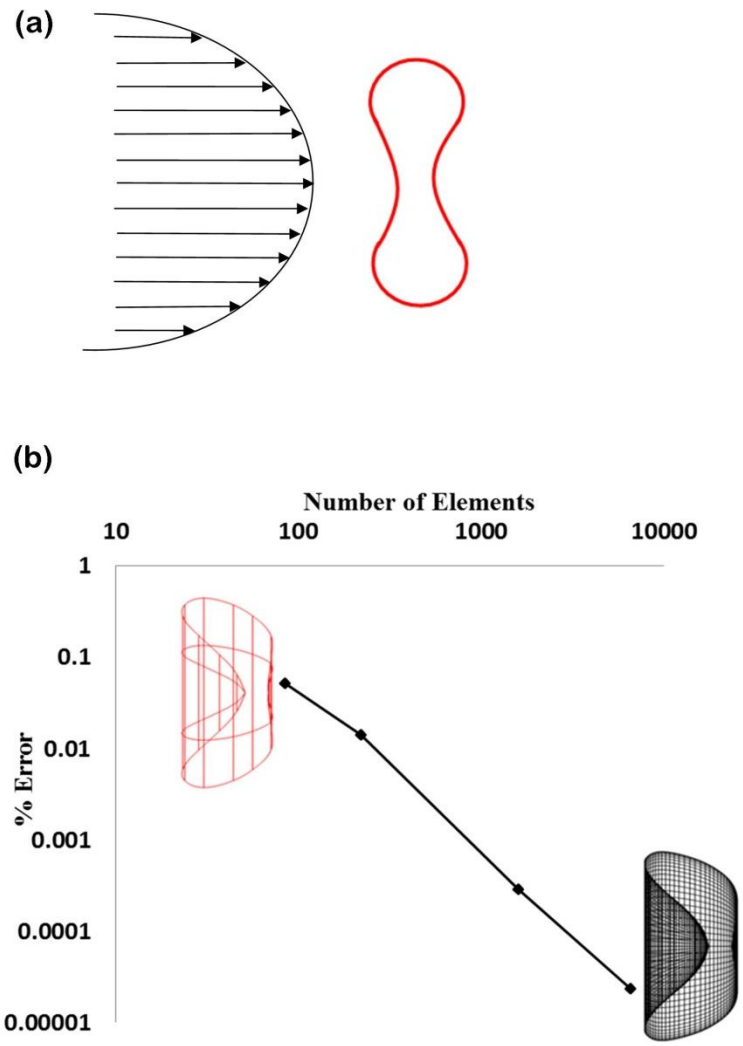

Figure 2-16: Plot of L^2 relative error between the computed locations of the surface points of the RBC and the analytical values in a prescribed Poiseuille flow profile.

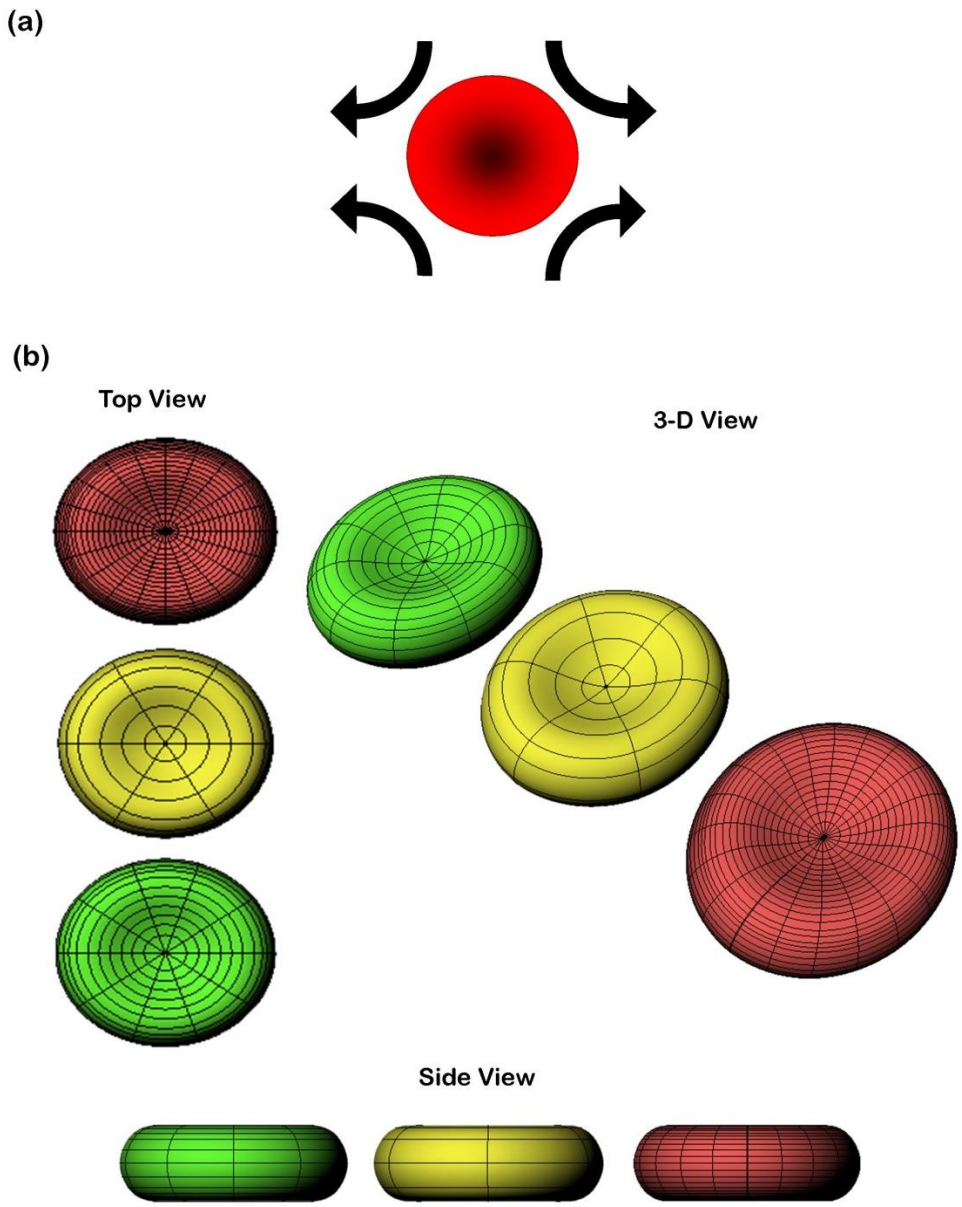

Figure 2-17: Comparison between coarse, medium and fine RBC meshes when subjected to an analytically prescribed straining field and using the least squares method for applying boundary condition (a) Schematic of flow field prescribed (b) Three views of deformed models for coarse mesh with 84 elements (yellow), medium mesh with 440 elements (green) and fine mesh with 1600 elements (red).

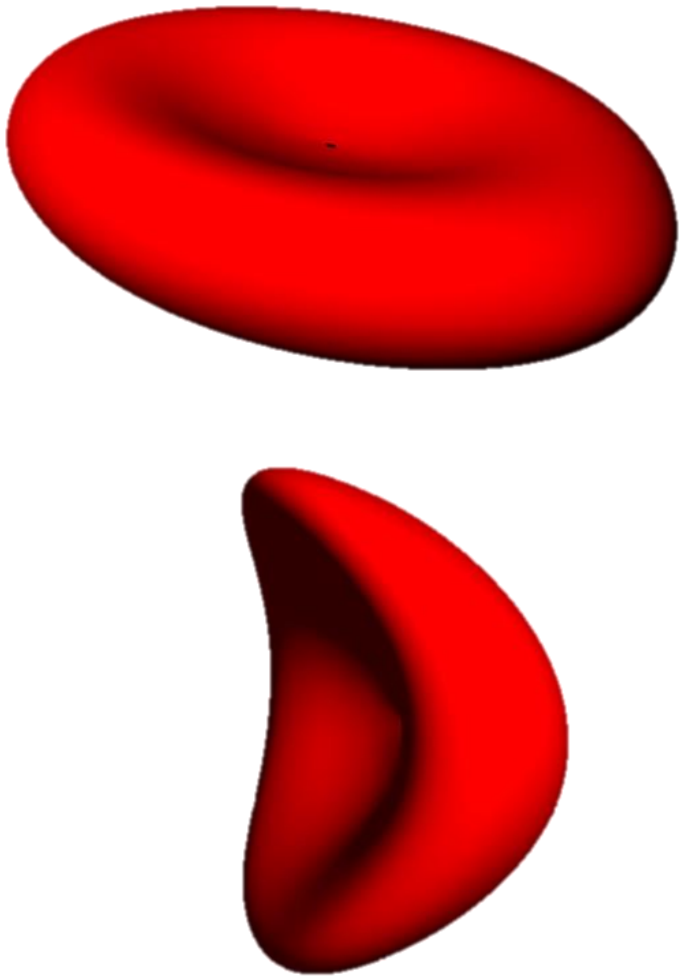

Figure 2-18: Smooth rendered shapes of RBC in straining and parabolic flow using the coarse mesh with 84 elements.

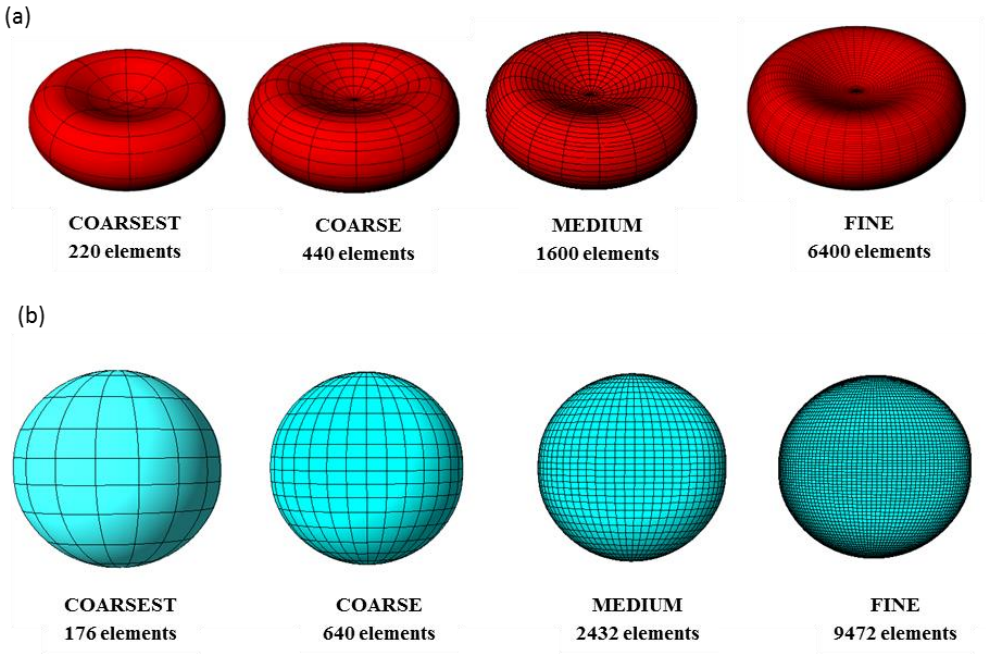

Figure 2-19: Various NURBS meshes created for RBC and sphere (a) 3-D view of the different NURBS meshes created for the RBC. The meshes contain 220, 440, 1600 and 6400 elements respectively, from left to right. (b) 3-D view of the different NURBS meshes created for the spherical cell. The meshes contain 176, 640, 2432 and 9472 elements respectively, from left to right. Note that there is no loss of geometrical resolution as the mesh is coarsened.

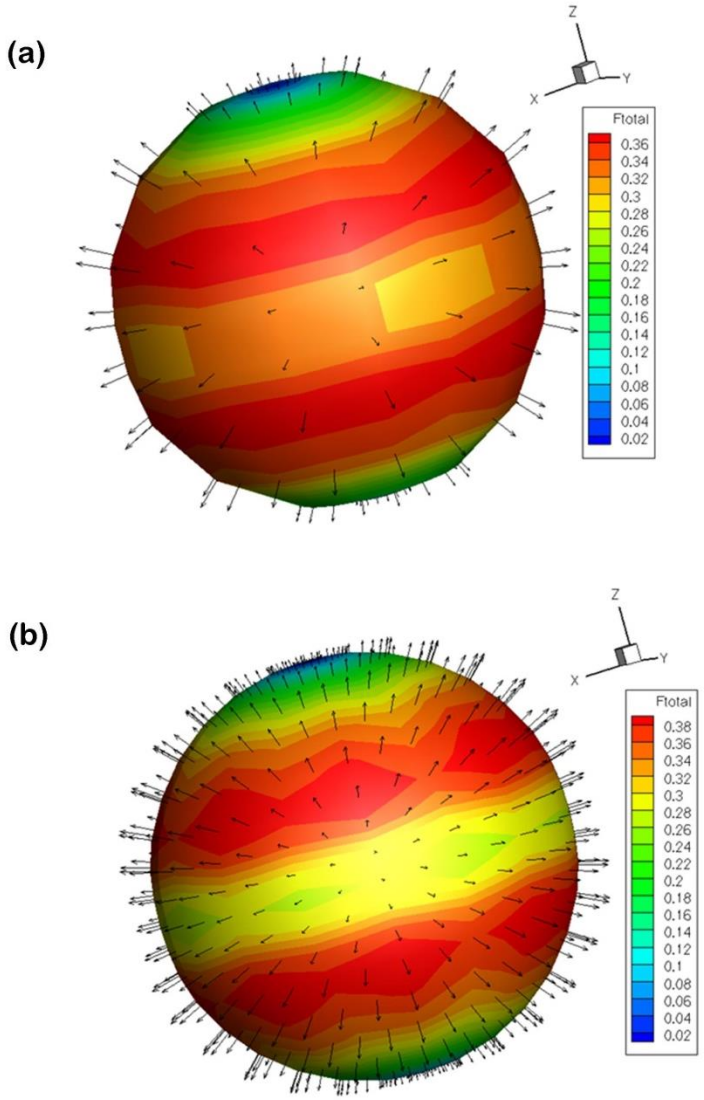

Figure 2-20: Comparison of force distribution over the surface of a spherical NURBS model subjected to uniform expansion (a) Coarse model with 176 elements(b) Fine mesh with 640 elements.

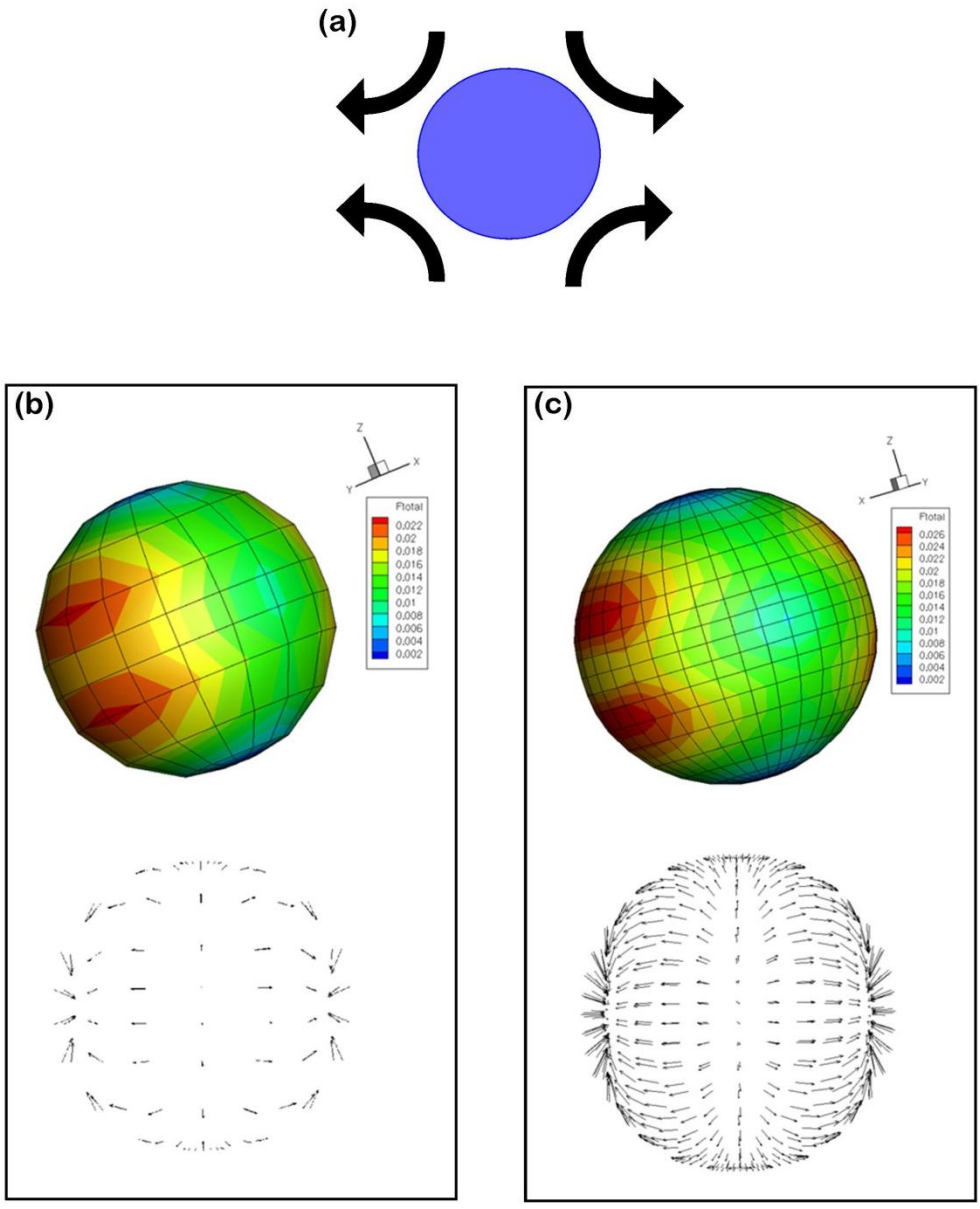

Figure 2-21: Comparison of force distribution and force vectors over the surface of a spherical NURBS model subjected to an analytically prescribed straining field (a) Schematic of flow field (b) Coarse mesh with 176 elements (c) Fine mesh with 640 elements.

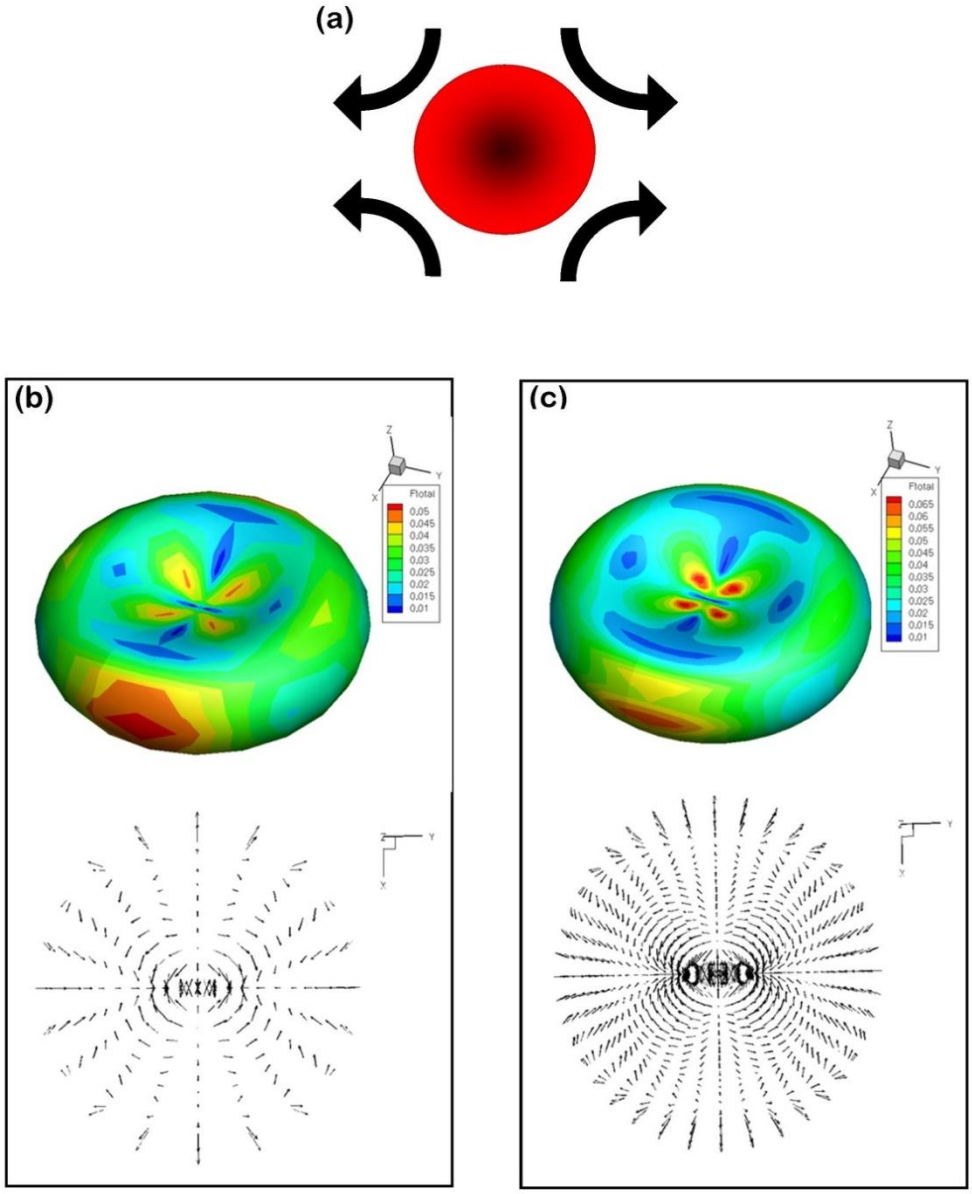

Figure 2-22: Comparison of force distribution and force vectors over the surface of a biconcave RBC NURBS model subjected to an analytically prescribed straining field (a) Schematic of flow field (b) Coarse meshl with 440 elements (c) Fine mesh with 1600 elements.

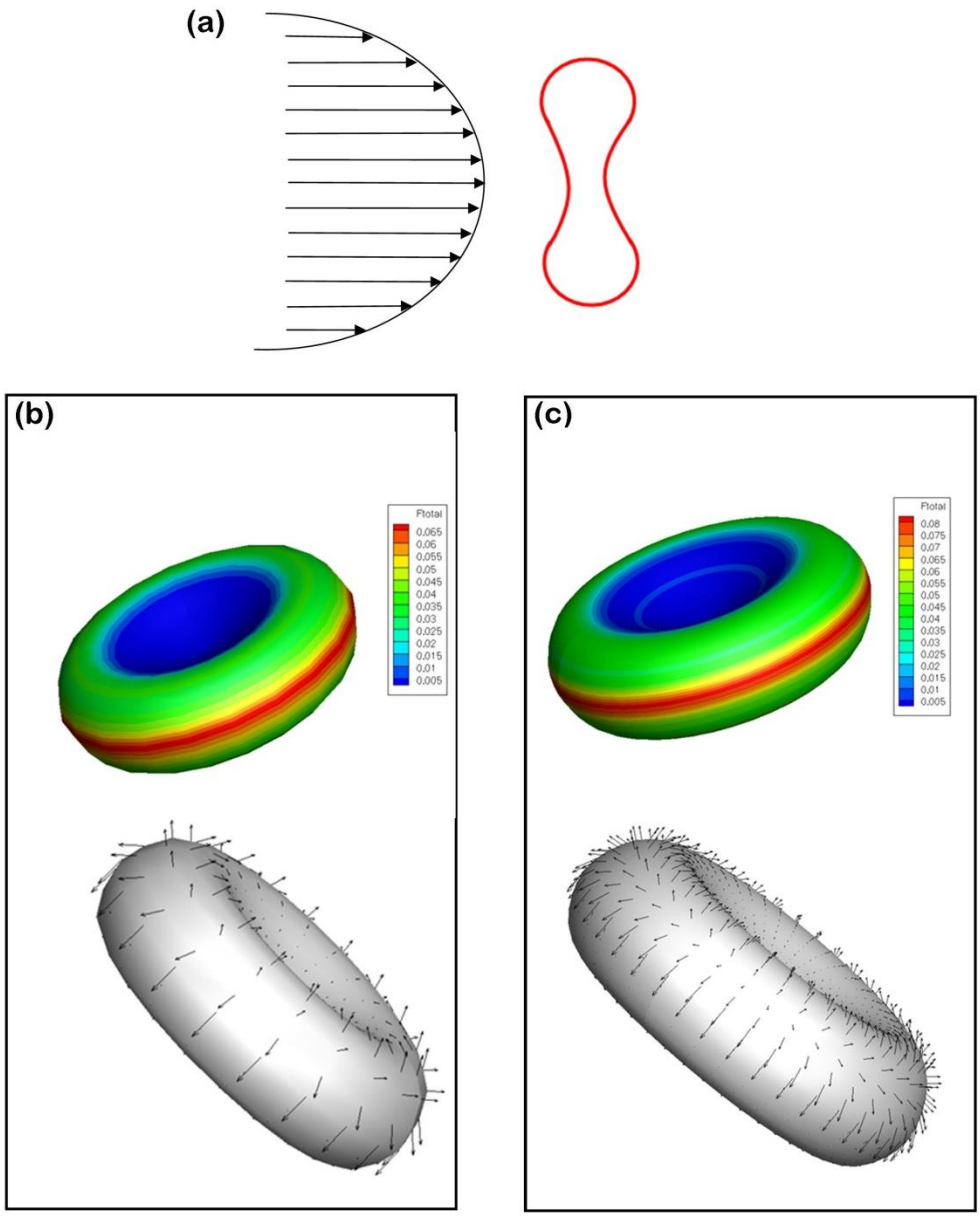

Figure 2-23: Comparison of force distribution and force vectors over the surface of a biconcave RBC NURBS model subjected to an analytically prescribed parabolic flow field (a) Schematic of flow field (b) Coarse mesh with 440 elements (c) Fine mesh with 1600 elements.

CHAPTER 3

CHARACTERIZING PROPERTIES OF CIRCULATING CELLS

3.1 Introduction

Modeling and simulating the behavior of cells in the micro circulation entails knowledge of material properties prior to simulation. Typical circulating cells include the ubiquitous red blood cells, white blood cells or leukocytes and platelets. This chapter provides a brief description of the use of material properties for the aforementioned typical cells which also provides a motivation for determining properties of other application-based circulating cells. Since one of the aims of this research involves attempting to simulate cancer cells in the micro circulation for investigating cancer metastasis, there arises a need for determining material properties of cancer cells. A brief review on what is currently understood about cancer cell material properties is provided, followed by current efforts to determine material properties of suspended cancer cells.

3.2 Characterizing material properties of typical cells in the circulation

3.2.1 Red Blood Cells

The red blood cell (RBC) is the most common of all cells in the circulation. RBCs have captured the interests of researchers for decades, and this section highlights some of the approaches for measuring their properties, beginning in the 1950s [61]. The characteristic biconcave shape of the RBC was researched extensively by Evans and Fung [62] who determined an average RBC to possess a diameter of 7.82 μ, a volume of 94 μ^3 and a surface area of about 135 μ^2. The biconcave shape of the RBC allows it to have roughly 40% more surface area than a sphere of equivalent volume, thereby greatly aiding its function of oxygen transport. There have been multiple approaches taken to determine the material properties of a RBC. Since the RBC is considered to be a

membrane enclosed capsule, it was necessary to determine the property of the membrane that encapsulates the cytoplasm of the RBC. Initial approaches involved swelling the RBC based on osmosis (osmotic swelling), and this technique was used to determine the extent of swelling allowed by the RBC membrane. It was deduced that a radius change of about 7% corresponded to a volume change of about 74%, but the surface area remained roughly the same as the RBC approaches hemolysis. This indicated that the membrane of the RBC is quite resistant to area dilatation, even as it deforms or takes on other shapes. Multiple approaches were used to determine the area dilatation modulus of the RBC membrane – micropipette aspiration, compression plates and deflection by an adhered particle. In micropipette aspiration, the cell was swollen to an almost spherical shape by suspending it in a hypo-osmotic solution. The swollen cell was then partially aspirated into a micropipette thereby giving rise to isotropic tension in the membrane. Using this approach, the area dilatation modulus(K) for a RBC was found to range from 288 - 450 dyn/cm at room temperature [57,63,64].

Along with area dilatation, the RBC membrane was also found to behave in a viscoelastic nature. Using micropipette aspiration again, but this time with normal biconcave RBCs, the dimpled portion of the RBC was partially aspirated to determine the viscoelastic properties for the RBC membrane. This approach was similar to a membrane adhered to glass and the membrane sliding upon the glass in response to an applied force. Using this method, the shear modulus of the RBC membrane(μ) was determined to be 6.6 x 10^{-3} dyn/cm [65]. Other properties of the RBC membrane which were also determined were a characteristic surface viscosity(η) of ~10^{-3} Poise-cm and a membrane bending modulus or bending rigidity (D) of 10^{-12} dyn-cm.

Determining the above properties led researchers to estimate an elastic modulus for the RBC membrane. This modulus is estimated to range from 3.1 x 10^{7} dyn/cm^2 to 3.0 x 10^{8} dyn/cm^2 in a spherical state [66]. Values of an elastic modulus of the RBC membrane in its natural state ranged from 10^{4} dyn/cm^2 [67] to 7.2 x 10^{5} dyn/cm^2 [35].

3.2.2 White Blood Cells

Leukocytes or White Blood Cells (WBCs) are immune system cells which are involved in defending the human body against infectious diseases. The presence of leukocytes vary depending on the level of infection in the human body, and can be further divided into different categories [68]. One type of WBC is a neutrophil which are one of the first to respond to an injury or inflammation, and micropipette aspiration experiments have been performed on neutrophils to determine their mechanical properties. A neutrophil can be thought of as a spherical cell with a diameter of approximately 8 μ[69]. Dong et.al. [70] used a Maxwell-Liquid drop model to model a leukocyte which assumes a cell to be an elastic cell containing a Maxwell viscoelastic fluid. They determined the leukocyte to have an elastic constant (k) of 28.5 N/m^2 , a coefficient of viscosity(μ) of 30 N-s/m^2 and a cortical tension(To) of 0.031 dyn/cm using best fit to experimental data. Based on the nature of their behavior, neutrophils are classified primarily as "liquid" cells which flow into a micropipette upon application of suction beyond a particular value [69]. Others have determined the cortical tension of a neutrophil to range from 0.024 dyn/cm [71] to 0.035 dyn/cm [64]. Neutrophils have also been characterized using a Newtonian liquid drop model and a linear visco-elastic solid model [72].

3.2.3 Platelets

Platelets can be considered to be discoids having a diameter of 2μ. There exists one platelet for every 15 RBCs and these cells play a very important role responding to areas of injury and kick-starting the process of thrombosis in wound-healing [68]. While some approaches have been used to determine material properties of platelets [73] these cells are highly sensitive to stress and take on very different properties when activated. In computational modeling, platelets are typically modeled as rigid particles [27,74] in computational simulations and will not be further discussed in this chapter.

The determination of material properties of the cell membrane has led to various constitutive models to describe the cell's behavior. For RBCs, it was generally accepted that the biconcave shape was the stress-free shape of the RBC [75], but it was also inferred that the RBC membrane was elastic and that it was extremely resistant to area dilatation [35]. Various constitutive models were proposed for the RBC membrane including Mooney-Rivlin, neo-Hookean and others [22]. Leukocyte behavior has been modeled computationally using various approaches. In the compound drop model, the cell is described as having an outer membrane, a shell layer and a core [76]. Other have treated leukocytes as elastic membranes encapsulating an incompressible fluid [77], with additional approached also being exploted [10,78]. As mentioned earlier, platelets are typically modeled in their passive states as rigid particles. A detailed description and analysis of the various laws that have been proposed and used to model cell membranes is given in [79]. The aforementioned material dimensional parameters and material properties for RBCs are tabulated in Table 3-1and for WBCs in Table 3-2 respectively.

While it is clear from the above discussion that the material properties of typical circulating cells viz. RBCs and WBCs have been characterized and modeled, there have been relatively few studies to determine the mechanical properties of cancer cells in suspension. While a large body of research has focused on cancer cell material properties when in an adhered state [80,81], it is important to remember that cancer cells often traverse the circulatory system during the process of metastasizing and their properties when not adhered to a surface(i.e. when the cytoskeleton may not actively be contracting) are anticipated to be different. One of the applications of the current research is to investigate the role of hemodynamic forces during cancer metastasis, and to model these cells, it was necessary to determine the mechanical properties of cancer cells in suspension.

3.3 Background of Cancer Cell Property Investigation

Cancer is extremely dangerous primarily due to its ability to spread (metastasize) to secondary locations through the process of metastasis. Over 90% of the deaths due to cancer are caused by metastasizing tumors rather than primary tumors[82]. A common school of thought about the initiation of metastasis is the seed and soil theory proposed by Paget[3], where it was proposed that cancer cells – the seed- will metastasize under specific conditions depending on the surrounding organs – the soil. Despite being proposed in 1889, Paget's theory is still considered to be a viable explanation, though additional explanations have been proposed which relate metastasis with mechanical loading conditions of the tissue surrounding the site of primary cancer. Once a cancer is initiated at a primary site, various mechanisms are set into motion which lead to its growth, proliferation and ultimately spreading to secondary locations. The major steps in cancer metastasis are as follows – (a) a primary tumor grows at a primary site, (b) proliferation of the tumor cells occur, leading to the creation of new blood vessels to supply nutrients to the tumor (angiogenesis), (c) detachment of cancer cells from the primary tumor and invasion of the cells into the blood circulation and lymphatic circulation, (d) spread of cancer cells to various parts of the body through the aforementioned circulatory systems, (e) adherence of the circulating tumor cells to the lumen of the circulatory vessels in preparation for extravasation, (f) extravasation of the tumor cells to secondary sites, (g) establishing of a viable microenvironment to support tumor growth at the secondary sites and finally (h) metastasis of cancer at secondary sites. A clear review of cancer growth and metastasis can be found in [4].

One of the important aims of this research is to investigate the effect of the environment that a cancer cell is subjected to when in the circulation, namely the effect of fluid shear stress. As described briefly in their paper on the force journey of a cancer cell, the authors [83] mention that the cancer cell is subjected to a host of fluid shear forces among other forces when in the circulation. This exposure of a new set of mechanical

forces hitherto unknown by the cancer cell could possibly effect a change in the mechanical and biochemical properties of the cell. Basson and colleagues [84]investigated the effect of non-laminar shear stress on the adhesive ability of cancer cells and found that shear stress and turbulence may stimulate the adhesion of malignant cells shed by colon cancers by a mechanism that requires both actin-cytoskeletal reorganization and independent physical force activation of a kinase called Src Kinase. The same research group also investigated the effect of pressure on the adhesion of cancer cells and noticed similar behavior [85]. A similar study undertaken by Haier and colleagues [86] also found that shear can enhance phosphorylation (switching on) of a kinase called Focal Adhesion Kinase in colon carcinoma cells thereby leading to increased adhesion of those cells. Previous work [87] established the evidence of a biphasic viability in the survival of prostate cancer cells when exposed to fluid shear stress. In their study, Barnes and colleagues determined that cancer cells seemed to "adapt" to a fluid shear environment, thereby increasing their survivability; while non-cancerous cells were more susceptible to fluid shear stress, and did not change in response to exposure of said stresses. This brings to light an important point that mechanical stimuli leads to biochemical changes in the cell structure which in turn dictates the behavior of the cell.

Determining the mechanical properties of cells – human cells, animal cells or plant cells has been an active area of research over the latter half of the previous century. The basic principle behind investigating mechanical properties is that the cell must be deformed by some known force or stress and its deformation must be measured. Multiple methods to investigate mechanical properties for cells have been developed such as Atomic Force Microscopy(AFM), Optical Tweezers and Micropipette Aspiration. In AFM [73] [88], the cell surface is depressed (indented) by a probe that moves with a constant velocity, thereby providing an increasing force. This force is proportional to the deflection of a beam that is very stiff compared to the apparent stiffness of the cell that is

being deformed. This method is usually restricted to measuring forces around 50pN, however advancement of technology is making possible the application of larger forces. In Optical Tweezers (also known as optical trap), a small bead is captured in an optical trap (laser beam) which is then made to contact a cell surface. Once contacted, the bead is made to move slowly away from its initial position using the laser, thereby extending the surface of the cell where contact has been made [89] [38]. The force of extension is measured by the deflection of the bead in the trap based on its location from the optical axis. Optical tweezers method is very complicated to implement and is quite unstable with respect to bead positioning, laser positioning, etc. Micropipette aspiration was developed by Mitchison and Swan in 1950 [90,91]to measure elastic properties of sea urchin eggs and has become immensely popular due to its versatility, range of applicable forces and its relative simplicity. The micropipette aspiration technique can be used to apply forces over a range of three orders of magnitude – from 10pN to 1nN [69]. No other single method possesses this wide a range. The biggest motivating factor for selecting the micropipette aspiration technique was the fact that the cells can be analyzed in suspension, which is extremely pertinent to investigating cancer metastasis where the cells are traversing the circulation in a suspended state. Micropipette aspiration has been extensively used by researchers to study properties of various cells including the red cell membrane [66], chondrocytes[92], neutrophils[64] and others. Due to the simplicity , versatility and high relevance to investigating cancer metastasis, the micropipette aspiration technique was chosen for investigating the mechanical properties of cancer cells.

3.4 Experimental Methodology

3.4.1 Micropipette Aspiration Technique

The forces needed to deform soft cells such as red cells or white cells are of the order of 10-100pN while those exerted on stiffer cells such as endothelial cells or

chondrocytes are of the order of 1nN [69]. One of the advantages of the micropipette aspiration technique is that it can apply the aforementioned range of forces due to the varying sizes of micropipette diameters employed. The calculation of forces will be described further into this section. The basic idea of micropipette aspiration is that a known force (pressure) is applied on a cell through the mouth of a micropipette onto a cell and to measure the deformation of the cell. Figure 3-1 shows the basic ideology of this technique. In Figure 3-1 (a) a cell is "attracted" towards the micropipette by a suction ΔP applied to the micropipette. Figure 3-1(b) shows a cell that is aspirated partially into the micropipette. The amount of aspiration into the micropipette depends on the suction pressure applied and the membrane properties of the cell.

Cells can be classified into behaving either as a "fluid" or "solid". This is deduced based on the amount of deformation a cell undergoes in response to an applied pressure. The response to either case is similar until a hemispherical projection is formed inside the mouth of the micropipette. Beyond that point, a further increase in suction pressure causes a "liquid-like" cell to flow completely into the micropipette, while a "solid-like" cell will extend its projection into the micropipette until a new equilibrium is attained. The force F on a static cell in a micropipette is given by the following equation:

$$F = \Delta P * \pi {R_p}^2 \tag{3.1}$$

where ΔP is the suction pressure applied and R_p is the radius of the micropipette.

During the process of aspiration, the length of projection of the cell inside the pipette L_p has to be scaled appropriately in order to determine the mechanical properties. Often in literature, L_p is scaled with respect to the radius of the pipette R_p as L_p/R_p. Hence, when this ratio is unity, there exists a hemispherical projection of the cell inside the pipette. Once the length of the projection of the cell is determined, appropriate models can now be implemented to calculate the mechanical properties.

Micropipette aspiration has the advantage of determining if a cell should be classified as a solid or as a fluid with relative ease. When a cell is classified as a fluid, it means that the cell behaves as a liquid drop with constant cortical tension in the membrane. This inference is obtained directly from the Law of Laplace when applied to the suction of a cell into a micropipette until $L_p/R_p = 1$, i.e. when there is a hemispherical projection of the cell inside the micropipette. In this situation, the cortical tension can be determined by the following equation[69]:

$$\Delta P = 2T_c\left(\frac{1}{R_p} - \frac{1}{R_c}\right) \tag{3.2}$$

where R_c is the radius of the cell outside the pipette. The shape of the cell outside the pipette is normally spherical, or is approximated to a sphere in most cases. This is shown schematically in Figure 3-2. This situation is said to be in equilibrium, as any further increase in suction pressure will cause the radius of the cell outside the pipette to decrease and the reciprocal to increase, thereby upsetting the balance of the equation, leading to the cell flowing inside the pipette, a la fluid. Typical values for the cortical tension for a neutrophil (fluid-like cell) were reported to be around 35 pN/μm [69].

However, there are also cells that behave as a solid – i.e. they don't flow freely into the pipette when $L_p/R_p > 1$, but the projection length L_p increases linearly with suction pressure ΔP. This is the case for cells like chondrocytes[92] and endothelial cells[93]. In fact, it was shown that chondrocytes behaved as a solid for values of L_p/R_p that were significantly greater than one. Theret, in his work[93] provided an equation to determine a Young's Modulus for the homogeneous solid

$$\Delta P = \frac{2\pi}{3} E \frac{L_p}{R_p} \phi \tag{3.3}$$

where $E$is the Young's Modulus for the homogeneous solid and ϕ is a term that depends on the ratio of the thickness of the pipette wall to the radius of the pipette and a typical value for $\phi \sim 2.1$. The values of E for endothelial cells ranged from 103-400 pN/ μm^2 [93] and that for chondrocytes was approximately 650 pN/ μm^2 [92].

Hochmuth[69] also proposed a formula to calculate the equivalent cortical tension of a solid cell:

$$T_{c_{equivalent}} = 2.2\,\frac{ER_p}{1-(\frac{R_p}{R_c})} \approx 2.2ER_p \tag{3.4}$$

Using (3.4), it was possible to obtain a value of cortical tension for a solid cell in order to compare the deformability with other cells classified as liquids.

3.4.2 Experimental Setup

This section describes the experimental setup for conducting the aspiration experiment. The major requirements for the setup were as follows:

1. **Micropipette Puller**: This is required to pull micropipettes from capillary tubes Figure 3-3(a). However the end diameter cannot be achieved directly from the micropipette puller, as the requirement for an aspiration pipette is that it should have a long taper and should end in a tip with a constant diameter for at least 6-7 diameter lengths (parallel walls).
2. **MicroForge**: The microforge is used to cleanly cut and polish the end of a micropipette Figure 3-3(b). The micropipettes pulled in the micropipette puller cannot produce a clean break at the required diameter (2-7μ) and hence must be cut and forged under a microforge.
3. **Micromanipulator**: The micromanipulator shown in Figure 3-3(d) is required to manipulate the micropipette under the microscope very carefully so that the pipette tip can be bought in contact with a specific cell to be aspirated. It is imperative that the micromanipulator have a very fine resolution, as micron to sub-micron level motion is required in all three axes.

4. **Pressure Suction Apparatus**: The micropipette aspiration experiment is built on the premise that a prespecified suction pressure can be applied at the tip of the micropipette. It is necessary to have a wide range of suction pressures and to have high resolution. a water reservoir on a stand whose height can be carefully varied was selected to apply suction pressure. The change in height of the reservoir directly transfers to a change in pressure using the canonical relation between height and hydrostatic pressure.
5. **Microscope**: In order to perform the aspiration experiment, unhindered access is required to the cell sample on the slide. This necessitates the use of an inverted microscope rather than a traditional one, due to the ease of access available, shown in Figure 3-3(c).
6. **Camera/Imaging**: Applying a suction pressure is one part of the puzzle. Measuring the radius of the cell inside and outside the pipette along with measuring the radius of the micropipette accurately is very critical to obtaining accurate values for cortical tensions and Young's modulus. This mandates a good imaging system capable of capturing crisp and clear images at a high resolution.

The setup used for the MA procedure consisted of a micropipette puller (Sutter Instruments P-97), a microforge (Narishige MF-900), a micromanipulator (Scientifica LBM-7), thin walled glass capillaries (WPI Inc), a microscope (Nikon TE-300) and a camera (AVT Stingray). Preliminary pipettes were pulled on the micropipette puller and were broken to the desired size using the microforge. The average internal diameter of the micropipette was around 5-8μ, based on the size of the CC. The micropipette was filled with the appropriate media using a microfilling needle (WPI Inc MicroFil) and was connected by Tygon® tubing to a fluid reservoir mounted on a linear scale. The resolution of the linear scale used to change the height of the reservoir was 0.5mm (which corresponded to a pressure change of 4.9 Pa). The micropipette was attached to the

micromanipulator which was mounted on a stand. The micropipette was maneuvered into position just above the cover glass on the microscope platform using the micromanipulator. A schematic of the experimental setup is shown in Figure 3-4.

The micropipette was positioned into place before depositing a small sample of the cell suspension on the cover slip. A cover slip was used instead of a glass slide due to the requirement of needing a larger working depth for the objective to capture the experiment. All experiments were performed at room temperature. The pressure applied to the tip of the micropipette was controlled by raising and lowering the reservoir in reference to the height of the microscope stage. The tip of the micropipette was positioned near a cell using the micromanipulator. A small suction pressure was used (~ 20 Pa) to attract a cell towards the micropipette. This was done not only to attract cells towards the pipette, but also in order to "pick up" the cells from the bottom of the sample in case they settled down. Precaution was taken to ensure that the cell was completely suspended in the sample prior to actually starting the experiment. This methodology is in stark contrast to AFM where the cells are adherent to a slide. Once a cell was identified as satisfactorily attracted to the micropipette tip, the reservoir was lowered very slightly in order to apply increasing amounts of suction pressures via the tip of the micropipette. Images were taken at regular intervals noting the position of the reservoir (and thereby the applied suction pressure) for every cell. The suction pressures were increased until the aspirated portion of the cell began to lose coherence, at which point the experiment for that cell was ceased and a new cell was aspirated. The MA experiments were performed on the cells at rest in order to establish a reference (control) value of the Young's Modulus for comparison with the cells that were exposed to the FSS protocol. For the MA experiments that were performed immediately following the FSS protocol, care was taken to complete the MA experiments within 1 hour of the FSS exposure. The cell was allowed to sit undisturbed in the pipette for a few minutes prior to recording the image of

the cell at a particular pressure, as only the elastic properties were desired in this research.

3.4.3 Fluid Shear Stress Exposure

The FSS exposure protocol is described in detail in [87], however a brief description is provided here for completeness. A dilute suspension of PC cells of concentration upto $5x10^5$ cells/mL was passed through a 30G needle (average internal radius = 7.94 x 10^{-3} cm). A syringe pump (Harvard Apparatus PHD-2000 Infuse/withdraw pump) was used for the experiment. It was calibrated based on the syringe and the needle being used to provide the desired flow rates. A range of flow rates were used, ranging from 20 µL/s to 250 µL/s (corresponding to a Reynolds number range of Re = 159.58 to 1998). The cell suspension was passed up to 10 times through the needle. The cells were expelled at a constant flow rate for a specific pass through the syringe pump; in a few cases manual expulsion was used. The volume fraction of the cell suspension was < 0.2%, thereby facilitating the use of Poiseuille flow relationships in order to estimate the fluid shear stress(FSS). The minimum and maximum FSS experienced by the cell suspension at flow rates of 20 µL/s and 250 µL/s respectively were 510 dyn/cm^2 and 6400 dyn/cm^2. The cells were exposed to both the minimum and maximum flow rates of the syringe pump to determine changes based on flow rates, if any. A schematic of the setup used for the FSS exposure is shown in Figure 3-5.

3.4.4 Cells

The transformed prostate cancer cells (PC-3), and immortalized, non-transformed prostate epithelial cells (PrEC LH) were obtained from our collaborator, Dr.Michael Henry from the University of Iowa Department of Molecular Physiology and Biophysics. Details are given in [87]. Briefly, the cells were sourced from ATCC and Clontech and were cultured in the recommended prescribed manner.

3.5 Results

Cells can be categorized into two categories – solid or fluid based on their response to the suction pressures [69]. The cancer cell exhibited solid-like behavior in that it did not flow into the pipette on increasing the suction pressure applied and hence the elastic model described above was chosen for analysis. The images collected for the cancer cells not exposed to FSS were analyzed to determine the projection length L_p and the radius of the pipette R_p. A typical image sequence collected for an experiment is shown in Figure 3-6.

Typical response curves for the projection length versus the applied suction pressure are shown in Figure 3-7. As can be seen, there exists a linear relationship between the suction pressure ΔP and the projection length L_p. The Young's Modulus(YM) is obtained from the slope of the observed linear relationship between the suction pressure ΔP and the normalized projection length L_p/R_p.

3.5.1 Young's Modulus of Cells at Rest

A suspension of transformed prostate cancer cells (PC-3) and the immortalized epithelial cells (LH) separately was prepared and tested for their mechanical properties at rest, i.e. when not exposed to shear stress. The YM for the PC-3 at rest was **$PC_{unsheared}$ = 19.96 ± 6.77 Pa** *(n=54),* while the YM for PrEC LH cells at rest was **$LH_{unsheared}$ = 47.78 ± 25.15 Pa** *(n=47).* A bar-plot of the Young's Modulus is shown in Figure 3-8.

3.5.2 Young's Modulus of Cells after Exposure to High Shear

The transformed and non-transformed cells were exposed to the highest flow rate that could be applied by the syringe pump. As mentioned above, the cell suspension was passed 10 times through this syringe. The MA experiments were conducted immediately after the cells were exposed to shear stress. The YM for PC-3 cells was **35.35 ± 13.99 Pa**

(n=58) and for PrEC LH cells was **43.7 ± 21.21 Pa (***n = 45).* A summary plot of the YM for both PC-3 and PrEC LH cells is shown in Figure 3-8.

3.5.3 Young's Modulus of Cells after Exposure to Low Shear

The transformed cells (PC-3) were also subjected to low shear to determine the response in elastic modulus, if any. The YM for PC-3 cells after 10 passages through the syringe at low shear was **29.26 ± 10.37 Pa** *(n = 45).*

3.5.4 Young's Modulus of Cancer Cells after Exposure to One Pass at High Shear

The FSS protocol included passing the suspension of cells through the syringe for 10 passes. It was decided to conduct a test of passing the suspension of PC-3 cells through the syringe for 1 pass at the high shear rate and determine the YM to see if there was any change. Upon passing the PC-3 cells for 1 pass at the high shear rate, the YM of PC-3 cells was found to be **27.5 ± 10.0 Pa** *(n = 45).* A summary plot of the YM for the PC-3 cells is shown in Figure 3-9.

3.5.5 Equivalent Cortical Tension

As mentioned earlier, the equivalent cortical tension of all the cells tested thus far was determined using (*). The cortical tension for the unsheared PC-3 cells was found to be **133.8 ± 56.13 x 10^{-6} N/m** *(n=54)* and for the PC-3 cells exposed to 10 passes at high shear it was found to be **203.8 ± 57.2 x 10^{-6} N/m** *(n=58).* The equivalent cortical tension for the unsheared PrEC LH cells was found to be **346.43 ± 199.0 x 10^{-6} N/m** *(n=47).*

The results for all of the aforementioned experiments for both PC-3 and LH cells are tabulated in Table 3-3 and Table 3-4.

3.6 Discussion

The micropipette aspiration technique was successfully applied to investigate the behavior of PC-3 cells and PrEC LH cells both at rest and after being exposed to FSS. The use of MA is important in that it is one of the few methods in which the mechanical properties of the cell can be investigated when the cell is in suspension. This is very pertinent to the current research, where it is attempted to determine the effect of FSS on the PC-3 cells during the spread of PC-3 cells from the primary tumor to a secondary site via the circulatory systems (blood and lymphatic). The range of FSS to which the PC-3 cells were exposed is a physiological range which they can expect to see when in the microcirculation [87]. Moreover, the biphasic viability displayed by the PC-3 cells indicated that they adapted to the FSS.

Firstly, our study found that at rest, the Young's Modulus of PrEC LH is about 130% stiffer than PC-3 cells, with the distribution of PC-3 cells about four times narrower than the PrEC LH cells. This compares well with other researchers who have used Atomic Force Microscopy to determine the Young's Modulus [80,81,94–96] and found that the PrEC LH cells were ~80% stiffer than transformed cells and that the distribution of the PrEC LH cells was six times that of the transformed cells.

Until now, the impact of FSS exposure on the Young's Modulus of Cancer Cells has not been investigated. Using micropipette aspiration, we examined how FSS exposure impacts the Young's Modulus of cells. We found that the Young's Modulus of PC-3 cells exposed to high FSS was almost double that of the PC-3 cells at rest, i.e. there was an almost 80% increase in the Young's Modulus upon exposure to high FSS. After exposing the PC-3 cells to $1/10^{th}$ the shear rate (Low Shear), we found the Young's Modulus to increase by ~45% after 10 passages through the syringe. The Young's Modulus of the PC-3 cells after exposure to only 1 pass at high shear was found to be very similar to the Young's Modulus after 10 passages at high shear. This indicates that the PC-3 cells seem to display a graded response to the magnitude of FSS. The acquired

stiffness of the PC-3 cells was dependent on the level of FSS exposure, with increasing exposure resulting in a higher Young's Modulus.

Interestingly, the change in the survivability of PC-3 cells after exposure to low shear was found to be shear dependent [87], so that at low levels of fluid shear, most of the PC-3 cells (~90%) survived after 10 passages through the syringe. This contrasts starkly with the behavior of PC-3 cells upon exposure to high shear, where they show a biphasic survival and only ~55% of the PC-3 cells survive at this high rate of shear after 10 passages through the syringe. In addition, the survival and the Young's Modulus of PC-3 cells after 1 passage at high shear (250 µL/s) was similar to the survival of PC-3 cells after 10 passages at low shear (20 µL/s). In contrast, there was no significant change in the Young's Modulus of PrEC LH cells upon shear exposure, indicating that the stiffening is a phenomenon only present in cancerous cells. A histogram of the Young's Modulus is shown in Figure 3-11 and a dot plot showing all the data points and the spread of data for PC-3 cells is shown in Figure 3-10.

The equivalent cortical tension for the aforementioned cells was also calculated as per [69]. Though it is not an actual cortical tension as the cells are classified as a homogeneous solid, it nevertheless provides a means to compare the deformability against more fluid-like cells. The cortical tension for the PC-3 cells at rest was almost 4 times that of neutrophils [69]. As the PC-3 cells stiffened themselves upon shear exposure, the cortical tension of PC-3 cells after exposure to high shear was almost 6 times that of a neutrophil. The cortical tension of the PrEC LH cells was almost 10 times that of neutrophils. Conversely, the equivalent cortical tension of the PC-3 and PrEC LH cells were an order of magnitude lower than that obtained for endothelial cells, whose cortical tension was found to be ~100 times greater than neutrophils. This indicates that while the PC-3 and PrEC LH cells are definitely stiffer than neutrophils, they are much more compliant as compared to other cells characterized as a solid like endothelial cells [93] or chondrocytes [92]. Thus from the perspective of flow behavior, the values of

cortical tension obtained in this way could shed light on how PC-3 cells behave in the microcirculation in comparison to other circulating cells like neutrophils and RBCs.

An interesting hypothesis that may be postulated is based on the values of Young's Modulus for the PC-3 cells at low shear (10 passes), high shear (1 pass) and at high shear(10 passes). The flow rates used for the low shear runs were $1/10^{th}$ that of the flow rates used for the high shear runs. Coincidently, the Young's Modulus for the PC-3 cells exposed to 10 passes at low shear overlap almost exactly with the Young's Modulus for the PC-3 cells exposed to 1 pass at high shear. This hypothesis that could be postulated is that the PC-3 cells exhibit not only an acquired response to fluid shear, but that the response is cumulative based on the levels and exposure time of fluid shear stress. However much more testing needs to be done in order to confirm this hypothesis.

It has been recognized that not all the cancer cells that enter the bloodstream will actually contribute towards metastatic growth [97]. This metastatic inefficiency coupled with the death of a majority of the circulating tumor cells within a few hours of entering the circulation has been well documented phenomenon [4,97–99]. It is also known that cancer cells undergo extensive modifications in their cytoskeleton prior to intravasation into the circulatory system [100–102]. In their review on the physics of cancer metastasis, the authors [82] mention that shear stress is one possible factor that impacts the distal metastasis site. However, they acknowledge that information regarding the behavior of cancer cells in response to fluid shear stress is still extremely limited.

The histogram of the Young's Modulus of the cells in Figure 3-11 indicate a much wider range of Young's Modulus for the PC-3 cells exposed to FSS as opposed to the control group. There could be multiple reasons for the same, one of which is a simple explanation that not all the cells are exposed to the same levels of FSS upon passage through the needle, a result of the expected parabolic (Poiuiselle) flow profile. Another possible explanation is the fact that different cells are adapting differently, based on their ability to withstand FSS. This might also provide insight into the survival of only a few

PC-3 cells that enter the circulation. A third, equally plausible explanation could be that the PC-3 cells tested were in different stages in their mitosis cycle, and hence were of differing maturity when tested, leading to uneven response to FSS.

The current study is one of the first studies to investigate the effect of FSS on the mechanical properties of cancer cells using the micropipette aspiration technique. The importance of this technique is underscored by the fact that during metastasis, the cancer cells enter the circulation and are in a suspended state until they extravasate to a secondary site. Thus the findings of this study are highly relevant to cancer metastasis. We have determined that PC-3 cells display varying levels of stiffening based on the magnitude of fluid shear stress that they are exposed to. We have also shown that this stiffening appears to be limited to cancer cells only and is not present in non-transformed cells. The fact that almost 90% of the PrEC LH cells die after the FSS protocol suggests that the PrEC LH cells are not able to withstand let alone adapt to the FSS environment. On the other hand, PC-3 cells change their properties and appear to become increasingly resistant to FSS exposure. Moreover, the PC-3 cells display a lesser change in their Young's Modulus when exposed to low shear in comparison to high shear, where they exhibit a biphasic viability curve and a lower survival rate.

The circulatory system is a harsh environment [83] where fluid shear stresses abound. Our study sought to investigate the effect of fluid shear stress on the mechanical properties of cancer cells by subjecting them to flows of Reynolds numbers from 100 - 2000 . This corresponds to a fluid shear stress range of 500 dyn/cm^2 – 6400 dyn/cm^2. While the average shear stress in typical arterial circulation is ~ 15 dyn/cm^2, the local fluid shear stress can be as much as 3000 dyn/cm^2 near the walls of large vessels, turbulent blood flow, near the presence of mechanical prostheses and during atherosclerosis [2,103]. Our study found that PC-3 seems to adapt itself to FSS by making itself upto 80% stiffer after exposure to the aforementioned range of shear stress. While the stiffening of cells could be one of the manifestations of a cellular level

response to fluid shear stress, this could enable the survival of a select few cancer cells which then go on to metastasize. Thus our study on elastic property change could possibly be used a stepping stone towards diagnosing cancer metastasis, along with other mechanical properties such as viscoelasticity [95].

3.7 Summary and Future Work

The objective of the current chapter was to explore the material properties of various cells in the circulation. While the material properties of RBCs and WBCs in the circulation have been characterized in the literature, there is still a dearth of information for cancer cells in the circulation. Hence it was decided to undertake a related secondary project to determine the material properties of cancer cells especially when exposed to fluid shear.

In the present study, we have observed that cancer cells appear to stiffen upon exposure to fluid shear stress. This stiffening appears to be graded based on the magnitude of fluid shear stress exposure. Interestingly, this is stark contrast to the behavior of LH cells which do not show any change in Young's Modulus upon fluid shear stress exposure. The observation that the stiffening is a cancer cell-only phenomenon sheds new light on the behavior of cancer cells during metastasis. Mechanical stimuli has been shown to be responsible for inducing a biochemical response related to increased potential for PC-3 cell adhesion and extravasation to secondary sites [84–86]. While our study described the cell as simply an elastic continuum, it provides significant insights into the response of cancer cells to fluid shear and must be investigated further. We anticipate that determining the viscoelastic properties of cancer cells exposed to fluid shear would be the next logical step, along with using more complex models to describe the cytoskeletal structure. It is important to acknowledge that the micropipette aspiration technique is ideally suited to investigating the mechanical properties of a cell in suspension, which is highly pertinent to cancer

metastasis research. While the perceived change in the elastic modulus of cancer cells exposed to fluid shear may not be conclusive that stiffening is the intended response, it sheds new light on shear induced mechanical responses of cancerous cells and could potentially be used for diagnostic purposes, and possibly develop new strategies to combat cancer. Moreover, the values of Young's Modulus for the PC-3 cells seem to point towards a cumulative response hypothesis, which could also contribute to our understanding of the behavior of circulating cancer cells. The over-arching goal of the current research to obtain and use the mechanical properties of cancer cells in computational simulations of cancer metastasis is one of the novel approaches that could be used to gain more understanding about the physics of cancer.

CELL TYPE	RBC
Shape	Biconcave
Diameter (μm)	7.85
Thickness (μm)	2.58
Surface Area (μm^2)	135
Volume (μm^3)	94
Area Dilatation Modulus K (dyn/cm)	450
Shear Modulus μ (dyn/cm)	6.6×10^{-3}
Bending Rigidity D (dyn-cm)	10^{-12}
Elastic Modulus E (Pa)	3.1×10^{7}

Table 3-1: Typical values for material properties of RBCs [61]

CELL TYPE	Neutrophil (WBC)
Shape	Spherical
Diameter (μm)	8
Cortical Tension T_o (dyn/cm)	0.031 – 0.035

Table 3-2: Typical values obtained for material properties for WBCs[61,69]

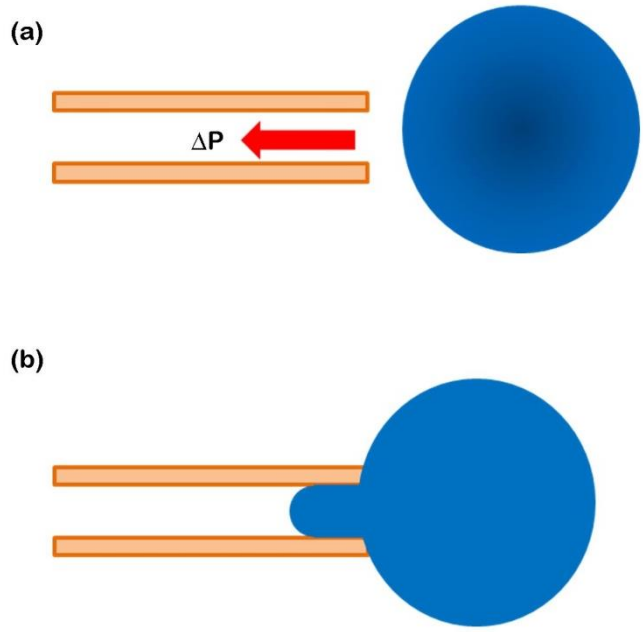

Figure 3-1: 2-D Schematic showing micropipette aspiration (a) A micropipette is manipulated towards the cell and a small suction pressure is applied (b) The cell gets partially aspirated in the micropipette, with the projection length depending on the suction pressure.

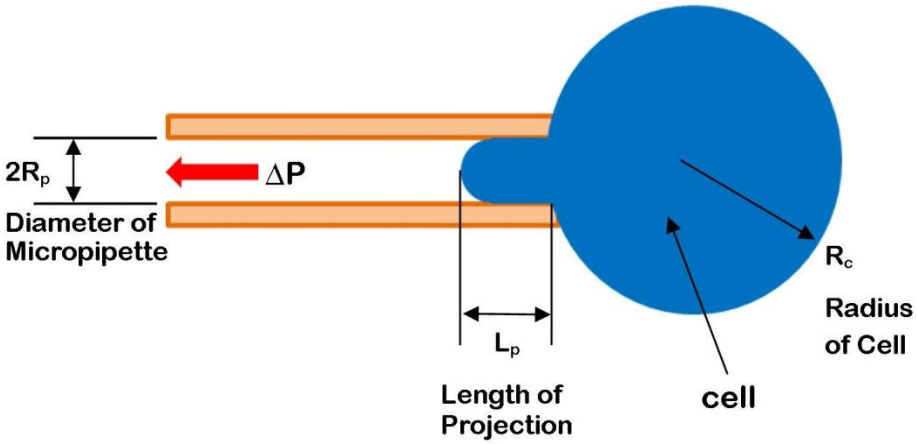

Figure 3-2: 2-D Schematic showing micropipette aspiration of a cell with relevant measurements indicated.

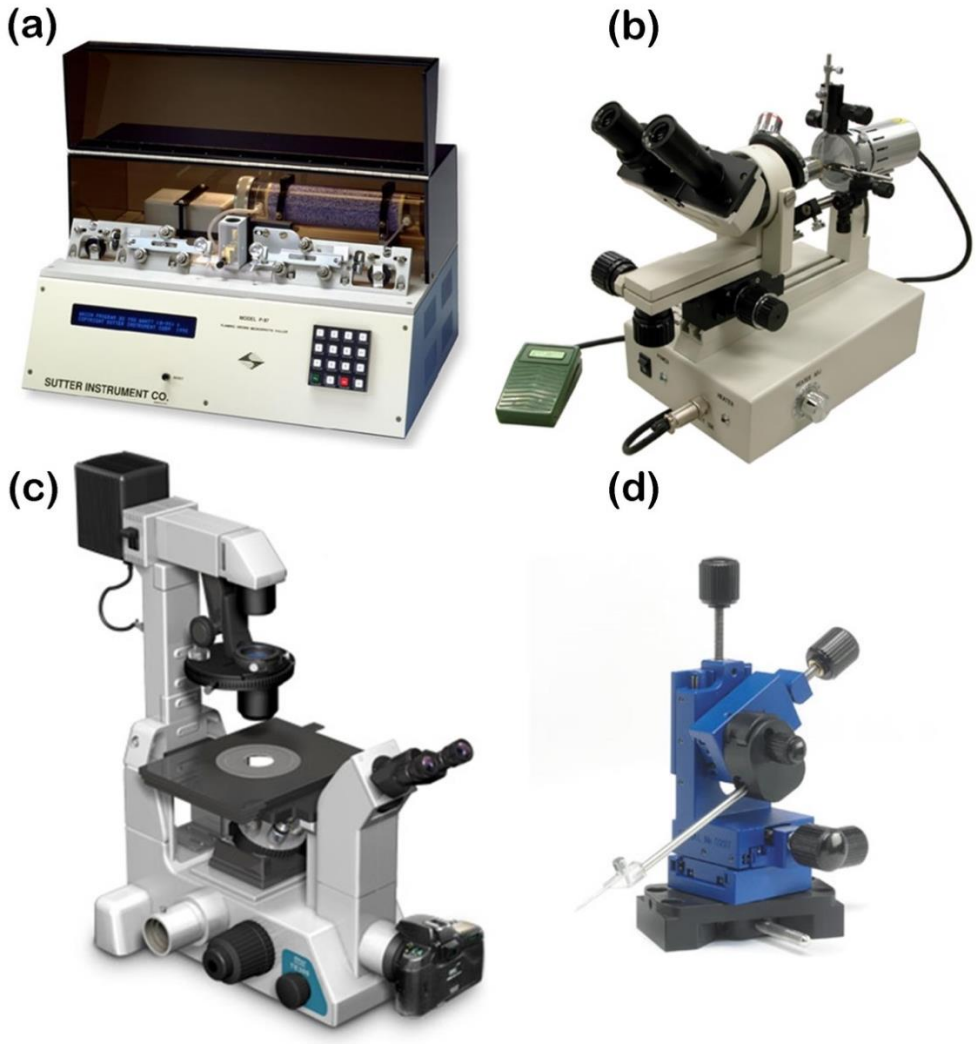

Figure 3-3: Some of the main apparatus used for micropipette aspiration: (a) Micropipette puller (Sutter Instruments P-97) (b) Micro Forge (Narishige MF900) (c) Inverted Microscope (Nikon TE-300) (d) Micromanipulator (Scientifica Little Blue).

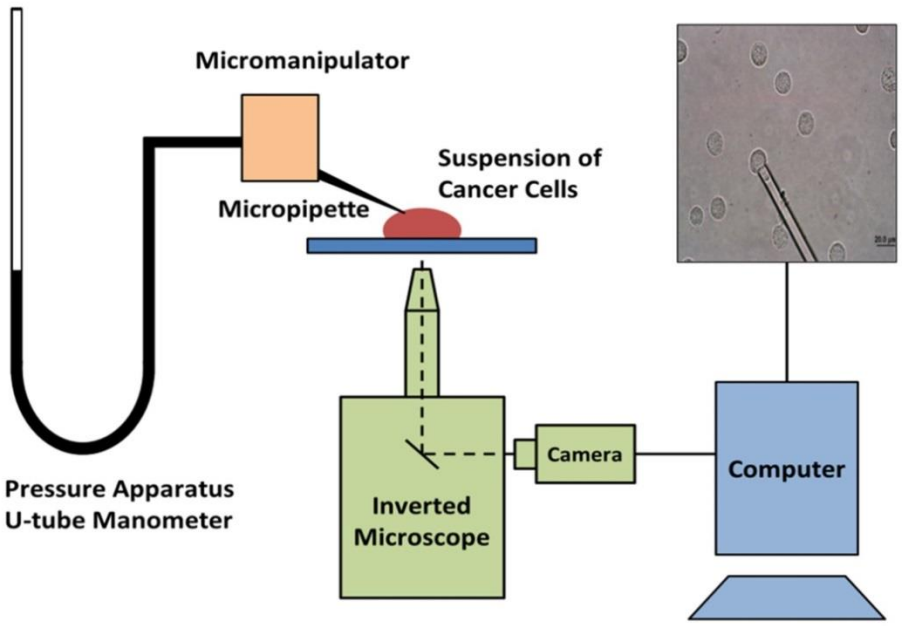

Figure 3-4: Schematic of Experimental Setup to perform Micropipette Aspiration experiments.

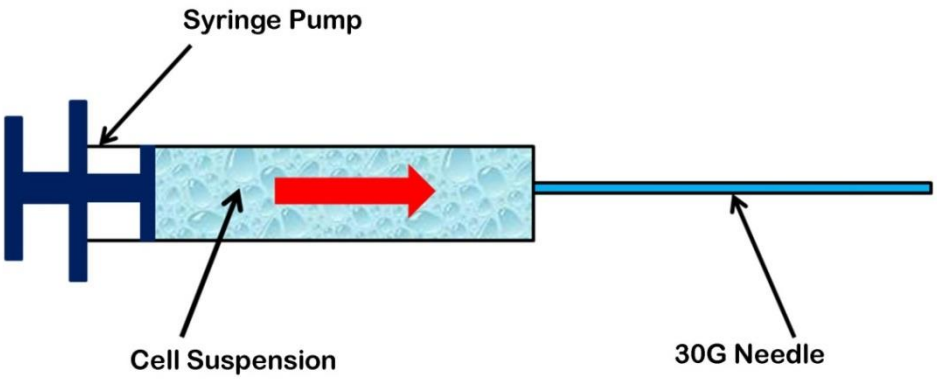

Figure 3-5: Schematic of Setup for Fluid Shear Stress Exposure.

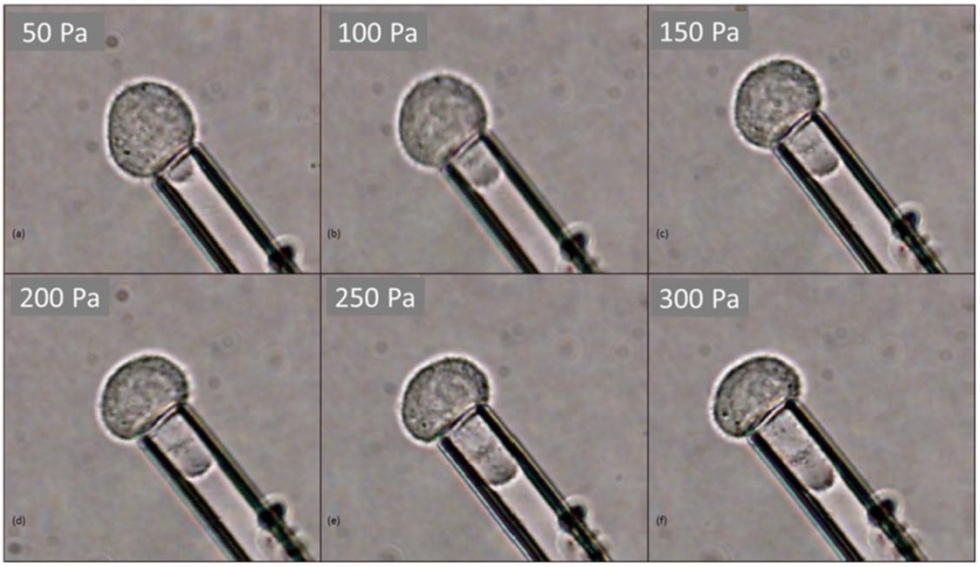

Figure 3-6: Typical sequence of images collected for an aspiration experiment. Suction pressures are mentioned on the top left in every image.

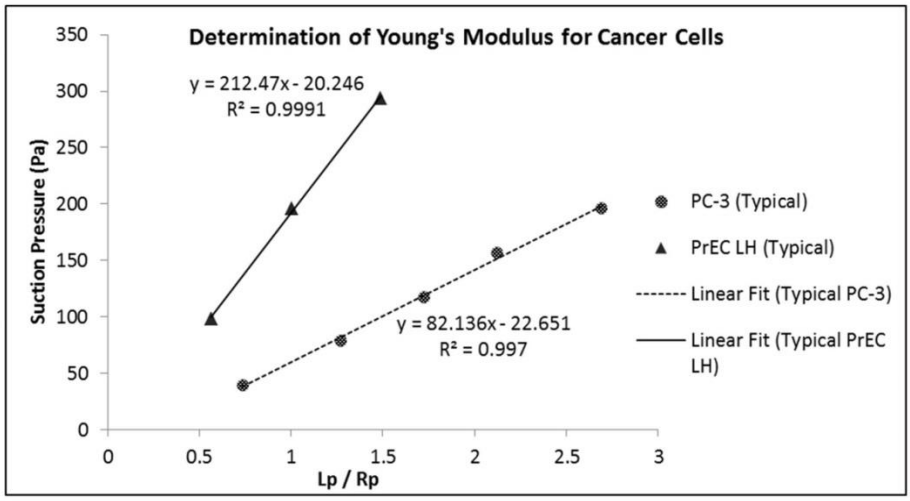

Figure 3-7: Typical results for relationship of suction pressure and length of projection of the cell inside the pipette. The length of projection is normalized by the radius of the pipette. The Young's Modulus is obtained from the slope of the linear fits.

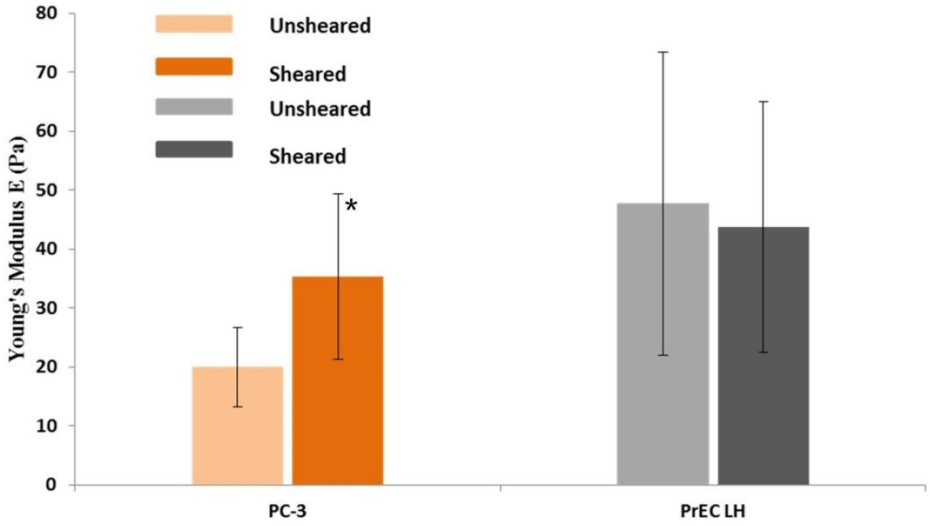

Figure 3-8: Comparison of Young's Modulus for Transformed and Non-transformed cancer cells at rest and after exposure to high shear. There is a ~77% increase in the Young's Modulus of Transformed cells after being exposed to high shear, but no discernible change can be seen for the Non-Transformed Cells. * *denotes $p<0.05$*

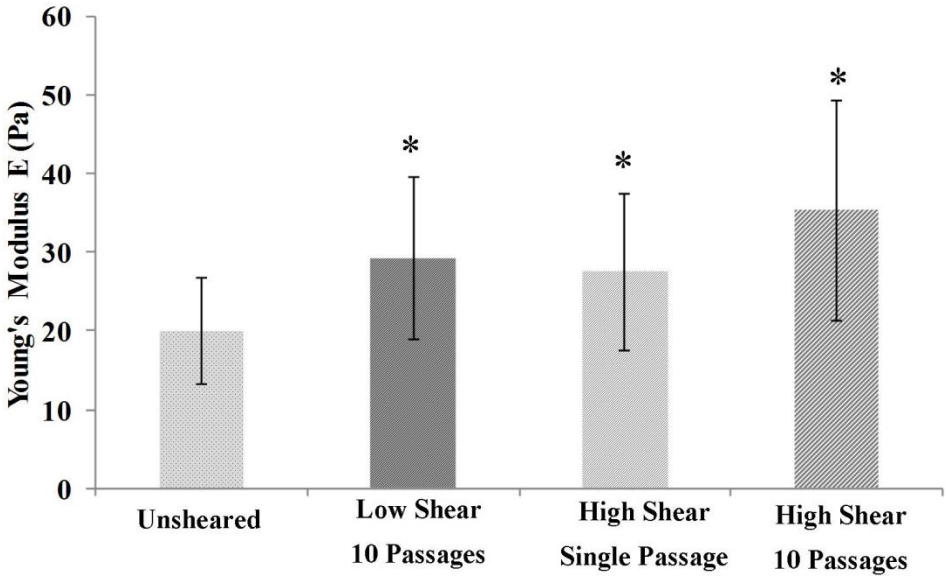

Figure 3-9: Comparison of Young's Modulus for Transformed at rest, after exposure to 10 passages at high shear, after exposure to 10 passages at low shear and after exposure to a single pass at high shear. There appears to be a graded response to the level of fluid shear stress that the cancer cells are exposed to. * *denotes* $p<0.05$

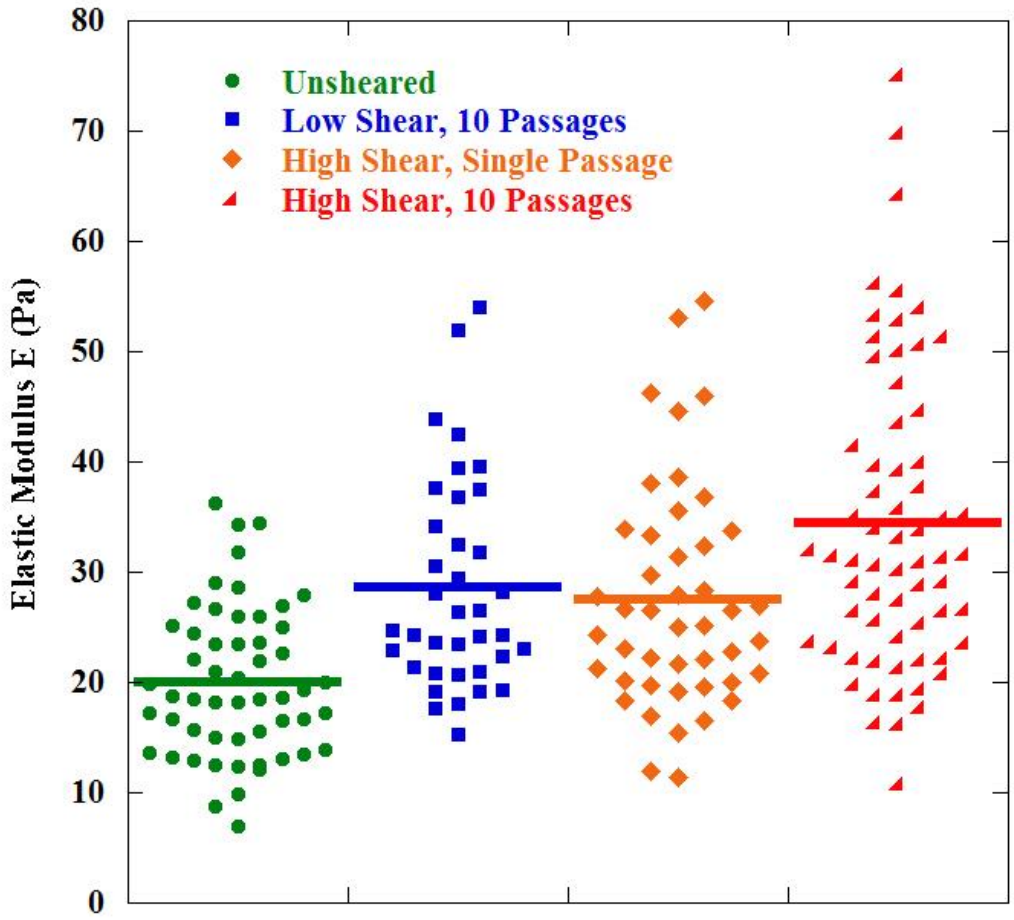

Figure 3-10: Dot Plot showing all data points collected for all PC cells (unsheared, low shear 10 passages, high shear single passage and high shear 10 pasages).

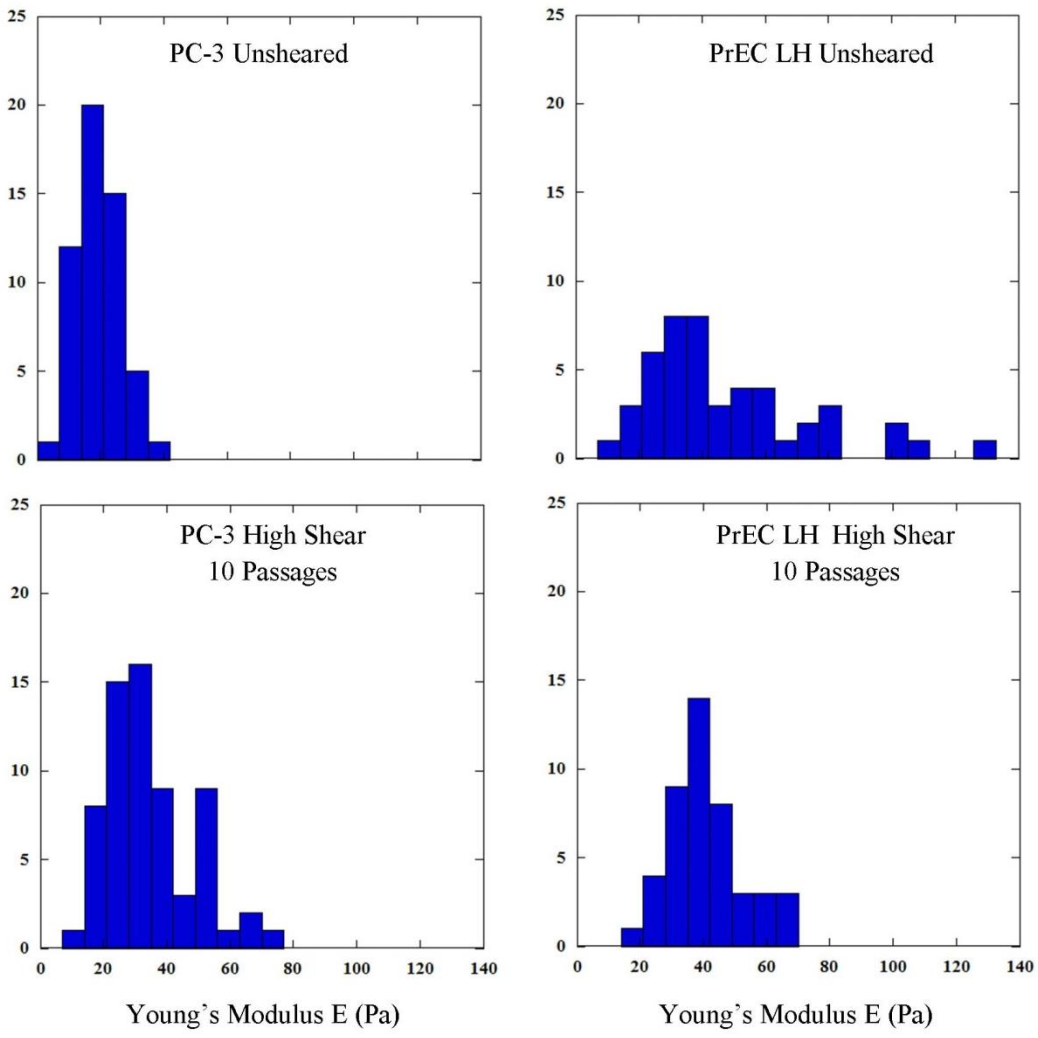

Figure 3-11: Comparison of Histogram of Young's Modulus(E) for unsheared and sheared PC cells and LH cells. The different distributions of data can be clearly seen. The standard deviation of the PC unsheared cells is over six times smaller than the unsheared PrEC LH cells.

Cell type (Description)	Elastic Modulus (Pa)	% difference compared to unsheared *p<0.05
PrEC LH (Unsheared)	47.72 ± 25.7 Pa *(n=47)*	N/A
PrEC LH (10 Passes, High Shear)	43.7 ± 21.21 Pa *(n = 45)*	4% decrease
PC-3 (Unsheared)	19.76 ± 6.77 Pa *(n=54)*	N/A
PC-3 (Low Shear)	29.26 ± 10.37 Pa *(n = 45)*	48% increase *
PC-3 (Single Pass, High Shear)	27.5 ± 10.0 Pa *(n = 45)*	46% increase *
PC-3 (10 Passes, High Shear)	35.35 ± 13.99 Pa *(n = 58)*	77% increase *

Table 3-3: Elastic Moduli obtained for both PC-3 and PrEC LH cells for the case of not being exposed to shear and after being exposed to different levels of shear

Cell type (Description)	Equivalent Cortical Tension (μN/m)
PrEC LH (Unsheared)	346.43 ± 199.0 (*n=47)*
PrEC LH (10 Passes, High Shear)	--
PC-3 (Unsheared)	133.8 ± 56.13 *(n=54)*
PC-3 (Low Shear)	227.6 ± 85.33 *(n = 45)*
PC-3 (Single Pass, High Shear)	229.05 ± 79.75 *(n = 45)*
PC-3 (10 Passes, High Shear)	203.3 ± 96.7 *(n = 58)*

Table 3-4: Equivalent Cortical Tension for PC-3 and PrEC LH cells where the data is shown for the case of not being exposed to shear and the effect of various levels of shear on the PC-3 cells

CHAPTER 4

MODELING SINGLE CELL DYNAMICS

4.1 Introduction

Blood is a suspension of particles. The focus of discussion thus far has been primarily on modeling blood cells from a cellular perspective. However, one of the aims of this research is to develop a general framework for multiple particles potentially composed of a variety of cell types – red/white blood cells, platelets, cancer cells, etc. In order for the behavior of blood to be simulated realistically, these constituents should be such that their presence and behavior influences, and is influenced by, the fluid surrounding them. The current chapter deals with the fluid-structure interaction (FSI) between a blood particle and the surrounding plasma. A brief review on interaction methodologies provides the motivation for the FSI technique chosen. A detailed description of the implementation of the chosen technique is provided and various benchmark for validation, along with some parametric studies are highlighted.

4.2 Review of FSI methodologies

The blood particulates – RBCs, platelets, WBCs, etc. – are together called formed elements of the blood and these occupy roughly 45% of the volume of blood; the rest is plasma. In the micro-scale, the behavior of individual blood particulates play a vital role in the dynamics by influencing, and in turn being influenced by, the surrounding plasma. Thus it becomes essential that the individual particulates (blood cells) be highly resolved and deformable in order to capture the micro-scale dynamics. For the purpose of computational simulations, an RBC can be thought of as a "capsule" which is an elastic membrane enclosing a fluid of either same or different properties as that of the surrounding fluid. This approach has been adopted by myriad researchers in the past [8,16,30,31]. The initial approach in this field was using perturbation methods pioneered by Barther-Biesel and co-workers [8,29,30]. Using a capsule representation, spherical

cells were simulated in Stokes flow using linearized models where the spheres were allowed to deviate only a small amount from their resting shape. Though these were initial attempts, some inferences were drawn about the deformability of capsules in simple shear flow, including possible tank-treading behavior. The viscosity ratio of the fluids interior and exterior to the capsule was not varied. The capsule representation was also utilized by Ramanujan and Pozrikidis using a boundary element method [16] . In their approach, Stokes flow was again simulated, and the viscosities of the interior and exterior fluid was varied. The boundary element method was discussed as being primarily applicable for potential flow problems and was highly mathematically intensive. These methods were primarily adopted for flows with known analytical solutions, and were the first few to foray into the field of FSI for cells and capsules. Secomb et al performed 2-D simulations of blood cells using interconnected viscoelastic elements [104] where both the RBC and the fluid were discretized using finite element (FEM) methods. However, this necessitated a re-meshing of the domain after every time step. Moreover, all the research mentioned so far were for individual particles in known flow conditions, or in single file capillaries.

The actual physiological blood flow environment is a very complex, dynamic and fully 3-D environment that has to be simulated taking the complexity into account. Due to the complex nature of flow, the computational methods have to be adaptive and should be able to resolve high gradients near the particle interfaces and at the walls. Recent advances in computational modeling and in technology have led to the development of methods such as 3-D boundary integral methods, immersed boundary methods and immersed interface methods [23] .

One of the methods that is extensively used for deformable objects embedded in flows is the immersed boundary method (IBM). This method was pioneered by Charles Peskin in the 1970's for investigating blood flow in the heart [12,105]. Because of its versatility, this method has been adopted to numerous other situations of flows with

embedded objects such as heart valves, blood cells, etc. Eggleton and Popel [30] used the IBM to perform 3-D simulations of an RBC as a capsule in simple shear flow. Pozrikidis adopted the IBM to investigate single RBCs in shear flow in 3-D [105]. Eggleton's model incorporated a hyperelastic constitutive model by Skalak [35] for the membrane mechanics, while Pozrikidis used a neo-Hookean model. These works paved the way for future, more resolved studies of deformable cells immersed in fluid. Bagchi in 2007 performed 2-D simulations of upto 2500 deformable RBCs in channels between 20 and 250μm [11]. The fluid interior to the cell was assigned a viscosity that was five times higher than the surrounding fluid. AlMomani et al in 2008 performed 2-D simulations of erythrocyte-platelet interaction in blood flow [14]. While Bagchi's model simulated deformable cells, AlMomani et al used pseudo-rigid representations of RBCs and platelets. This was followed by Bagchi in 2009 who performed 3-D simulations of up to 122 deformable RBCs employing a neo-Hookean membrane model [31]. This work also employed different viscosities in the interior of the fluid, and was implemented using a front-tracking method developed by Unverdi and Tryggvason [106]. The main advantage of the IBM method was that it was designed for handling immersed Lagrangian entities in an underlying Eulerian fluid mesh. Moreover, a body-conforming mesh was not required, and this advantage lends itself beautifully to an application that is proposed in this research. The IBM is well established in the field of simulating FSI of deformable particles and hence it was chosen for FSI.

4.3 The Immersed Boundary Method

4.3.1 Methodology for IBM

The IBM was pioneered by Peskin in 1977 in his work about investigating blood flow in the heart. The basic idea of this method is to have a separate "fluid mesh" and a separate "solid mesh" and the two meshes interact with each other where required using forces. This allows for using any kind of solvers for the fluid and solid separately,

which is one of the highlights of this method. The fluid can interact with the solid by prescribing velocities (and hence deformations) and the solid can interact with the fluid by means of forces. The solid entity is simply "immersed" in the fluid, and the fluid mesh has no knowledge of its existence, save for the forces conveyed to the fluid at specific points at the boundary.

There exists, thus, two separate systems – an Eulerian system for the fluid where the fluid equations are solved, and a Lagrangian system for the solid – where the solid mechanics equations are solved. These two sub-systems are independently calculated and interact only at interfaces. A schematic for this system is shown in Figure 4-1 [26] where Ω_f is the fluid domain and Ω_b denotes the boundary of the 2-D solid. In the fluid domain, the traditional equations, viz. the continuity and the momentum equations hold:

$$\nabla . \vec{u} = \mathbf{0} \tag{4.1}$$

$$\rho\left(\frac{\partial \vec{u}}{\partial t} + \vec{u} \cdot \nabla \vec{u}\right) = -\nabla p + \mu \nabla^2 \vec{u} \tag{4.2}$$

Equation (4.1) and (4.2) shows the basic continuity and momentum equations for the fluid in dimensional form. Here, $\vec{u}$ is the velocity vector, p is pressure, ρ is the fluid density, and μ *is* the fluid dynamic viscosity. For the IBM, the momentum equation is modified to include a source term which incorporates the effects of the stresses in structure. Thus, the modified momentum equation becomes:

$$\rho\left(\frac{\partial \vec{u}}{\partial t} + \vec{u} \cdot \nabla \vec{u}\right) = -\nabla p + \mu \nabla^2 \vec{u} + \boldsymbol{F} \tag{4.3}$$

where $\boldsymbol{F}$ is a source term arising from the force generated in the membrane of the cell. This communicates to the fluid the presence of the force in the solid membrane. This force term is zero where a solid membrane is not present.

4.3.2 The Fluid Solver

Before proceeding to the mechanisms of the IBM and force interactions, it is important to describe the fluid flow solver in general. Briefly, the discretization of the fluid domain can be described as a hybrid collocated cell-centered grid where the velocity vector and the pressure are stored at the cell centers, and a secondary set of mass-conserving velocities are stored at the cell faces. A four-step fractional step method is employed to solve the primitive variable values at the next time step. This is highlighted briefly below, and a more extensive description can be found in [107].

The fractional step method consists of four steps:

First step: This step provides the initial provisional velocity field by solving an unsteady advection-diffusion equation. The incompressibility condition is not explicitly enforced in this step. A second order Adams-Bashforth explicit scheme is used for discretization in time for the non-linear convection term:

$$-\vec{u}.\nabla\vec{u} = \frac{1}{2}(\vec{u}^{n-1}.\nabla\vec{u}^{n-1} - 3\vec{u}^{n}.\nabla\vec{u}^{n}) = \frac{1}{2}\left(H(\vec{u}^{n-1}) - 3H(\vec{u}^{n})\right) \quad (4.4)$$

The diffusion terms are treated implicitly using a Crank-Nicholson scheme. Here, H is a discrete spatial approximation of the non-linear term and L is a spatial approximation to the Laplacian:

$$\frac{1}{Re}(\nabla^2\vec{u}) = \frac{1}{2Re}(\nabla^2\vec{u}^{*} + \nabla^2\vec{u}^{n}) = \frac{1}{2Re}\left(L(\vec{u}^{*}) + L(\vec{u}^{n})\right) \quad (4.5)$$

The resulting equation for this step is ($\vec{\boldsymbol{F}}$ is the membrane force transferred to the fluid from the solid using the IBM which is explained in the next section):

$$\vec{u}^{*} - \vec{u}^{n} = \Delta t\left[\frac{1}{2}\left(H(\vec{u}^{n-1}) - 3H(\vec{u}^{n})\right) + \frac{1}{2Re}\left(L(\vec{u}^{*}) + L(\vec{u}^{n})\right) - G\left(P^{n-\frac{1}{2}}\right)\right] + \vec{\boldsymbol{F}} \quad (4.6)$$

Second step: In the second step, the estimation of the pressure used for calculation of the velocity field ($\vec{u}^{*}$) will be removed in order to obtain the second intermediate velocity field:

$$\vec{u}^{**} = \vec{u}^{*} + \Delta t\, G\left(P^{n-\frac{1}{2}}\right) \tag{4.7}$$

Third step: In the third step, a Poisson equation is solved to obtain the pressure for the next time step. This Poisson equation is derived by initially performing a Helmholtz-Hodge decomposition of ($\vec{u}^{**}$) into its solenoidal and irrotational vector components $\vec{\beta}$ and $\nabla\varphi$:

$$\vec{u}^{**} = \vec{\beta} + \Delta t \nabla\varphi \tag{4.8}$$

The Poisson equation is then obtained by taking the divergence of the above equation (4.8) and mandating that $\vec{u}^{n+1}$ be divergence free:

$$\nabla^2\varphi = \frac{\nabla\cdot\vec{u}^{**}}{\Delta t} \tag{4.9}$$

It is important to note that φ is not pressure, but is instead a purely mathematical variable that can be related to pressure only when the discretization scheme has been chosen. This Poisson equation is solved to obtain the intermediate pressure $p^{n+\frac{1}{2}}$ subject to the following Neumann boundary conditions:

$$\mathrm{L}\left(p^{n+\frac{1}{2}}\right) = \frac{\mathrm{D}(\vec{u}^{**})}{\Delta t} \tag{4.10}$$

$$G\left(p^{n+\frac{1}{2}}\right)\cdot\vec{n}|_{\partial\Omega} = 0 \tag{4.11}$$

Fourth step: In the fourth and final step, the provisional velocity obtained in the second step is projected onto the divergence free space where the final velocity ($\vec{u}^{n+1}$) is obtained:

$$\vec{u}^{n+1} = \vec{u}^{**} - \Delta t \mathrm{G}(p^{n+\frac{1}{2}}) \tag{4.12}$$

4.3.3 Interfacing with solid entity (NM-I and NM-V)

Recall from Chapter 2 the steps involved in performing a complete fluid-solid interaction calculation in the current framework. Computing a single time step broadly entails the following sub-steps:

For Time Step $\mathbf{t}^n$:

NM-I. Determine Boundary Conditions to be applied to the NURBS entity

NM-II. Apply the Boundary Conditions obtained in NM-I to the NURBS entity

NM-III. Characterize deformation of NURBS entity

NM-IV. Determine entity-specific Membrane restoring forces

NM-V. Communicate the presence of membrane forces to surrounding fluid

Repeat for Time Step $\mathbf{t}^{n+1}$.

While Chapter 2 dealt with Steps NM-II to NM-IV, Steps NM-I and NM-V will be described in detail in this chapter. The IBM procedure is described in Figure 4-2. In Step NM-I, the boundary conditions to be applied to the solid are specified, i.e. the velocities are transferred from the fluid to the solid to enforce kinematic compatibility at the interface. This ensures that the velocity at an "interface" point (i.e. shared point between the solid and the fluid) is the same irrespective of the domain (Lagrangian or Eulerian), essentially enforcing the no-slip condition. Mathematically, this is shown as:

$$\frac{d\boldsymbol{x_f}}{dt} = \mathbf{u}(\boldsymbol{x_s}) \tag{4.13}$$

where $\boldsymbol{x_f}$ denotes any point in the Eulerian (flow) domain and $\boldsymbol{x_s}$ denotes any point on the Lagrangian (solid) domain. At a given timestep, the velocity at a solid interface point can be interpolated from the velocities of the adjacent fluid points using a delta function.

$$\boldsymbol{u}(\boldsymbol{x}_s) = \int_{\Omega_S} \boldsymbol{u}(\boldsymbol{x}_f)\delta(\boldsymbol{x}_f - \boldsymbol{x}_s)d\boldsymbol{x}_f \tag{4.14}$$

where $\boldsymbol{u}(\boldsymbol{x}_s)$ denotes the velocity of the solid membrane and $\boldsymbol{u}(\boldsymbol{x}_f)$ denotes the velocity of the surrounding fluid. The delta function δ used in (4.14) is adopted from [106] and is a product of three one-dimensional delta functions $\delta(\boldsymbol{x}_f - \boldsymbol{x}_s) = \delta(x_f - x_s)\,\delta(y_f - y_s)\,\delta(z_f - z_s)$ and is defined in (4.15):

$$\delta(\boldsymbol{x}_f - \boldsymbol{x}_s) = \begin{cases} (4h)^{-\alpha}\prod_{i=1}^{\alpha}\left(1 + cos\,\frac{\pi}{2h}(\boldsymbol{x}_{f_i} - \boldsymbol{x}_{s_i})\right), & |\boldsymbol{x}_{f_i} - \boldsymbol{x}_{s_i}| < 2h \\ 0, & otherwise \end{cases} \tag{4.15}$$

where h is the Eulerian grid size for the fluid domain and α denotes the dimension of the problem considered, which is 3 for the purpose of this work. This provides the contribution of all the fluid nodes lying within a sphere of influence of radius $2h$ around the point of interest while all other points lying outside the sphere of influence have null or zero contributions. This is highlighted schematically in Figure 4-3 for a simple 2-D case, where the circle of influence (blue dots) denotes all the fluid points that will contribute to the value of the parameter (eg. velocity) at the solid node (red dot) in the center. All the other fluid nodes (outside the black dotted circle) do not contribute towards the value of a parameter at the central solid node. This idea is directly extended to 3-D where all the fluid nodes lying inside the sphere of influence will contribute to a non-zero delta function value, hence contributing to the value of a parameter at a solid node. The delta function is zero everywhere, except where a solid membrane is present, thereby ensuring that only the fluid in the immediate vicinity of the solid experiences a contribution via the source term.

Once the velocities are interpolated at the solid points, the NURBS isogeometric analysis procedure described in Chapter 2 is performed and the membrane forces are calculated. Step NM-V of the FSI procedure involves spreading the membrane forces from the solid to the surrounding fluid points, a task that is carried out by using the same delta function described above. The force given to the fluid is included a source term in

the momentum equation (4.2) thereby achieving closure. The elastic forces in the cell membrane are coupled to the fluid via the source term $\boldsymbol{F}$ and the delta function:

$$\boldsymbol{F}(\boldsymbol{x}_f) = \int_{\Omega_f} \boldsymbol{f}(\boldsymbol{x}_s)\delta(\boldsymbol{x}_f - \boldsymbol{x}_s)d\boldsymbol{x}_s \tag{4.16}$$

where $\boldsymbol{f}(\boldsymbol{x}_s)$ is the elastic force generated in the solid membrane. This completes the FSI problem. A flowchart showing the information flow for FSI is shown in Figure 4-4.

In order to specify different properties for the interior and exterior of the membrane, a front tracking algorithm is used for the membrane. Briefly, the delta function described in (4.15) is used to determine the fluid points in the vicinity of a membrane point $\boldsymbol{x}_s$. Once all the surrounding fluid points are determined, the unit normal $\vec{\boldsymbol{n}}$ is used to identify the points in the interior of the membrane. The entire interior of the particulate is then identified using a fast-marching algorithm [108]. An indicator function $\boldsymbol{I}(\boldsymbol{x},\boldsymbol{t})$ is used to specify the viscosity in the interior of the RBC, described in (4.17).

$$\boldsymbol{\mu}(\boldsymbol{x},\boldsymbol{t}) = \boldsymbol{\mu_p} + (\boldsymbol{\mu_c} - \boldsymbol{\mu_p})\boldsymbol{I}(\boldsymbol{x},\boldsymbol{t}) \tag{4.17}$$

where $\boldsymbol{\mu_p}$ is the viscosity of plasma which is specified as 1.2 cP and $\boldsymbol{\mu_c}$ is the viscosity of the cytoplasm of the RBC, which is specified as 6 cP, thereby providing a viscosity ratio $\lambda = \boldsymbol{\mu_c}/\boldsymbol{\mu_p} = 5$, as reported to be physiological values in viscosity [68]. The viscosity ratio for spherical particulates is maintained at unity for simplicity.

4.4 Single Blood Particulate Micro-scale Dynamics using IBM

4.4.1 Validation: Sphere in Linear Shear Flow

As a first test case, the motion of a sphere in a linear shear flow was simulated. This is a well-documented case for finite element models [16,109,110]. Briefly, the sphere is placed at the center of a domain with a fully developed shear flow. The shear flow profile is $\boldsymbol{u} = (kz, 0, 0)$ with k being the non-dimensional shear rate and z is the vertical distance from the center of the domain. The length scale chosen is the radius of

the sphere $L_0 = R$, the time scale is $t_0 = 1/\dot{\gamma}$ where $\dot{\gamma}$ is the shear rate, the velocity scale is $U_0 = R\dot{\gamma}$ and the Capillary number is $Ca = U_0\mu/E_s$ where μ is the fluid viscosity and E_s is the membrane shear modulus. The constitutive model used for this simulation was the extensively used neo-Hookean model, details of which can be found in [11,79]. The value of E_s is chosen to be $6\,x\,10^{-3}\,dyn/cm$ concurrent with published values [110]. The viscosity of the fluid is chosen to be that of plasma – 1.2 cP and the density of the fluid is taken to be $\rho_0 = 1060\,kg/m^3$. Various Capillary numbers were simulated and the measure of deformation of the spherical cell was captured by the Taylor Deformation Parameter $D = (L - B)/(L + B)$ where L is the length and B is the width of the capsule in the plane of shear. For the sake of simplicity, the inner and outer fluid have the same fluid properties and bending was neglected. A schematic of the flow field to which the sphere is subjected to is shown in Figure 4-5. Figure 4-7 shows the late-stage deformed shapes of the sphere for various Capillary numbers. This matches published results [16,30,110]. A mesh density analysis was performed for a high Capillary number of 0.1, with meshes ranging from 176 elements to 9472 elements. The evolution of the Taylor Deformation parameter for Ca = 0.1 for various meshes is shown in Figure 4-8. The error in the coarsest model with 176 elements was ~5%, with the error reducing to < 1% for models with higher number of elements. All the models including the coarsest one captured the asymptotic nature of the deformation very well. The evolution of the deformation parameter for various Ca is shown in Figure 4-9, compared with the evolution of the deformation parameter from [110]. It can be clearly seen that the NURBS isogeometric Analysis captures the asymptotic evolution of the Deformation Parameter very accurately for the range of Capillary numbers from 0.025 to 0.2. The NURBS mesh used for the sphere consisted of 2432 elements. This strongly shows the advantage of using isogeometric Analysis over conventional FEM based methods, in that highly coarse meshes can be used while still preserving accuracy and geometric fidelity. While a much coarser solid mesh could have been employed for the NURBS analysis, the

limitation of this method is the use of the IBM for FSI, which requires a specific solid mesh density based on the fluid mesh. That the NURBS based isogeometric analysis allows the use of extremely coarse meshes while still providing accuracy in results is well documented in the paper by Hughes et al [39].

4.4.2 Validation: Sphere in Parabolic Flow

In order to simulate the motion of blood particulates in the micro-circulation, the behavior of cells under capillary (parabolic) flow were simulated next. For validation purposes, the behavior of a sphere in a fully developed Poiseuille flow profile was studied. This is based on a previous simulation performed by others [31,111] in order to test the extent of deformation of the spherical cell based on the flow profile. In an unhindered flow, the sphere deforms and attains a steady state shape based on the Ca as long as the length of the capillary or channel is enough to attain steady state. An increase in Ca leads to an increase in the deformation of the particle, and is also dependent on the material properties of the membrane. In addition, the size ratio between the capsule diameter and the capillary or channel width bears an influence on the way the particle deforms and if it reaches steady state. A schematic of this case is shown in Figure 4-6.

In order to compare with the simulations of [111,112], the ratio of the capillary width to cell diameter H/d was maintained at 1.3 and the Ca = 0.04. A mesh independency study was also carried out for this case, with the coarsest mesh having 176 NURBS elements, the medium mesh having 640 NURBS elements and the fine mesh having 2432 NURBS elements. A comparison of the steady state shapes for all three meshes is shown in Figure 4-10 along with the steady state shape reported in [112] for the same case parameters. While the membrane model in [112] was reported to be neo-Hookean, no moduli parameters were provided and hence the current NURBS model used typical parameters used for RBC membranes, i.e. $6\,x\,10^{-3}\,dyn/cm$ and bending was neglected. It can be seen that the three NURBS meshes almost overlap each other

and the curvatures at the front and rear of the spheres match the final shape of [112] very well.

4.4.3 Validation: RBC in Parabolic Flow

The deformation of an RBC in Poiseuille flow in a capillary was simulated next. The case of an RBC in a capillary and/or channel is interesting because of the various phenomenon noticed in capillary flow such as Fahraeus-Lindqvist effect, cell free zone [9,113], reduction in apparent viscosity, reduction in hematocrit [2] and others. Moreover, the motion of RBCs through capillaries become even more interesting because the RBCs can fold and bend dramatically to squeeze through capillaries half its diameter [17,114]. The ability of the RBC to undergo such drastic deformations is in part due to the unique nature of the membrane which allows it to deform but strongly resists area dilatation [35,68,75].

For validation purposes, the flow of an RBC with 440 NURBS elements in a capillary at Ca=0.1 was considered. Beginning from an unstressed, biconcave shape, the RBC deforms and achieves a parachute shape. Moreover, the portion of the RBC facing the flow bends into a convex shape while the rear of the RBC away from the direction of flow deforms into a concave shape. The RBC reaches a steady state and is then convected without undergoing any additional deformation. Figure 4-11 shows the comparison of the steady state shape obtained by the NURBS model and the shape reported in [115] for the same conditions. It can be seen that the NURBS model matches the reported shape very closely. Despite the coarse representation, the model is able to capture accurately the different curvatures at the front and rear of the RBC. The steady state shape obtained by a finer NURBS model with 1680 elements (not shown) overlapped the steady state shape obtained by the coarser mesh with 440 elements. Thus both the coarse and fine NURBS meshes capture the curvatures of the biconcave RBC in parabolic flow very well.

4.4.4 Parametric Study: Sphere in Shear Flow

The effect of different membrane laws on the behavior of a sphere deforming in shear flow were simulated for a fixed Ca of 0.1 .Using the deformation behavior of a model with a neo-Hookean membrane as a reference, the behavior of the same spherical model under the action of the well-known Skalak law [35] with different membrane properties was simulated. The Skalak Law is replicated here for convenience.

$$W = \frac{E_b}{4}\left(\frac{1}{2}{I_1}^2 + I_1 - I_2\right) + \frac{E_c}{8}{I_2}^2 \tag{4.18}$$

$$C = \frac{E_c}{E_B} = \frac{Area\ Dilatation\ Stress\ Value}{Neo{-}Hookean\ Membrane\ Stress\ Value} \tag{4.19}$$

where W is the strain energy density function, $\lambda_1\ and\ \lambda_2$ are principal stretches, $I_1$and I_2 are the principal invariants based on [22]. The factors E_b and E_c are membrane material properties. For the Skalak Law, the value of E_b was maintained at $6\ x\ 10^{-3}\ dyn/cm$ and the area modulus E_c was varied over a range of values such that the ratio C defined above ranged from C = 1 to 1000. All other parameters namely the NURBS mesh and the fluid mesh were kept constant. The time step had to be reduced for the higher area moduli in order to achieve steady-state like behavior. The behavior of the sphere under the aforementioned membrane laws is shown in Figure 4-12. As can be seen, there is a substantial difference in the evolution of the deformation parameter as the membrane law is changed. Specifically, the sphere undergoes less deformation as the membrane becomes stiffer, as was expected. It is interesting to note that the late-stage deformation of the sphere for stiffer membranes is similar to a sphere with a neo-Hookean membrane at lower capillary numbers. Due to the high computational cost involved with an extremely small time step at the higher values of C, the simulation was not carried out for longer times. The behavior of stiffer membranes indicates that as the membrane becomes stiffer, it not only reaches steady-state faster, but also undergoes substantially lesser deformation than a more compliant membrane. This has significance in modeling spherical cells of varying membrane properties namely leukocytes and cancer cells.

4.4.5 Parametric Study: Sphere in Parabolic Flow

The motion of a sphere in parabolic flow in the same capillary used for RBC case was simulated. This was done to ensure that we can capture the deformation of the spherical cell in parabolic flow, as it is envisioned to simulate multiple cells – both biconcave and spherical in a dynamic setting. The size ratio and the parabolic flow velocity was maintained the same as that used for the RBC case. The Ca used in this case is also 0.6, and the constitutive model used in the neo-Hookean model. For the sake of simplicity, the inside and outside fluid have the same fluid properties and bending was neglected. The evolution of the spherical shape is shown in Figure 4-14. As reported in [31], the front and rear portions of the sphere respectively become more convex and concave with the development of almost sharp edges at the transition between the curvatures. The maximum deformation occurs in the $x - y$ plane while the shape in the $y - z$ remains largely unchanged from a circle. The spherical model used in this simulation had 640 elements.

The motion of a sphere in a 3-D parabolic flow in a capillary was simulated next. By 3-D, the parabolic flow profile depended on the position of the y and z-position of the cell unlike the previous cases where the parabolic flow profile depended only on the y position. Thus the parabolic flow profile is that of a paraboloid or a conical profile. The evolution of the spherical shape is shown in Figure 4-14. It can be clearly seen that starting from a sphere, the cell deforms into a "bullet" like shape, going on to deform into a paraboloid shape due to the flow around it. This is in qualitative agreement of the shapes obtained experimentally by Risso. et.al. in [116], a snapshot of which is shown in Figure 4-14(a). There is very good qualitative agreement of the deformed shapes of the sphere when subjected to the paraboloid flow. The spherical model used in this simulation also has 640 elements.

As a next logical step the effect of different membrane laws for a sphere in Poiseuille flow with the capillary number Ca = 0.125 was investigated. The ratio of the

capillary width to cell diameter H/d was maintained at 1.6. Three different membrane models were utilized – neo-Hookean, Skalak model with C =1 and a Skalak model with C = 10 (refer above for description of C). Snapshots of the shapes at end-stage are shown in. Figure 4-13 where it can be seen that the model with the neo-Hookean membrane undergoes the most deformation, with the Skalak models deforming to a lesser extent. It is also interesting to note that while the neo-Hookean and Skalak C=1 models display a convex surface in the rear portion of the sphere, the model with the Skalak C=10 membrane displays a concave surface. This indicates that the membrane model significantly impacts the extent of deformation of a particulate in capillary flow in the micro-circulation.

4.4.6 Parametric Study: Biconcave RBC in Parabolic Flow

The motion of a biconcave RBC in a fully developed planar Poiseuille flow (parabolic flow) in a capillary was simulated next. This is also a well-documented test case by researchers in the past [31,104,117]. The ratio of the capillary width to cell diameter H/d was maintained at 1.6, with the length scale being the same as the previous test case – the radius of the cell. This size ratio between the tube and the cell was chosen to mimic the reality of the flow of a cell through a capillary of comparable size to the cell, which entails the cell to deform substantially. The velocity scale here was the centerline velocity of the flow of fluid in the capillary, $U_0 = U_{center}$. The Reynolds number is defined as $Re = \rho_0 U_0 R/\mu$ and the Capillary number is defined as $Ca = U_0 \mu / E_s$. The Ca tested was 0.6, which meant that the cell had to undergo a large deformation in the tube. For the sake of simplicity, the inside and outside fluid have the same fluid properties and bending was neglected. The results of the simulation are shown in Figure 4-15(a). The initially biconcave RBC slowly deforms into a parachute shape on account of the parabolic flow profile. The shape of the cell in the $y-z$ plane remains

largely unchanged from the initial shape – a circle. These results are in agreement with both simulations and experiments [31][116]. The RBC model used in this simulation had 440 elements.

The effect of membrane laws on the behavior of an RBC in 3-D Poiseuille flow (paraboloid velocity profile) in a capillary was investigated. The capillary number was 0.1 and two membrane models were used – a neo-Hookean model and a Skalak C=1 model. The evolution of the RBC shape as it is subjected to a fully developed Poiseuille flow is shown in Figure 4-16. The neo-Hookean model undergoes considerable deformation due to the compliant nature of the membrane model, while the Skalak model undergoes considerably lesser deformation. This has implications in studying sickle cell anameia and/or malaria where the deformability of the cell becomes affected thereby preventing the RBC from traversing the microcirculation with efficacy of a normal RBC [118–120]. Figure 4-17 shows smooth renderings of the stages of deformation of an RBC in a capillary, showcasing the ability of NURBS to achieve smooth, potentially physiologically realistic deformations with very few elements.

4.4.7 Parametric Study: Biconcave RBC in Linear Shear Flow

Lastly, the motion of biconcave RBCs in shear flow was investigated. The dynamics of RBCs in shear flow is quite interesting, as RBCs are known to undergo tumbling motion at specific shear rates. Moreover, the tumbling dynamics are different for different shear rates. In this study, the effect of shear rates and different membrane laws on the tumbling dynamics of RBCs in shear flow was investigated. Shear rates of Ca = 0.0125, 0.025, 0.05 and 0.1 were simulated. The viscosity ratio of the RBCs was kept at the physiological value of 5. The viscosity of the fluid inside the RBC was updated at each timestep using the front tracking method described earlier. The membrane models

were the same as that used for testing the behavior of a sphere under different membrane laws in Poiseuille flow - neo-Hookean, Skalak model with C =1 and a Skalak model with C = 10. For quantifying the tumbling dynamics, a deformation parameter $Dxy = (L - B)/(L + B)$ where L is the length and B is the width of the midplane of the RBC in the plane of shear was used, as defined in [109,110]. The RBC is oriented at an angle of π/4 at time t*=0. All the simulations for RBC in shear flow were carried out with 440 NURBS elements.

For the purpose of comparison the case of the RBC described with the Skalak C=1 model for the lowest Ca = 0.0125 and the highest Ca = 0.1 is considered. Figure 4-18 shows the sequence of deformation of the RBC under Ca = 0.0125. The RBC undergoes an almost rigid-body like tumbling at this Ca. Fig Figure 4-20 and Figure 4-21 shows the deformation parameter Dxy versus -θ/π for this case. Because the RBC has a biconcave shape to begin with, the deformation parameter does not start at 0 unlike that for a sphere. The amount of deviation of Dxy from the initial value represents the extent of deformation of the RBC from its stress-free biconcave shape. The purpose of plotting Dxy versus -θ/π is to investigate the extent of deformation with respect to the orientation of the RBC at any point. It can be seen that the qualitatively observed almost rigid-body like rotations in Figure 4-18 translates quantitatively to an almost constant Dxy over the entire duration of one rotation. In contrast, Figure 4-19 shows the sequence of deformation and rotation of the RBC with the same membrane model but at Ca = 0.1. It is evident that the RBC undergoes considerably much more deformation at this high capillary number. As the RBC begins to tumble, it also gets stretched in the direction of shear until it reaches a sleeping position. Beyond this point the RBC actually undergoes compression as it tumbles further, which can be seen in Figure 4-19. This stretching and compression of the RBC translates into a large deviation from rest state of Dxy, which is plotted in Figure 4-20. While the Dxy for Ca= 0.0125 remained largely constant at around 0.78, the Dxy for Ca=0.1 deviates to 0.5 and begins to return to its original value.

This shows that the RBC responds to the stretching of itself by pulling back in an attempt to return to its stress-free state. Also shown in Figure 4-20 is the Dxy for Ca=0.05 for the Skalak C=1 and Skalak C=10 membranes along with the Dxy obtained by Pozrikidis [21]. The Skalak C=10 membrane closely follows the modified neo-Hookean membrane employed in [21]. It is also clear that not only does capillary number impact the tumbling dynamics, but membrane models play an important role in it as well.

After validating the tumbling dynamics of an RBC in shear flow, the effect of membrane laws on the tumbling dynamics were briefly investigated. All simulations were performed with only 440 NURBS elements. Three membrane models were simulated – neo-Hookean, Skalak C=1 and Skalak C=10 membranes at Ca=0.0125, 0.025, 0.05 and 0.1. For the lowest capillary number Ca=0.0125, only the Neo-Hookean and Skalak C=1 membranes were simulated as simulating the Skalak C=10 membrane required an extremely small timestep which was extremely computationally intensive. However, the tumbling dynamics at Ca=0.0125 did not differ much between the neo-Hookean and Skalak C=1 models as the RBC underwent almost rigid-body like rotations without much deviation in shape. The deformation parameter Dxy was calculated for all cases in order to quantitatively compare between them. Figure 4-21(a) shows the deformation parameter for Ca = 0.025 for all three membrane models. It can be seen that while there is not much deviation between them due to the tumbling being close to rigid-body like rotation, the Skalak C=1 model deviates slightly more than the other models. The difference between the three models becomes even more pronounced at Ca = 0.05 where the Skalak C=1 model deviated much further than the Neo-Hookean model, as shown in Figure 4-21(b). Interestingly, the neo-Hookean model reaches a minima early on during the rotation while the Skalak C=1 model reaches its minima later after almost completing an entire rotation before the RBC tries to actively regain its stress-free state. Also, while the neo-Hookean model is able to revert back very closely to its stress-free state, the Skalak C=1 model is not able to do so. The Skalak C=10 model prevents the RBC from deforming as

much as the other two models, which results in it maintaining its shape as close to the rest shape as possible over the duration of an entire rotation. The difference in tumbling dynamics between the membrane models is the most pronounced for the highest capillary number of 0.1. Figure 4-19 and Figure 4-22 shows the sequence of deformation of an RBC with a neo-Hookean model for Ca=0.1. It can be clearly seen that the RBC undergoes considerable deformation as the flow stretches it out to a large extent. The RBC is unable to prevent the large deformation due to the high capillary number as well as the membrane law. In contrast, the Skalak C=1 membrane prevents the RBC from deforming significantly, and is able to retain a more coherent shape closer to the biconcave shape. The plot Dxy versus orientation for Ca=0.1 is shown in Figure 4-21(c). It can be clearly seen that while the Skalak C=1 model deviates considerably from the rest shape while the Skalak C=10 membrane is able to prevent a large deviation throughout the tumbling process. Also shown in Figure 4-21 is the Dxy obtained in [21] for a modified neo-Hookean model with different elastic moduli. Thus the presence of a stiffer membrane has a considerable impact on the dynamics of an RBC in shear flow, with the stiffer membrane resisting deformation compared to a more compliant membrane.

4.5 Discussion and Summary

Simulating micro-scale blood flow dynamics entails two-way communication between the solid and the fluid, necessitating the implementation of a FSI algorithm. Due to the use of an underlying Cartesian mesh for simulating the fluid flow in an Eulerian setting, the Immersed Boundary Method was chosen for FSI. In the IBM, the solid entities are treated as Lagrangian entities immersed in an underlying Eulerian grid, making the method perfectly suited for the current research.

The IBM was successfully implemented and incorporated into the existing Cartesian grid solver ELAFINT. Details on the IBM implementation were provided and

explained. The IBM was tested in conjuction with the NURBS-based isogoemetric analysis approach described in Chapter 2 in order to perform FSI simulations. The implementation of the IBM was tested in multiple cases simulating the motion of a sphere in shear flow, the motion of a sphere in Poiseuille flow, the motion of RBCs in Poiseuille flow and the motion of RBCs in shear flow and were validated against published literature [21,31,110,112,115]. In addition to the aforementioned basic validation cases, the IBM implementation was further utilized in investigating the effect of membrane models on the flow dynamics of various cells.

The use of NURBS based analysis presents a very promising potential in FSI based applications such as those described in this chapter. The NURBS FSI procedure was validated by simulating various test cases such as shear flows and parabolic flows for both spherical and biconcave RBC models. Despite using substantially coarse meshes, not only was the geometry of the models replicated during flow, the dynamics of the system was also captured accurately and efficiently. Parametric studies were performed for multiple test cases of spherical and biconcave cells in shear and parabolic flows. The membrane properties were varied in order to investigate the effect of stiffer membranes on flow dynamics. In all the cases that were simulated, using stiffer membranes resulted in reduced deformation of the NURBS entities. Successfully capturing the different behavior of the blood particulates for different membrane laws displays the efficacy and utility of the NURBS modeling approach.

While the use of the IBM limited the mesh density of the NURBS models (the extremely coarse models could not be simulated due to restrictions on the grid sizing on the fluid side), other FSI methods can be employed in the future which exploits the coarse representation of the NURBS models to the fullest. Also, the current models contained a convergent *pole* both in case of the RBC and the spherical model. This was done in order to have a single NURBS Patch, or sheet, describe the complete cell and its deformation. The presence of a pole is known to have adverse effects especially in interacting with the

surrounding fluid [37,121]. In the future, models can be created with multiple NURBS patches such that a pole can be avoided. Other isogeometric modeling techniques such as T-Splines can also be utilized, if necessary[40]. As mentioned before, the global least squares based technique for effecting deformation may not preserve the surface normals very accurately and localized schemes can be implemented [59,122].

To summarize, the IBM was described and implemented in order to achieve FSI between the solid (blood cell) and the surrounding fluid. The NURBS based isogeometric analysis in conjunction with the FSI through IBM was successfully implemented in a three dimensional setting and was validated against canonical simulations. The advantage of NURBS in using very coarse representations of the entities (blood cells and particulates) was presented and employed in a series of test cases to validate the efficacy of this approach.

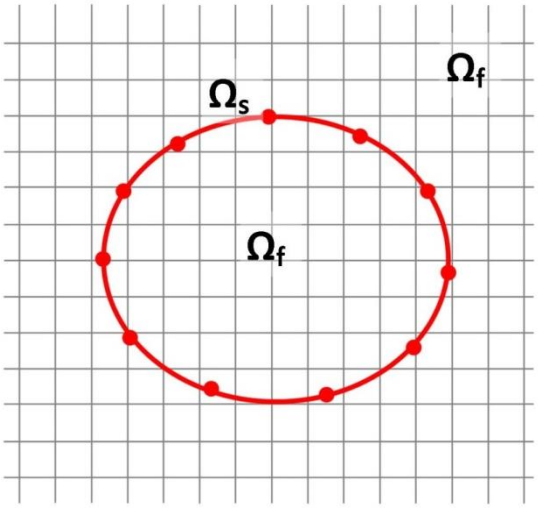

Figure 4-1: 2-D schematic of the two domains that exist in the IBM framework: Ωf is the fluid domain and Ωs denotes the boundary of the immersed 2-D zero-thickness membrane.

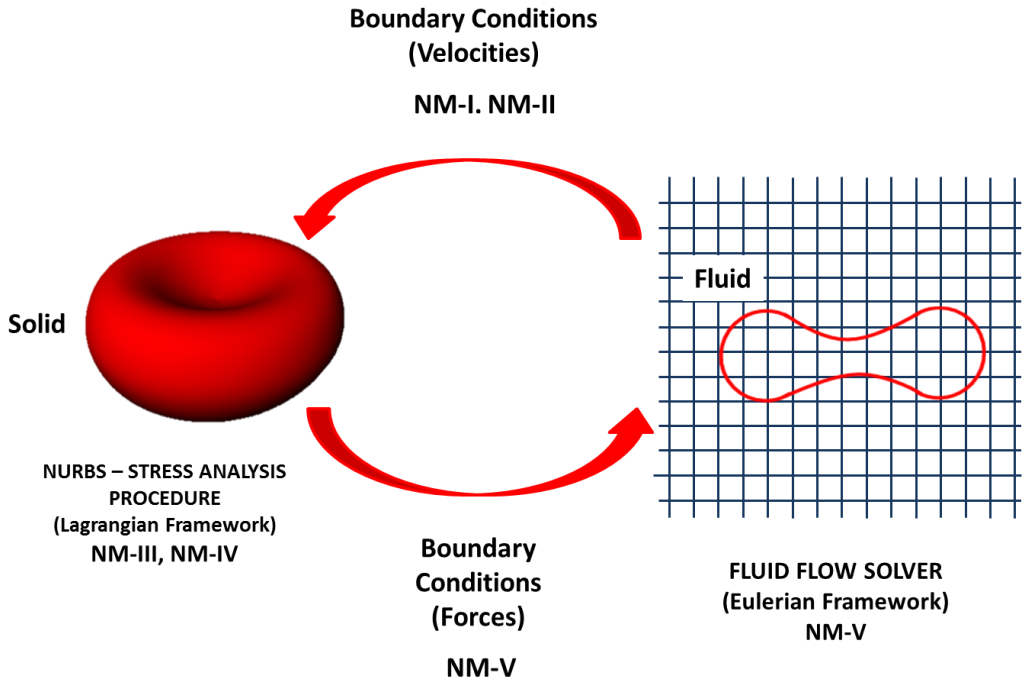

Figure 4-2: Schematic of steps involved in IBM to communicate between the solid and the fluid. Information about the boundary conditions from the fluid (velocities) is provided to the sold via a delta function, and the same delta function is used to transmit information about the membrane forces back from the solid to the fluid. The forces are incorporated as a source term in the momentum equation for the fluid and the system is solved.

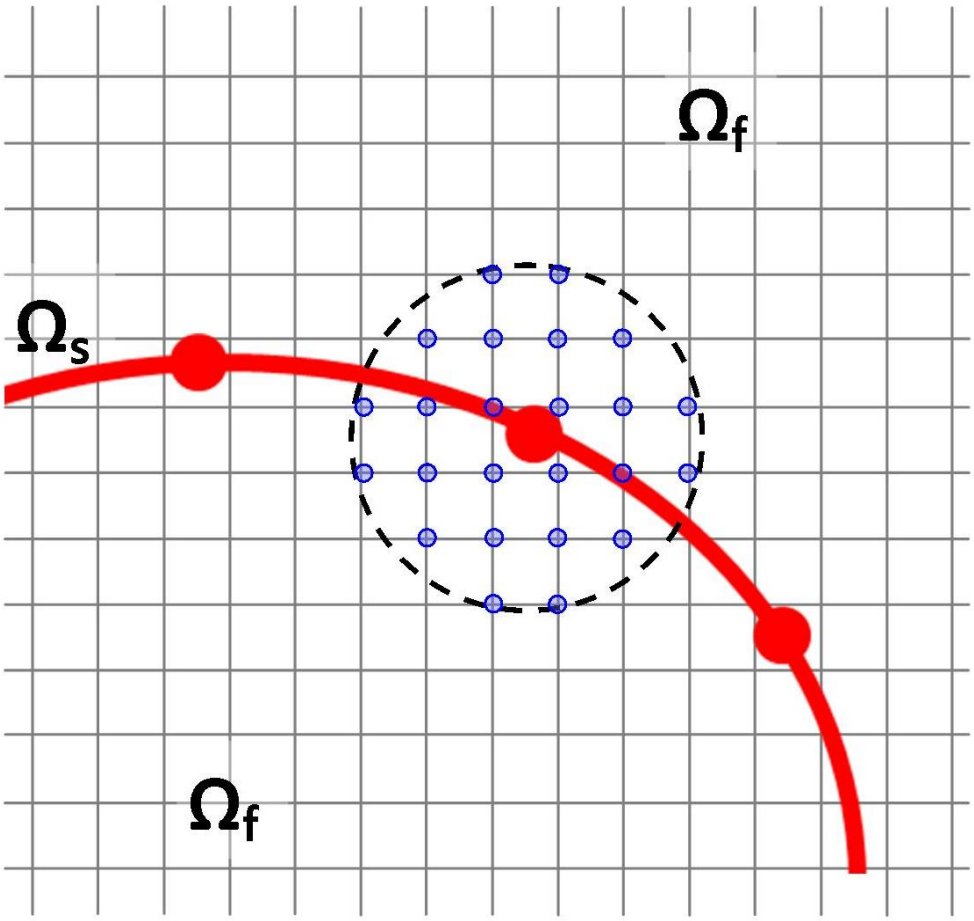

Figure 4-3: 2-D schematic of contributing fluid nodes for the delta function used to interpolate values of boundary conditions to be applied between solid and fluid. Only the fluid points within the sphere of influence will contribute to the delta function; all other points will not have any contribution.

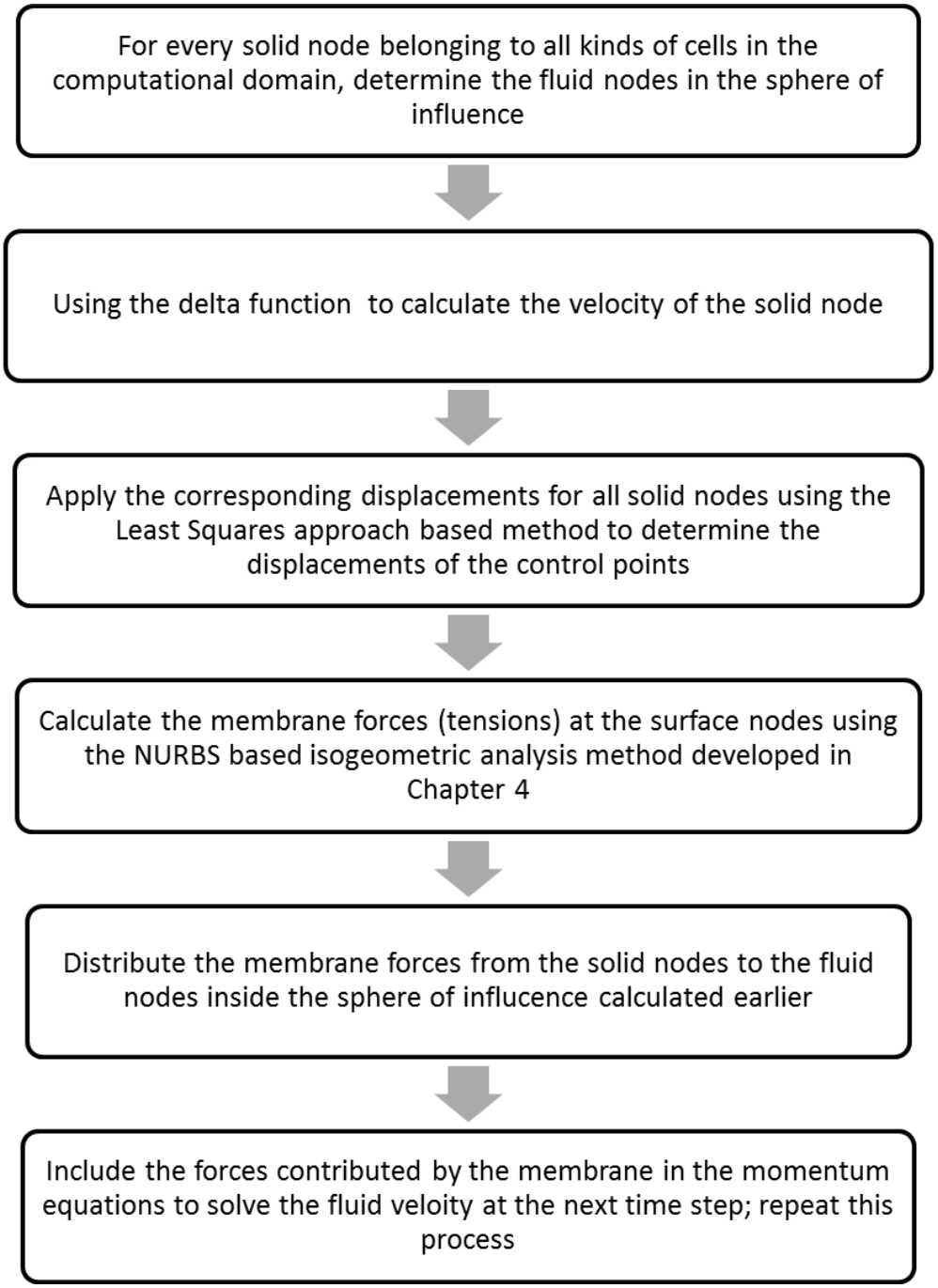

Figure 4-4: Flowchart showing the procedure to perform FSI using IBM.

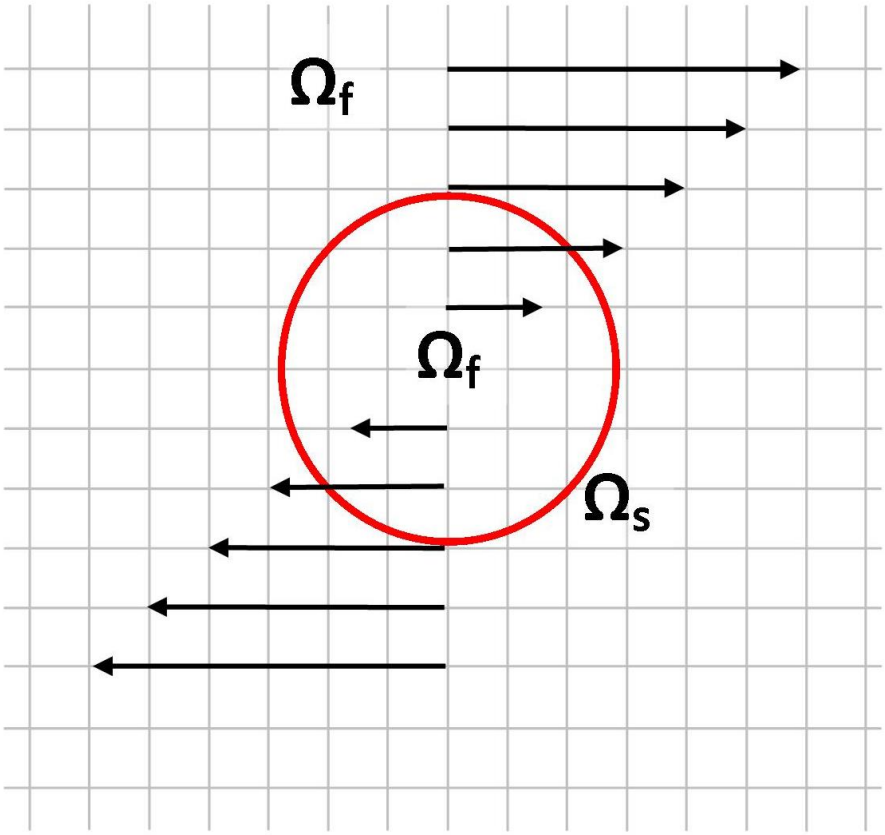

Figure 4-5: Schematic of problem setup for analyzing the deformation of a sphere in linear shear flow described in section 4.4.1 with the Eulerian (Ωf) and Lagrangian (Ωs) domain shown.

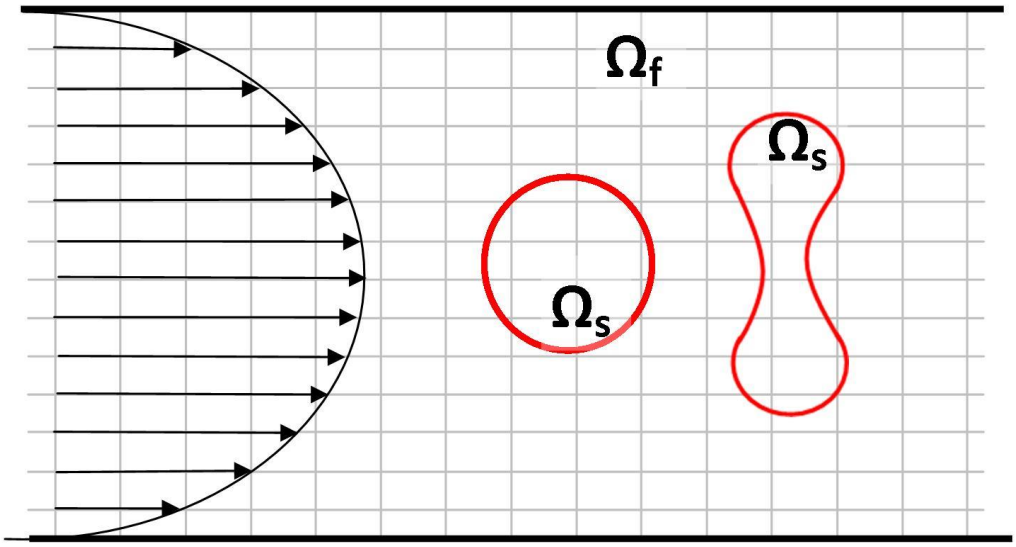

Figure 4-6: Schematic of problem setup for analyzing the deformation of a biconcave RBC and a spherical cell in parabolic flow described in section 4.4.2 and 4.4.3 with the Eulerian (Ωf)and Lagrangian (Ωs) domain shown.

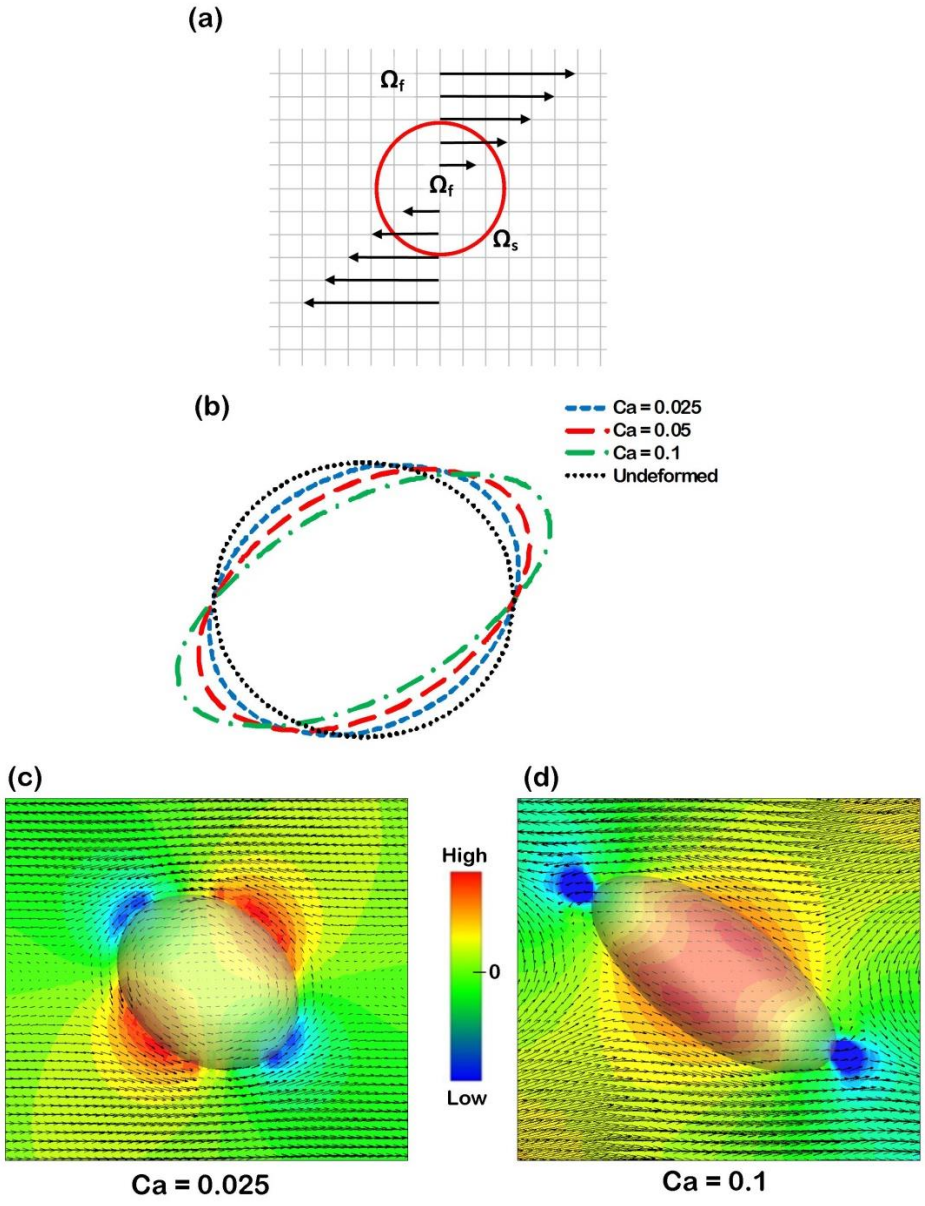

Figure 4-7: Behavior of a sphere in linear shear flow (a) Schematic of shear flow setup for validation. The sphere is introduced at the center of the domain. (b) Late-stage deformed profiles of spheres for various capillary numbers. The initial undeformed shape is also shown (c) Flowfield around sphere at Ca = 0.025 and Ca = 0.1 (d) Velocity vectors in (c) and (d) clearly show the presence of circulatory flow.

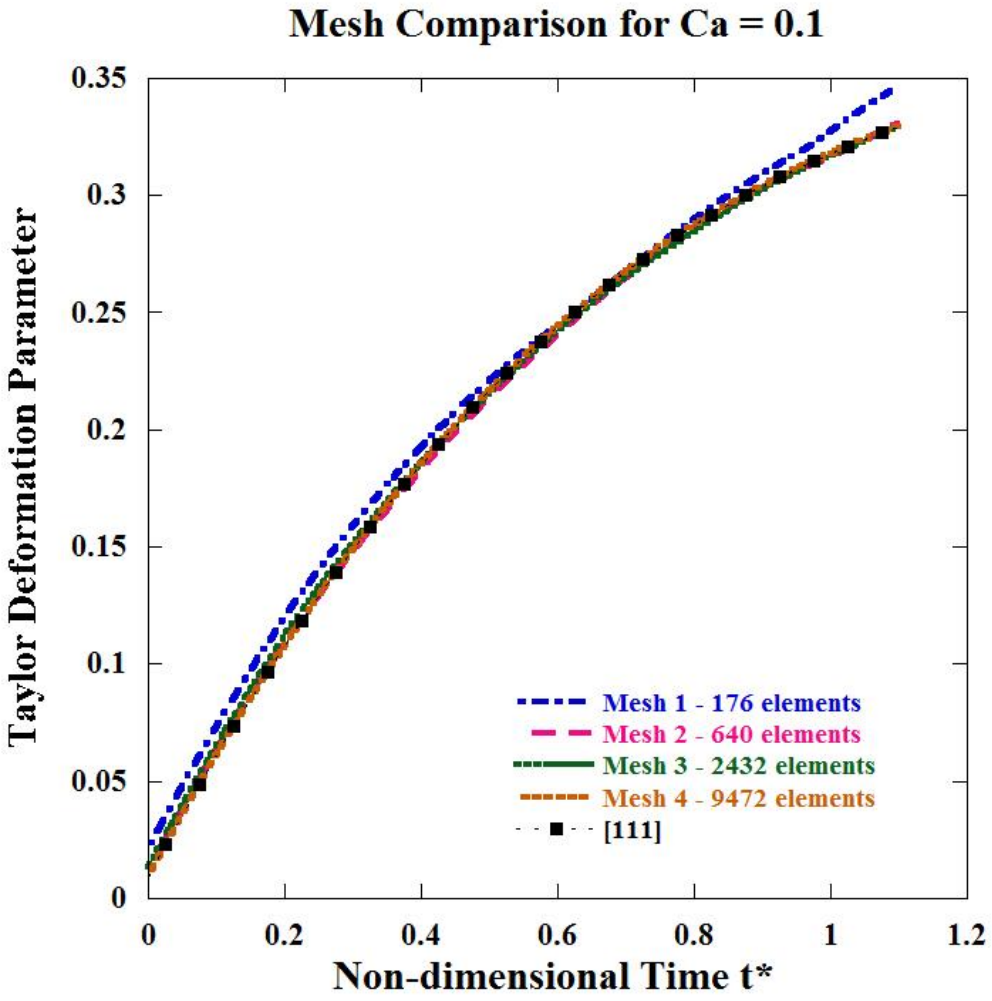

Figure 4-8: Mesh Density study for various NURBS meshes for the deformation of a sphere for a high Capillary number of 0.1. There is approximately a 5% error in the coarsest model with 176 elements. The error in all the other meshes compared to [110] is less than or equal to 1.5%.

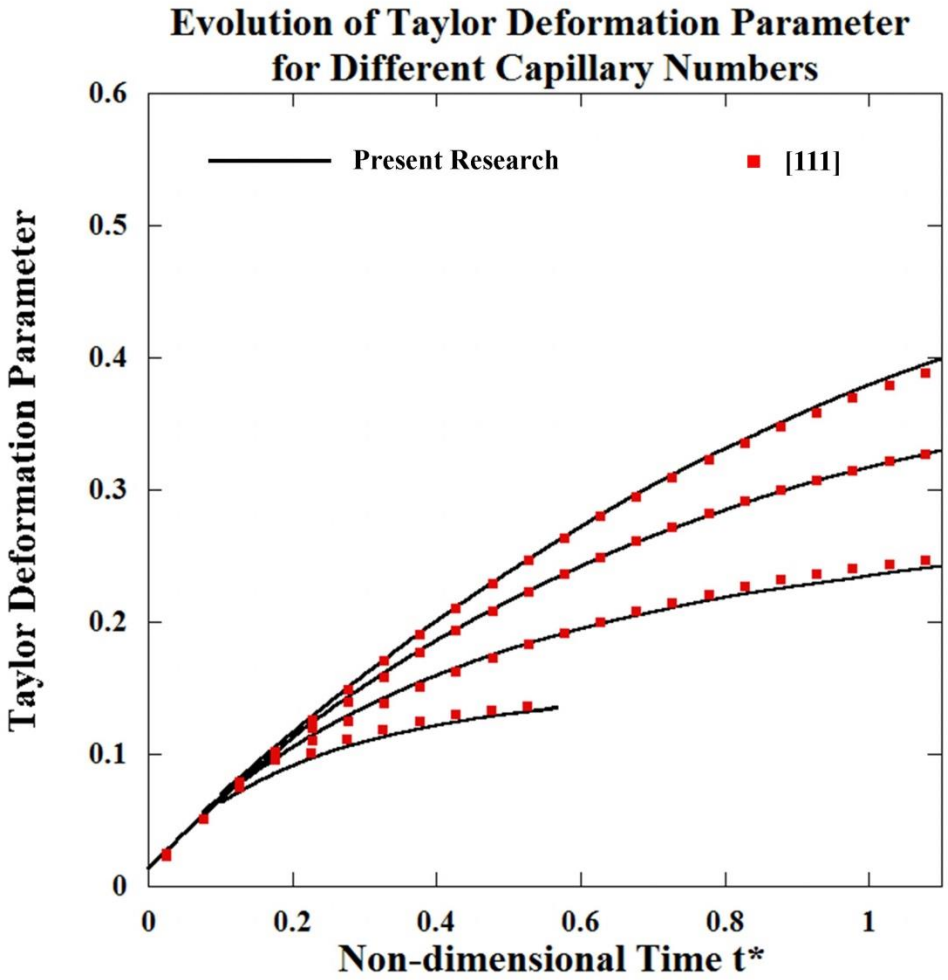

Figure 4-9: Evolution of the Taylor Deformation Parameter for a sphere in shear flow for various Capillary numbers compared to published results using FEM [110] described in section 4.4.1. It can be clearly seen that the NURBS models can capture the asymptotic behavior of FEM based models for the range of Capillary numbers tested.

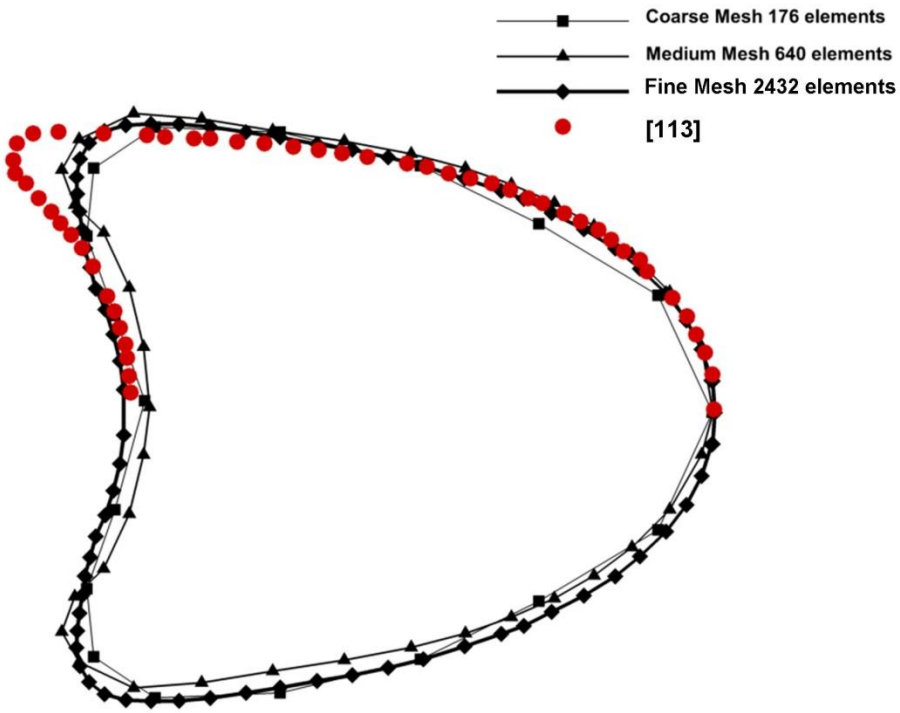

Figure 4-10: Validation of Sphere in Parabolic Flow with mesh density study compared with published data from [112], described in section 4.4.2. It can be clearly seen that the NURBS models with 176 elements captures the deformed steady state shape of the sphere. Also shown are the steady state shapes for NURBS models with 640 and 2432 elements.

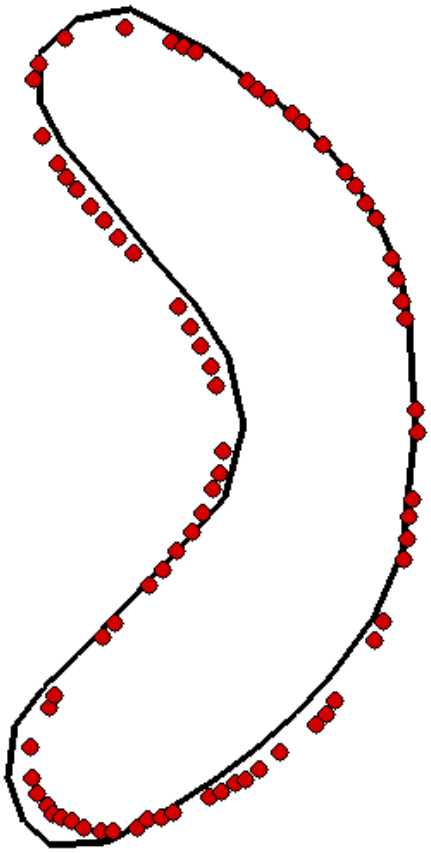

Figure 4-11: Validation of Biconcave RBC in Parabolic Flow in a Capillary with Ca = 0.1 . Steady state shapes are shown (●) [115] (—) NURBS RBC Model of present research with 440 NURBS elements. The NURBS RBC model with only 440 elements clearly captures the curvatures in the steady state shape achieved using FEM [115]

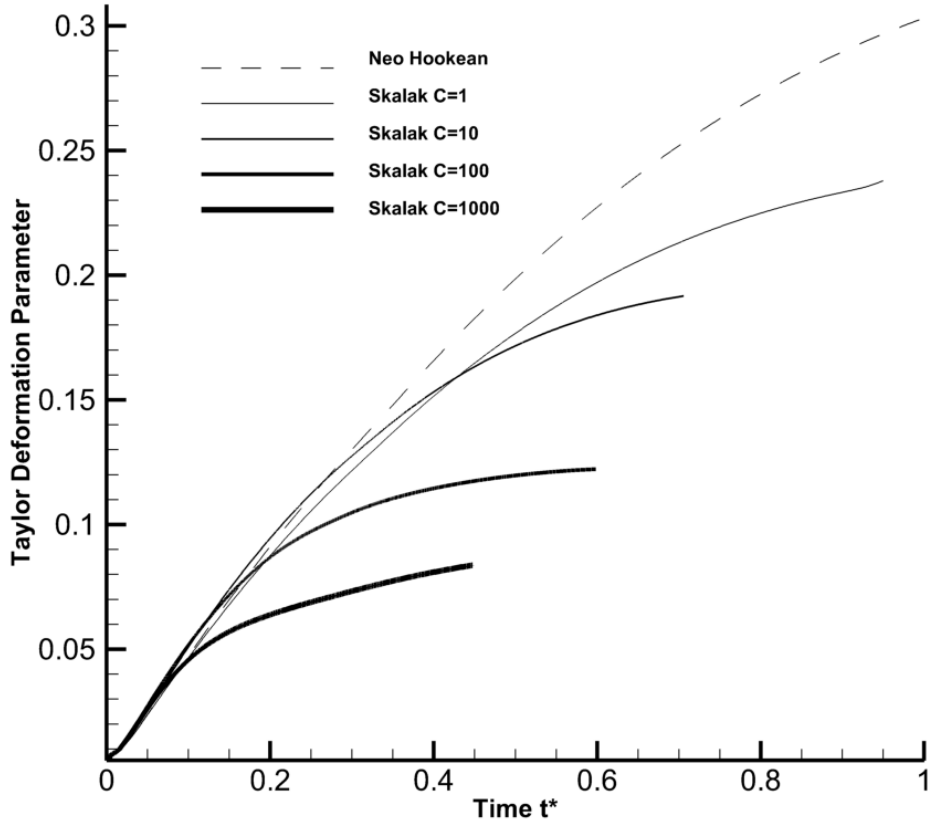

Figure 4-12: Evolution of the Taylor Deformation Parameter for a sphere in shear flow for Ca =0.1 for different Membrane Laws. The sphere undergoes lesser deformation as the membrane becomes stiffer.

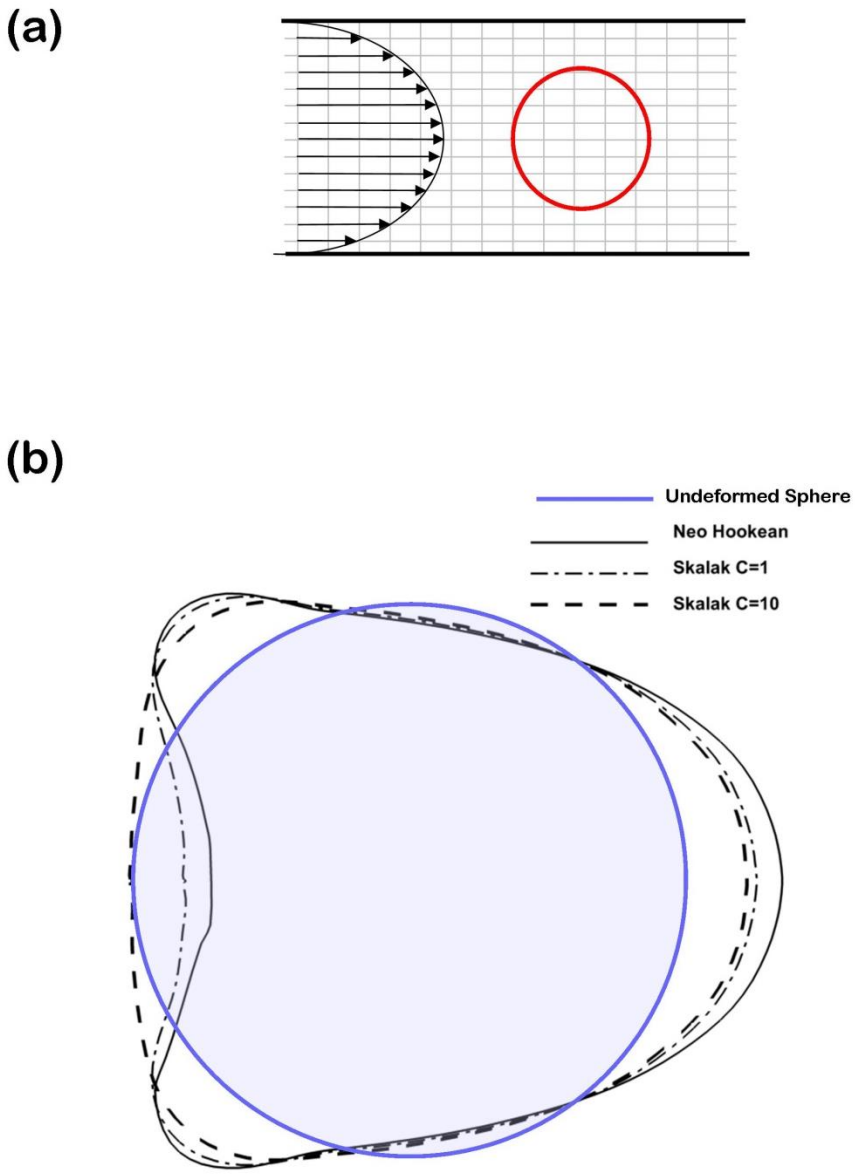

Figure 4-13: Comparison of steady state shapes shapes attained by a sphere in Poiseuille flow at Ca=0.125 in a capillary, a schematic for which is shown in (a) for different membrane models – neo Hookean, Skalak C=1 and Skalak C=10. It can be seen that the stiffer membrane models do not allow the spherical cell to deform as much as the compliant neo-Hookean model.

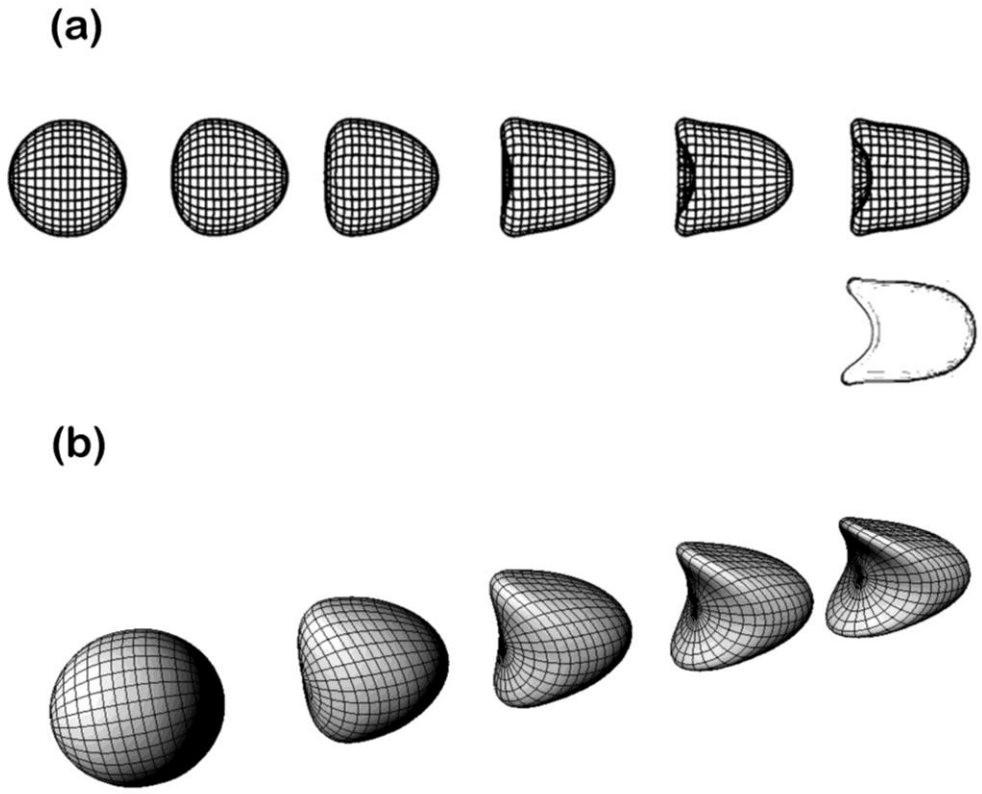

Figure 4-14:Behavior of a sphere in Poiseuille flow (a) Cross Sectional and 3-D views of the deformed shapes of a Sphere in fully developed 3-D Poiseuille flow in a tube. The Capillary number is 0.125 and the ratio of tube diameter to the diameter of the cell is 1.6. The NURBS mesh used consists of 640 elements. Also shown is a digitized image of the experimentally obtained shape of a capsule in a parabolic flow with Ca = 0.125[116] (b) 3-D views of the deformed shapes of a Sphere in fully developed Poiseuille flow in a tube. The Capillary number is 0.6 and the ratio of tube diameter to the diameter of the cell is 1.6. The NURBS mesh used consists of 640 elements.

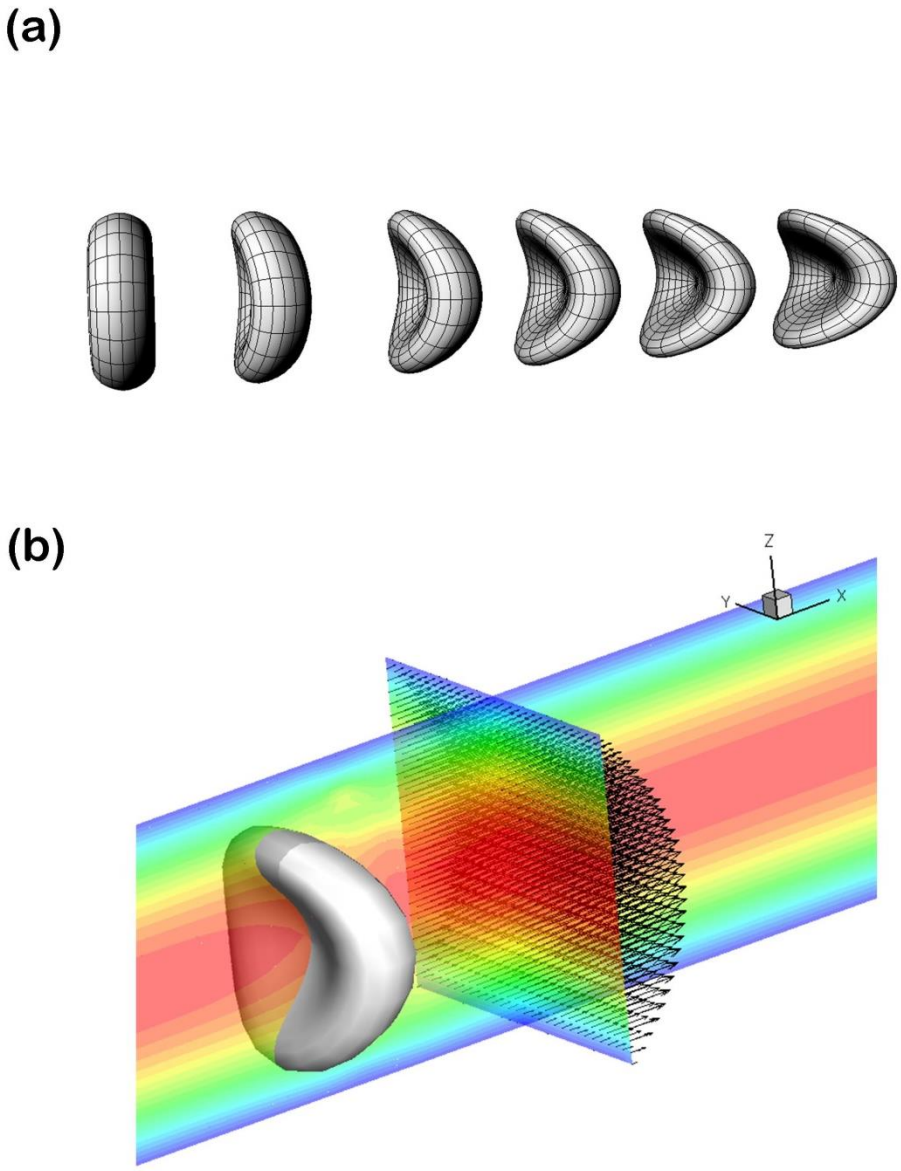

Figure 4-15: Behavior of an RBC in Poiseuille flow (a) 3-D views of the deformed shapes of a RBC in fully developed Poiseuille flow in a tube. The Capillary number is 0.6 and the ratio of tube diameter to the diameter of the cell is 1.6. The NURBS mesh used consists of 440 elements. (b) Flowfield around the RBC in the computational domain, with the velocity vectors depicting the Poiseuille flow shown.

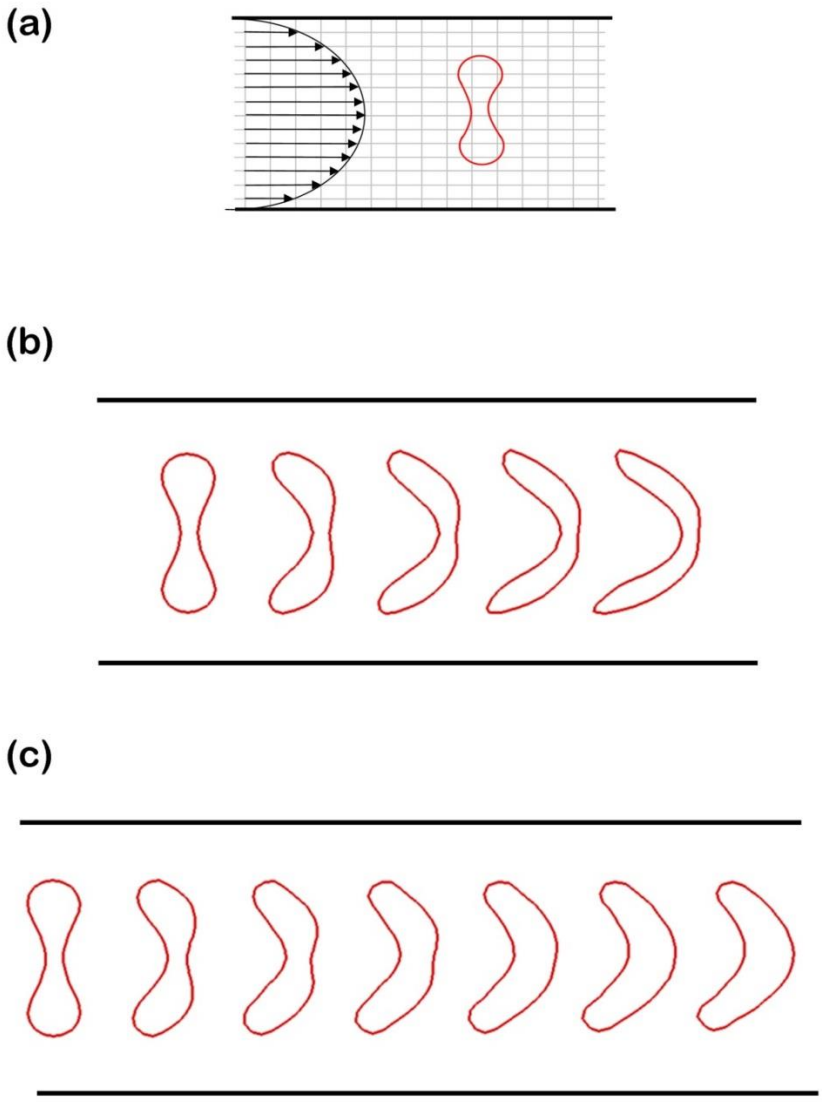

Figure 4-16: Stages of deformation of RBC in Parabolic (3D Paraboloid) flow, a schematic of which is shown in (a). The Capillary Number Ca = 0.1 and the membrane law is the classic neo-Hookean law in (b) and the Skalak Law (c).

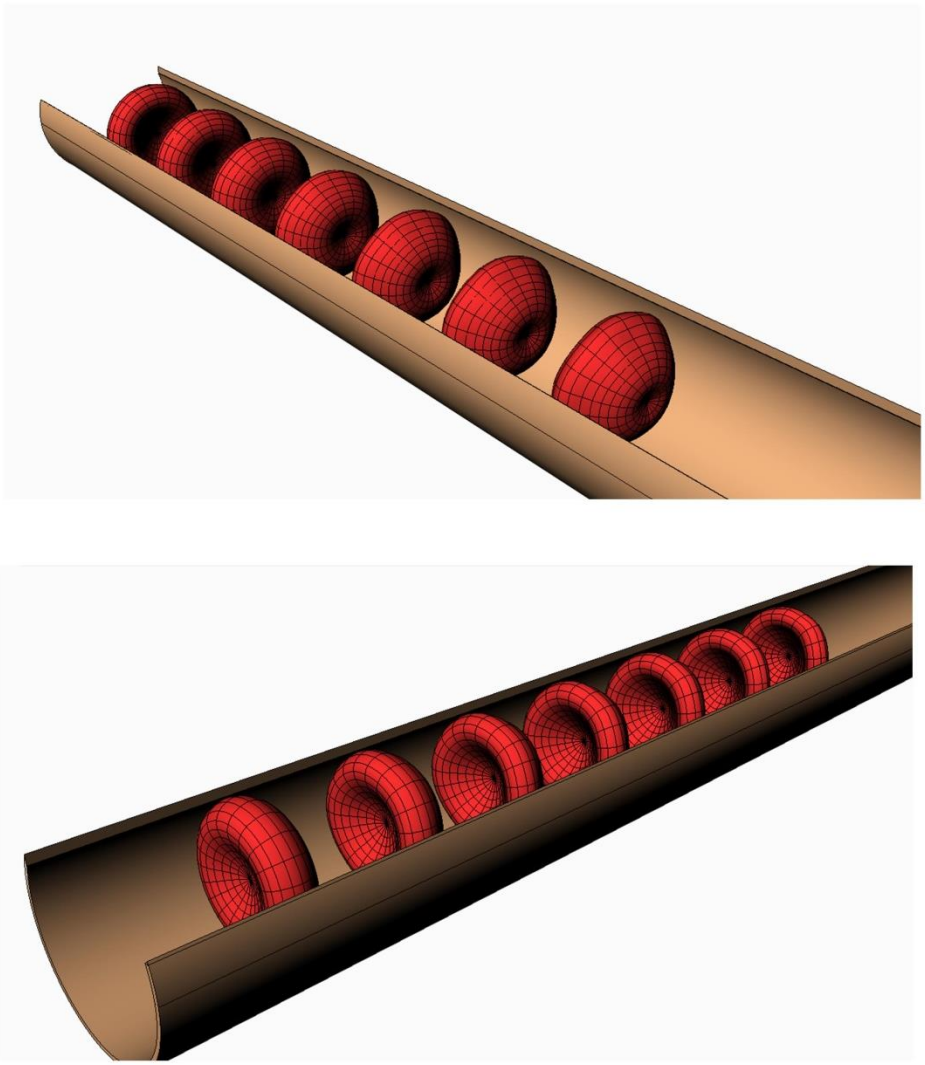

Figure 4-17: Stages of deformation of RBC in Parabolic (3D Paraboloid) flow for Ca = 0.1 and using the Skalak Membrane Law in 3D (previous image in rhino).

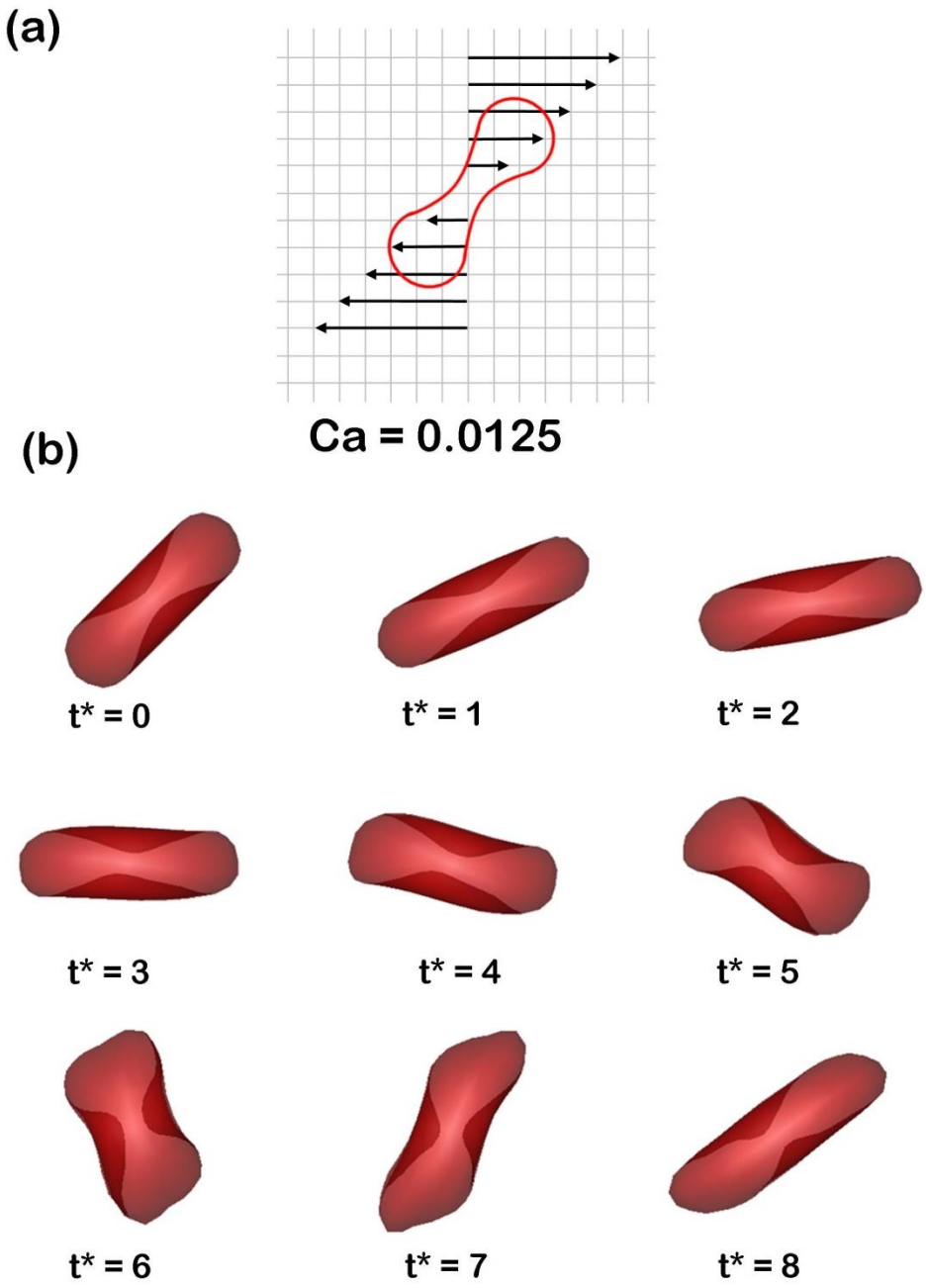

Figure 4-18: Stages of deformation of RBC in Shear flow at Ca = 0.0125 for the membrane law Skalak C = 1. The RBC undergoes an almost rigid-body like rotation. The NURBS RBC model has 440 elements (a) Schematic of flow setup (b) Stages of deformation of RBC. t* denotes non-dimensional time

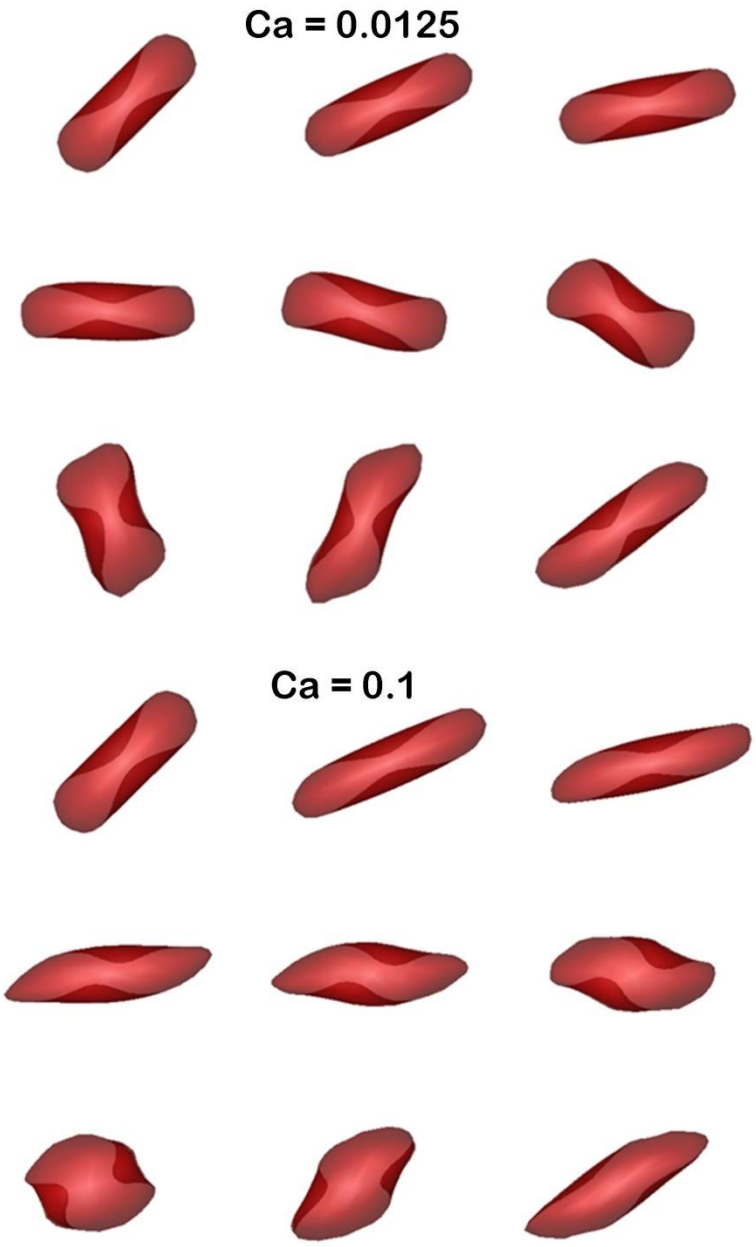

Figure 4-19: Stages of deformation of RBC in Shear flow at Ca = 0.0125 (top) and Ca = 0.1 (bottom) for the membrane law Skalak C = 1. The RBC undergoes an almost rigid-body like rotation for the lower capillary number, while it undergoes considerably more deformation at the high capillary number of 0.1. The RBC model has 440 NURBS elements and the time intervals are the same as the previous image.

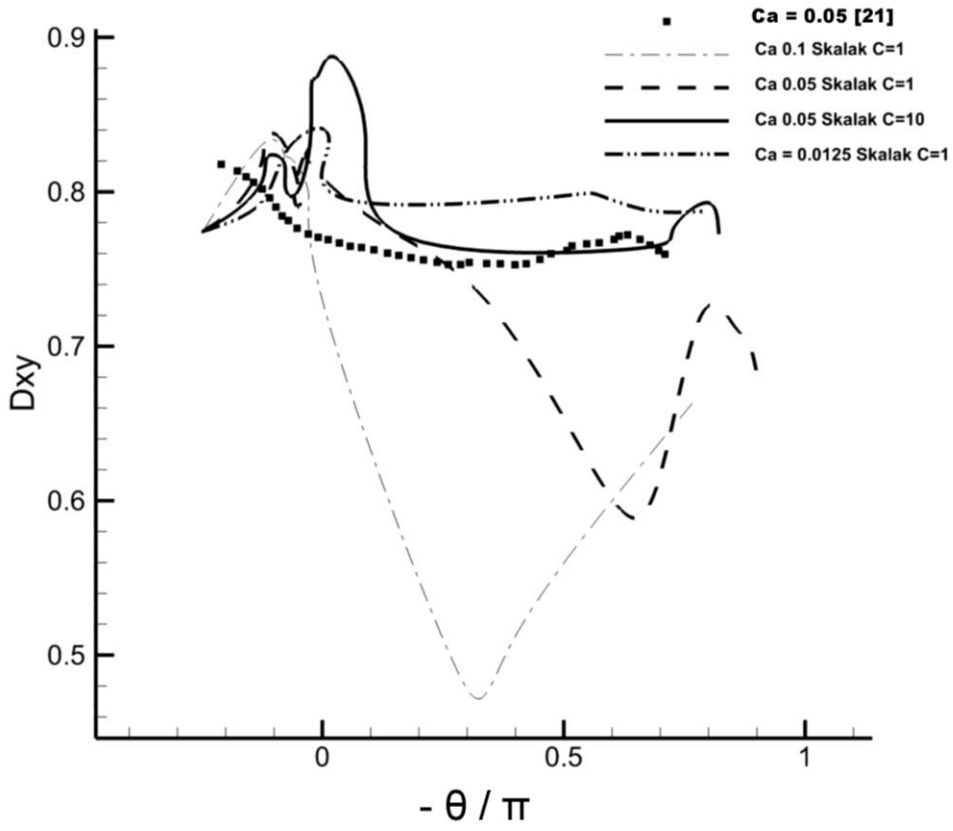

Figure 4-20: Evolution of the deformation parameter Dxy with orientation for different capillary numbers and membrane models. Also shown is the deformation parameter obtained in [21] for Ca = 0.05. It can be seen that as the capillary number increases, the RBC undergoes more deformation leading to a larger deviation of Dxy from the rest state.

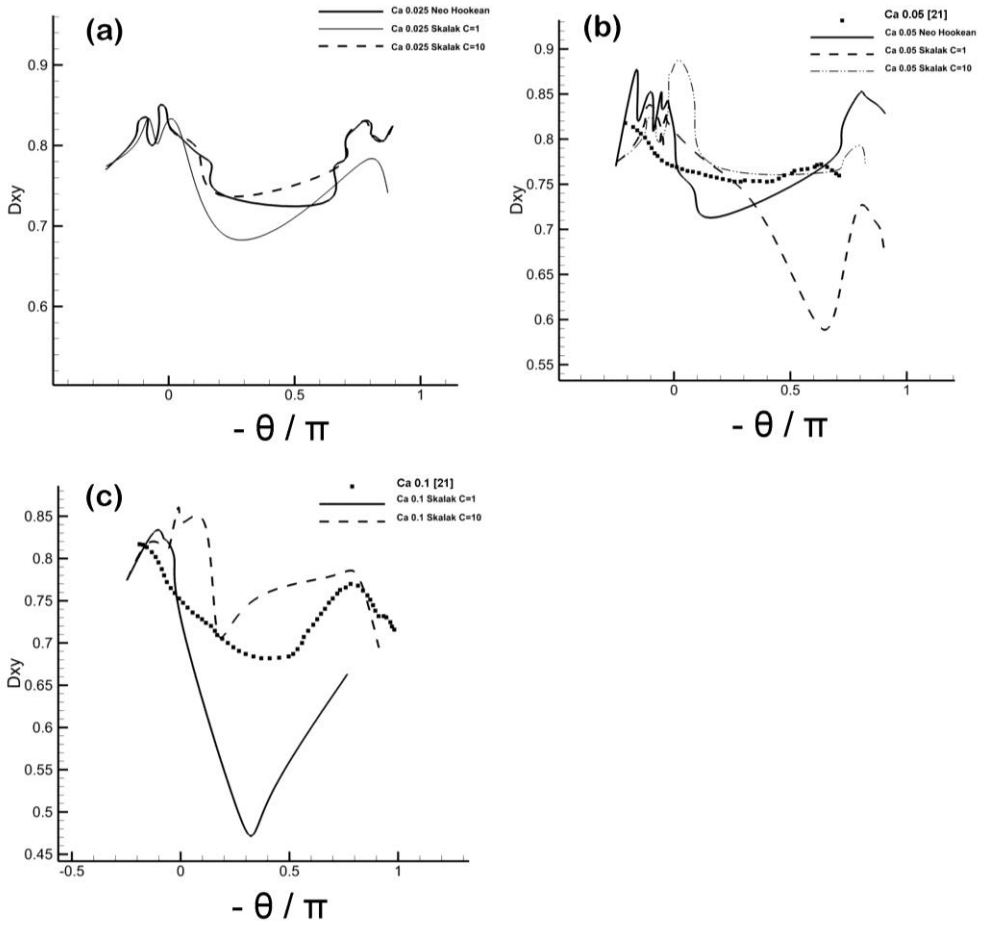

Figure 4-21: Evolution of the deformation parameter Dxy with orientation for different capillary numbers and membrane models. Also shown is the deformation parameter obtained in [21] for Ca = 0.05 and Ca = 0.1. It can be seen that as the capillary number increases, the RBC undergoes more deformation leading to a larger deviation of Dxy from the rest state. (a) Ca = 0.025 (b) Ca = 0.05 and (c) Ca = 0.1

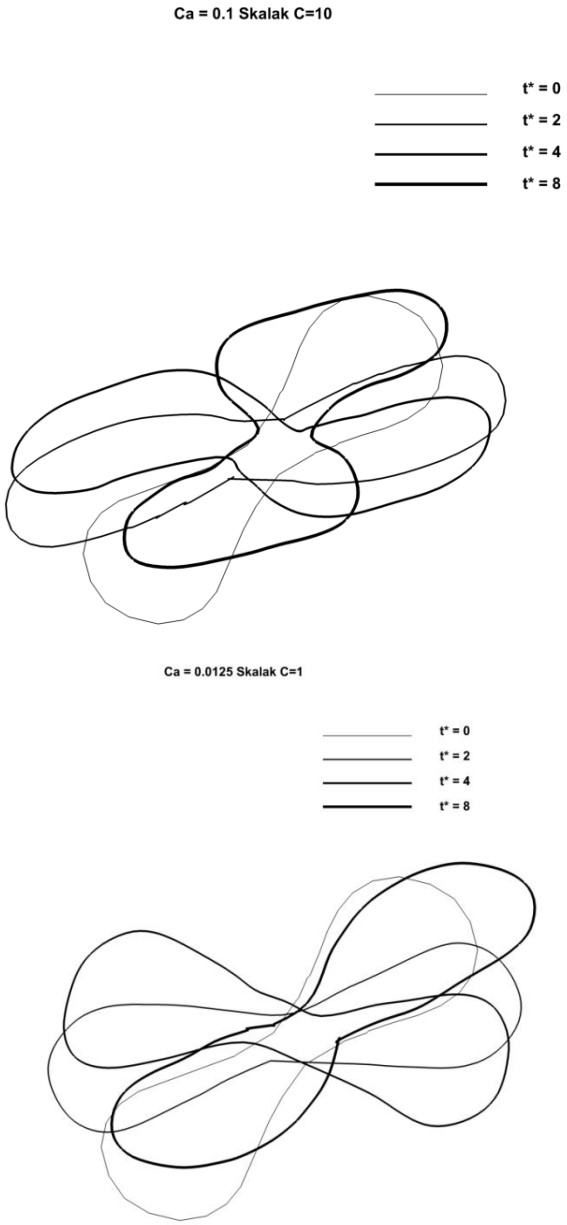

Figure 4-22: Comparison of deformed configurations of RBC in the midplane of the flow domain for Ca = 0.0125 (Skalak C=1 model) and Ca = 0.1 (Skalak C=10 model). It can be seen that while the RBC undergoes almost rigid body-like rotation for the lower capillary number, it deforms considerably for the high capillary number case.

CHAPTER 5

ENABLING EFFICIENT MODELING OF LARGE NUMBER OF CELLS INCLUDING CELLULAR INTERACTIONS

5.1 Introduction

One of the primary objectives of this research is to develop a framework for modeling and simulating the micro-scale blood particulate dynamics, along with implementing a novel methodology to model a single particulate. However simulating multiple particulate dynamics is non-trivial due to restrictions in the computational and modeling domains. This chapter primarily deals with the computational architecture implemented in order to simulate multiple cells. A brief overview of the scale of the problem at hand is presented, followed by a description of the computational architecture. The FSI problem is revisited from a multiple particle simulation perspective and finally some basic test cases simulating multiple particle dynamics are presented using the implemented approach.

5.2 Modeling Large Number of Blood Cells: The Scale of the Problem

Human blood is a dense suspension of multiple particulate matter, which makes up roughly 45% of the blood by volume [2]. This translates to over 2.5 x 10^{13} blood particulates in an average human body at any given point of time [1]. The blood particulates traverse the circulation, passing through blood vessels ranging from *O(cm)* – *O(μm)*; i.e. they traverse though pathways that are three orders of magnitude apart. Along the way they encounter countless bifurcations, high shear flows and are constantly colliding and interacting with each other. Modeling blood flow through the human body by taking each blood particulate into account is a non-trivial problem due to the unimaginable scale. Modeling a single drop of blood would entail simulating 10 million blood particulates, each deforming and behaving in its own way. Thus the problem of

modeling blood particulate dynamics at a relatively physiological level is a tremendous challenge, and one that researchers have been attempting to solve from almost a century [2,9,12,22].

While a comprehensive review on modeling blood particulate dynamics is out of the scope of this work, an attempt has been made to mention some of the important approaches. Refer to Chapter 2 for more details and references. A multi-particle 2-dimensional simulation was performed by AlMomani et al [14] who used pseudo-rigid particles for RBCs and rigid particles for platelets. Particle-particle interactions were accounted for based on the distance between particles. Modeling blood particulates as rigid or pseudo-rigid particles was used by many researchers in as it enabled capturing some of the interactive dynamics while attempting to model multiple cells with the available computational capability. Chakroborty et al [123] used a smoothed profile method to model blood particulate dynamics in 2-D. Chesnutt and Marshall [124] used discrete element method while keeping the particles rigid ellipsoids. They modeled cell aggregation and flow dynamics through bifurcations simulating up to 2500 particles. Sun and Munn [10] used a Lattice-Boltzmann method to simulate the aggregation and flow of 2-dimensional blood cells modeled as rigid capsules interacting with each other. There were multiple investigations on blood flow simulations using deformable blood particles in 2-dimensions. Secomb et al [104] used multiple deformable blood particles to study migration and bifurcation flow behavior. Zhang et al [113,125] modeled RBCs as 2-dimensional deformable particles using the Lattice-Boltzmann method and used the IBM for FSI and cell-cell interactions. Doddi and Bagchi [126] and Bagchi [11] used FEM and IBM for simulating the motion of 2-dimensional RBCs in capillary flow.

It is only over the past two decades that researchers were able to delve into 3-dimensional simulations on account of the advancements in computational capability. Pozrikidis [21,127,128] used a combination of quadratic elements based FEM and IBM to simulate the motion of RBCs in canonical flows. Dupin and co-workers [18,129,130]

modeled blood particulates as fully deformable 3-dimensional particles using the Lattice-Boltzmann Method and applied their models to simulate various flow conditions. Doddi and Bagchi [31] used FEM to simulate the flow of spherical and biconcave particles in Poiseuille flow in a capillary in 3-dimensions using IBM. While many attempts have been made thus far in modeling blood particulates in three-dimensions, achieving a physiologically realistic simulation continues to remain a challenge [23]. While the majority of modeling techniques for RBCs involve the use of the FEM, they are characterized by the use of large number of elements per cell , typically *O(1000)* - *O(10,000)* elements [30–32,38]. This makes the calculations highly computationally intensive, especially when attempting to simulate multiple cells. Furthermore, most FEM approaches use lower-order elements, which negatively affect accuracy [39]. There have been some attempts at achieving coarse-grained models [60], but this leads to a loss in resolution of the geometry [50] along with the accuracy of stress calculations. Various methods exist for simulating blood cells in relatively high fidelity – ranging from the Lattice Boltzmann method [10], Discrete Particle Dynamics [60] and multiparticle collision dynamics [131] ; however simulating a large number of cells in a dynamic environment becomes impractical and unfeasible on account of high computing requirements.

The current research attempts to use a novel isogeometric modeling technique to achieve accurate and efficient coarse-grained blood particulate models using NURBS. Moreover, using the combination of NURBS and IBM, the current research also aims to implement a computationally efficient architecture to model and simulate multiple particulates to achieve a large-scale, scalable simulation framework to model large number of cells in the future. The computational architecture should be able to adapt dynamically in both space and time with respect to the available computational resources. Moreover it is envisioned that the architecture be able to handle multi-scale simulations involving meso-scale and micro-scale particles, often simultaneously.

The computational architecture being implemented should adhere to a set of objectives based on both practicaland extensible constraints:

1. It should be based on an Object Oriented Programming(OOP) Structure
2. It should cater to multiple insertions and deletion of particles based on flow conditions
3. It should possess the ability to work with particles of multiple genres (meso-scale or micro-scale) on an as-needed basis
4. It should provide for existence of different kinds of particles (RBCs, platelets, cancer cells) of both genres
5. It should provide for efficient utilization of available memory, especially in a parallel framework

Prior to proceeding with the actual computational architecture, a brief background is provided about the need for OOP.

5.3 Object Oriented Programming Structure

In the context of this research, the blood particulates are modeled not only as different particles with different material properties and sizes, but also from the context of multi-scale modeling. The multi-scale framework consists of three major scales – macro, meso and micro, as explained in Chapter 2. The data structure described herein is developed to cater to both the meso-scale and the micro-scale models in one unified framework. It is worthwhile to reiterate that the meso-scale models are predominantly rigid bodies while the micro-scale models are fully deformable 3-D entities. This entails different attributes to be assigned to different scale models, a characteristic which is made capable by utilizing OOP.

Particles in the meso-scale are modeled as rigid bodies – the RBCs are modeled as 3-D ellpsoids while the platelets and cancer cells are modeled as spheres of differing sizes based on the physiological dimensions. The meso-scale model of blood particulates

thus would contain generic attributes such as position of the particle center. The generic particle class would be called “Generic Particle”. This would correspond to the parent class in Figure 5-1. Attributes specific to any meso-scale particle would be defined in a class “Meso-Scale Particle” which would be inherited from the Generic Particle class. This would include attributes such as radii of the particle, velocity, torque and other dynamic attributes. The Meso-Scale Particle class would correspond to the children level class in Figure 5-1. Furthermore, accounting for the existence of different kinds of particulates such as RBCs, platelets and cancer cells, individual classes would be created for each type of particle with the aforementioned names. These classes would correspond to the object level in Figure 5-1.

Similar to the implementation of the data structure for the meso-scale particles, the micro-scale particles would also be represented in terms of classes inherited from the father level class which represents a generic particle. However, in the case of the micro-scale particle, the particle is modeled as a fully deformable 3-D particle based on the NURBS representation explained in Chapter 2. Hence it would possess NURBS based attributes such as locations of the control points, knot points, NURBS basis functions, etc. Also, the different blood particulates are modeled with physiologically realistic shapes and dimensions – the RBC is modeled as a biconcave ellipsoid, the platelet and the cancer cell are modeled as deformable spheres with their respective material properties. Hence the schematic of the data structure for representing the micro-scale particle would be similar to that of the meso-scale particle but containing the NURBS attributes, as shown in Figure 5-1 which incorporates the descriptions of both meso-scale and micro-scale particles, depicting the framework of the particulate representation.

5.4 Linked List Architecture

A Linked List (LL) is a data structure that is similar to an array. While an array only stores a set of values like velocity, pressure, etc., it does so in a consecutive block of memory. This translates to the restriction of availability of consecutive memory locations to store and retrieve data. While arrays may be simple to implement on a small scale, it is not suited for large scale applications when a multitude of different data types are involved. As explained earlier, an OOP based data structure is implemented for obtaining the flexibility of dealing with multiple particles of multiple genres under a unified framework, as proposed in OBJ-II and OBJ-III. The presence of this transient environment necessitates the use of a dynamically robust data structure. Hence the implementation of a LL-based architecture was chosen and implemented.

The fundamental difference between an array and a LL is that while an array allocates memory for all its elements together as one block and is not dynamic in nature, a LL separately allocates memory for each of its data entries, called "nodes". This data entry consists of two parts – data and a pointer. The data portion of the LL may be comprised of any kind of data – ranging from standard variables like integer or float to complex data types like objects of a class. The pointer section of a node is akin to a link in a chain – it points to the memory location of the next node in the LL. A schematic is shown in Figure 5-2.

A LL is created when multiple nodes are inserted connected to each other. The LL is identified by the first node, called the "head" node. The head node usually does not contain any specific data, but is the most important node, as its pointer section contains the memory address of the first actual data-containing node of the LL. The LL is populated as more nodes are inserted, with the location of each succeeding node being "pointed to" by the pointer section of each preceding node. A schematic of how a LL is populated is shown in Figure 5-2(b).

5.4.1 Inserting a node in a Linked List

Inserting a node is a LL is straightforward, and this is one of the most important advantages of a LL. When a node is to be inserted, memory is dynamically allocated on the fly on an as-needed basis from the available pool of memory. Once the memory is allocated, the pointer of the head node is given the address of the new node, and the pointed of the new node is assigned the address of the first node, which was initially stored in the head node. In this way, the default insertion of a node is always at the beginning of the LL. However, the architecture of the LL data structure provides for easy insertion of a node at any desired location in the LL, as shown in Figure 5-3(b),(c).

5.4.2 Deleting a node from a Linked List

Deletion of a node from a LL is as straightforward as insertion in reverse. When any specific node is to be deleted, the preceding node's pointer is simply assigned to the location of the pointer of the node to be deleted to ensure unbroken continuity of the LL. The memory associated with the node to be deleted is deallocated, thereby freeing memory space for re-utilization. During deletion, a basic check is performed so as not to delete the head node accidentally, as that would make the accessing of the LL impossible. This is shown schematically in Figure 5-3(d) for a LL initially shown in Figure 5-3(a).

5.4.3 Tailoring a Linked List for the Current Research

In the current research, it is envisioned to utilize the LL architecture to develop a framework wherein multiple cells of different genres can co-exist. It is also necessary to incorporate the ability to effect a transition of the type of the cell based on its location in the computational domain. For instance, a cell which was initially present in the meso-scale region is convected into a region designated for further analysis in the micro-scale. This necessitates that the particle transition from a rigid-body type model to a deformable NURBS based model while preserving the generic particle attributes such as position of the center, velocity, etc. At the same time it is necessary that the particle is not

recognized as an entirely new particle, but as a particle whose model has changed. In other words, the location of the particle in the LL does not change, only its model should be updated. This ability to transition should also be exercised when the particle moves from the micro-scale region back into a meso-scale domain; only here the transition is the reverse of what occurred earlier. This situation is shown schematically in Figure 5-4.

As mentioned earlier, a framework for multiple particles was explained using inherited classes and objects. In this framework, the objects of the derived classes can have attributes of either RBCs (both rigid and deformable), platelets (both rigid and deformable) and cancer cells or any other type of cells (both rigid and deformable). The importance of having the ability to have this dual-personality is brought to light in this section. Initially, when particles are initialized as objects of the derived class, they possess both attributes of rigid-body and deformable models. However, only those attributes which are necessary in any particular region are utilized, while the other attributes are "masked". For instance, if a particle is initialized in the meso-scale region, it will have only the rigid-body attributes activated, keeping the deformable model attributes masked. When the particle moves into the computational region which requires a deformable cell simulation, the attributes of the rigid-body models are masked and the deformable attributes are activated. However, the essential attributes such as position and orientation is preserved through the transition process. This is shown schematically in Figure 5-5.

5.5 Accounting for Multiple Particle Interactions using IBM

When simulating multiple particles, the presence of multiple particles needs to be communicated to the fluid. Moreover, the presence of multiple particles needs to be communicated to each other. The particles interact not only with the surrounding fluid,

but with surrounding particles as well. Thus the need arises for a framework which enables this multi-particle interaction.

There have been multiple approaches used by researchers in the past. Some of the methods include distance-based interaction models [10,14] while others have used mass-spring models [104]. However, multiple researchers have depended on IBM for sensing neighboring cells and interacting with them. IBM lends itself nicely to handling multiple particle interactions (no contact) because of its formulation. In IBM, the membrane force is distributed to the surrounding fluid points using a delta function, as shown in Figure 5-6. When multiple particles come near each other, the fluid points which are recruited for supplying forces overlap between two or more particles. In such a case, the resulting flow field takes into account the contribution from all the particles at that point. It can be compared to performing a vector sum. Indeed, the force at any fluid point is a vector sum of all the forces from all the contributing particles. Figure 5-6 shows a schematic of two particles interacting with one another by sharing the same fluid points for force distribution. Thus IBM has an inherent basic particle interaction mechanism on account of its formulation. However the interaction mechanism does not, in theory, allow contact between particles because the forces increase in a repelling nature as particles come closer. The behavior of multiple particles can be compared to using an advanced form of lubrication theory. However as an initial interacting mechanism, IBM should suffice.

5.6 Test Cases for Multiple Particles

As discussed earlier in this chapter, the modular architecture of the developed framework combined with the choice of FSI technique enables simple implementation of multiple cells. As preliminary test cases we simulated the motion of both RBCs and spherical cells for basic flow conditions.

5.6.1 Two RBCs in Parabolic Flow

As an initial case, we simulated the motion of two RBCs in capillary flow. The flow conditions were exactly the same as that used for testing and verifying the single RBC case (described in section 4.4.2). Briefly, the RBCs are placed at the center of the flow domain in a Poiseuille flow profile for Ca = 0.1. Both the RBCs are separated by a distance equal to one cell diameter. The stages of deformation of the RBCs are shown in Figure 5-7 and Figure 5-8. Figure 5-7 shows a 3D view of the restoring forces set up in the membrane on account of the deformation effected by the flow, and Figure 5-8 shows a cross-sectional view of both RBCs. It can be clearly seen that the RBCs achieve a steady state shape similar to that seen in Section 4.4.2 for the single RBC. Due to the flow velocity and the spacing between the two RBCs, neither RBC seems to be affected by the presence of the other. The RBCs were inserted as nodes in the aforementioned linked list architecture, and the FSI was performed using the same IBM technique described in this chapter and earlier, with the main different being the possible contributions by multiple solid points to the same surrounding fluid points. Also, both RBCs were simulated with an internal to external viscosity ratio of 5.

5.6.2 Two Spheres Interacting in Linear Shear Flow

For a more rigorous testing of multiple cells interacting with each other, two spheres were placed in a linear shear flow in such a way that they are convected towards each other. As shown in the schematic in Figure 5-9(a), the distances Δx and Δy can be varied. Different initial locations of the sphere were tested for multiple Ca. The spheres, like the RBCs in the earlier case were introduced as nodes in the linked list architecture with the main difference being the viscosity ratio between the internal and external fluids which was maintained at unity.

Figure 5-9(b) shows the stages of interaction of the two spheres for Ca = 0.05. The two spheres were placed initially such that $\Delta x=2.5$ and $\Delta y=1.0$. Every screen shot in

Figure 5-9(b) shows the configuration of the two spheres at time intervals of non-dimensional time dt* = 1000. The spheres initially deform according to the shear flow and also begin to travel towards each other. When the two spheres are close enough such that they begin to feel the presence of each other, the shapes of the spheres no longer remain symmetrical, but begin to show asymmetery, as though the spheres are trying to force themselves into one another. As the spheres get closer to each other, their centers of mass shift away from the centerline trajectory and the portion of the membrane facing the other sphere flattens. As the spheres continue on their trajectory, they begin to regain their curvatures and start to recover the shape that they had prior to interacting with one another.

Figure 5-10 shows the stages of interaction of two spheres placed apart by the same distances, i.e. $\Delta x=2.5$ and $\Delta y=1.0$ but for a much higher Ca=0.15. As the Ca is three times that of the previous case, the spheres begin to interact with each other even before they have had the time to reach their steady state shapes in the shear flow. As a result, the spheres jump over one another, undergoing rotational motion as well as translational motion. Figure 5-11 shows the stages of deformation for the same Ca of 0.15 but with the spheres placed much farther apart, $\Delta x=3.5$ and $\Delta y=0.5$. Even though the separation along the y-direction is reduced, the increased separation in the x-direction allows the spheres enough time to achieve a steady motion prior to interacting with each other. As a result the spheres deviate from their original path similar to the earlier case for Ca=0.05, but by a different extent. Figure 5-12 quantifies the trajectory of the centers of the two spheres for the cases mentioned thus far. Also shown is the trajectory for a similar case of Ca=0.15 from the study by Lac et al [132]. It can be seen that the trajectory for the case of Ca=0.15 closely follows that of Lac et al until the trajectory reaches its highest point, following which the trajectory in the present study drops at a faster rate. This may be due to the variation in the starting positions for the two cases. In the case of Lac et al, the spheres started much farther away from each other in the x-direction. As a result, the

spheres would have possessed more time to reach a steady motion compared to the current study. This is only a preliminary simulation, and more testing is underway to investigate the interaction between two spheres in a shear flow.

5.7 Discussion and Summary

In the current chapter, incorporating a framework to model multiple cells was discussed. Simulating micro-scale blood flow dynamics necessitates the ability to model multiple cells in a dynamic framework. Moreover, the framework should be able to smoothly incorporate multiple cells of different genres such as RBCs, WBCs and so on. In order to achieve the apropos, a linked list based architecture in conjunction with object oriented programming principles was implemented. A linked list enables dynamic inclusion of new nodes and deletion of existing nodes as and when necessary, making it a flexible architecture to work with. The inclusion of object oriented programming principles, viz. inheritance enables multiple cells of different genres to be modeled and simulated within the same architecture. The combination of linked lists and inheritance also provides the ability to scale the framework both in terms of number of cells and also in terms of physics of the problem. For example, the framework can be easily extended to include meso-scale models for blood particulates in addition to the current NURBS micro-scale models. The nodes of the linked lists would refer to an individual blood particulate which would contain attributes of both meso-scale and micro-scale models. The appropriate attribute would be switched on based on the type of computational domain being used. This would enable switching between the meso-scale and micro-scale models as the flow proceeds from a meso-scale computational domain where the particulates need not be highly resolved to a region where the deformability and dynamics of particulates at the micro-scale become needed, eg. the hinge region of a mechanical heart valve. Moreover, the choice of the IBM for FSI lends itself beautifully to the aforementioned framework as there does not explicitly exist a need to include the

presence of multiple particulates. The formulation of the IBM automatically incorporates contributions from multiple sources through the delta functions, thereby laying the foundation for a simple and straightforward implementation for simulating multiple particulates.

The aforementioned linked list and object oriented programming architecture in conjunction with the IBM was implemented and tested for basic cases involving RBCs and spheres. Two RBCs were simulated in Poiseuille flow in a capillary, where the RBCs did not interact with each other due to the starting positions. Both RBCs achieved steady state shapes similar to that obtained in Section 4.4.2. In order to test the ability of the developed framework to deal with interacting particles, the interaction of two spheres in linear shear flow was simulated. The spheres were placed off-center such that they would be convected towards each other by the shear flow. Various Ca and initial placements were examined, and the trajectories of the center of the two spheres was tracked. The spheres were convected towards each other after achieving a steady deformation state of tank treading provided there was enough time for the spheres to reach steady state. As the spheres approached each other, they felt the presence of each other and deviated from their original paths based on the Ca and initial placements. Different dynamics were captured for different Ca and initial placements with NURBS meshes as coarse as 176 elements for the sphere. There existed good agreement with published data for the case with Ca=0.15, however further testing needs to be performed for other capillary numbers and starting positions. To conclude, the linked list architecture in conjunction with object oriented programming provides a strong foundation for achieving simulations of large number of cells of multiple genres, with the cells being able to interact with one another on account of the immersed boundary fluid-structure interaction technique.

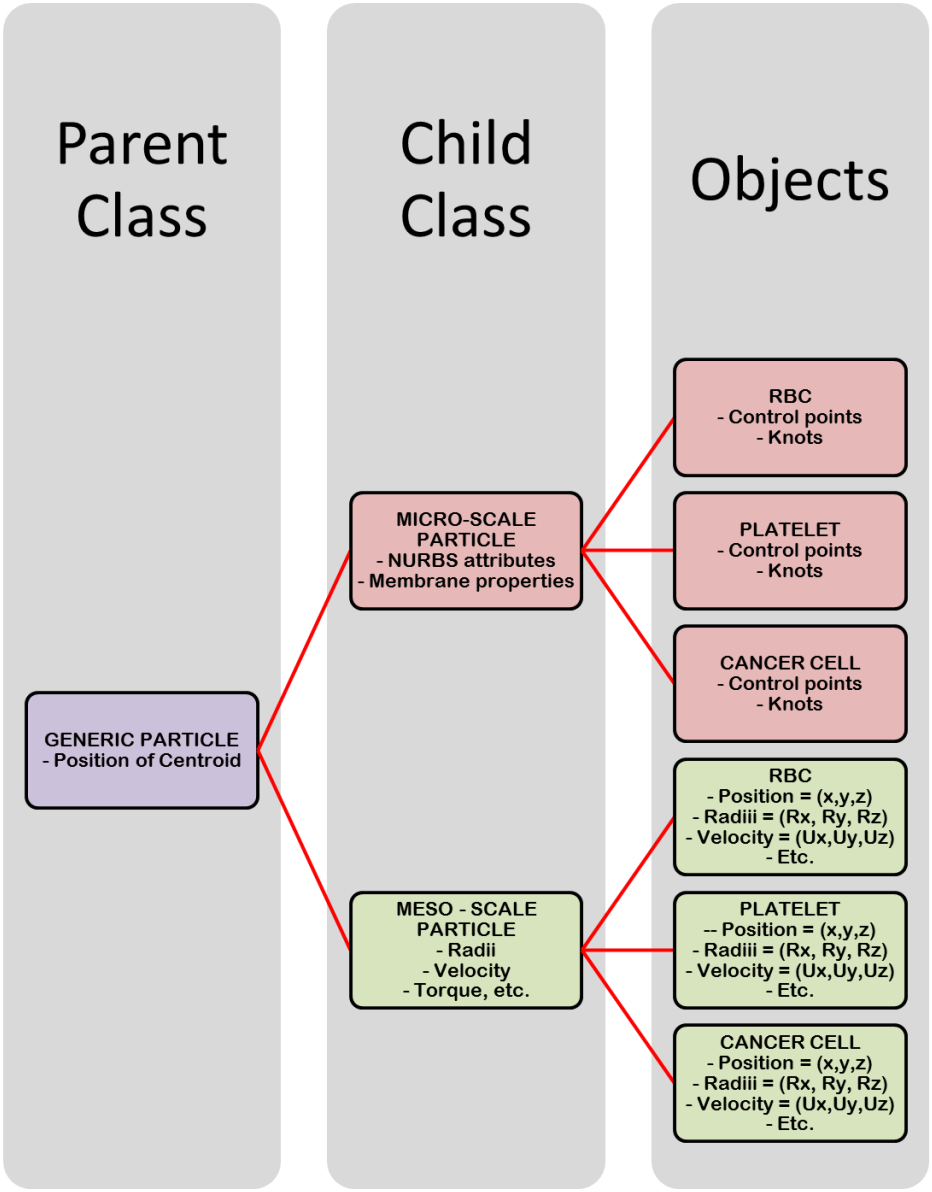

Figure 5-1: Combined framework depicting data structure for both meso-scale and micro-scale particle with information derived from a common parent particle, but consisting of individual as well as common attributes.

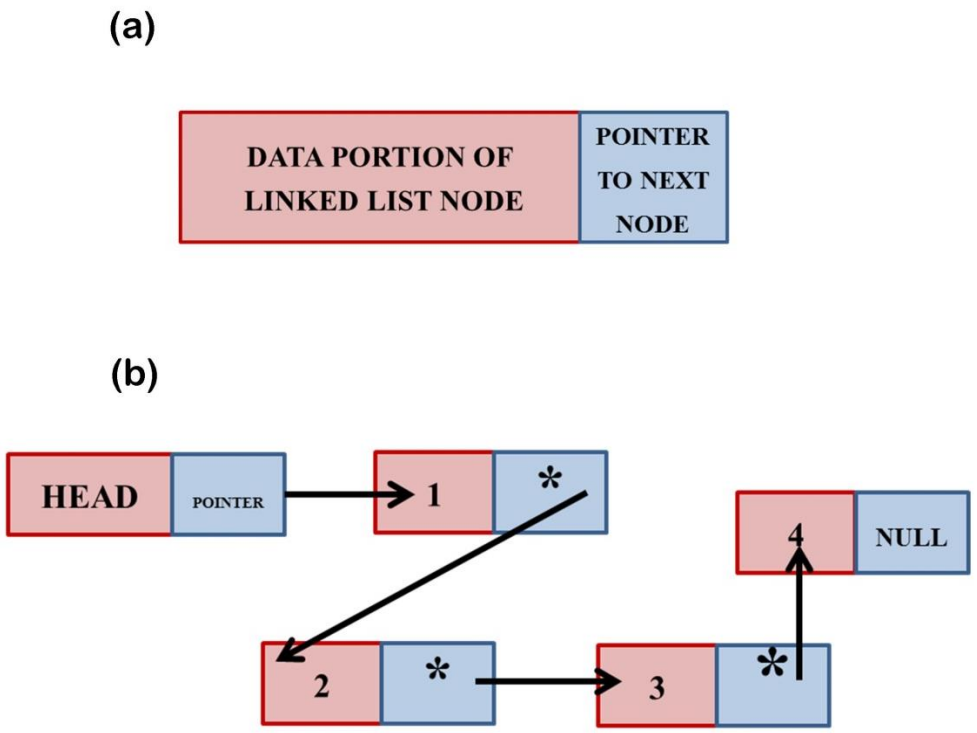

Figure 5-2: Linked List architecture (a) Components of a Linked List node consisting of the data portion and the pointer to the next node in the linked list (b) Schematic of Linked List consisting 4 data nodes and 1 head node. The locations of the nodes of the LL need not be consecutive blocks of memory.

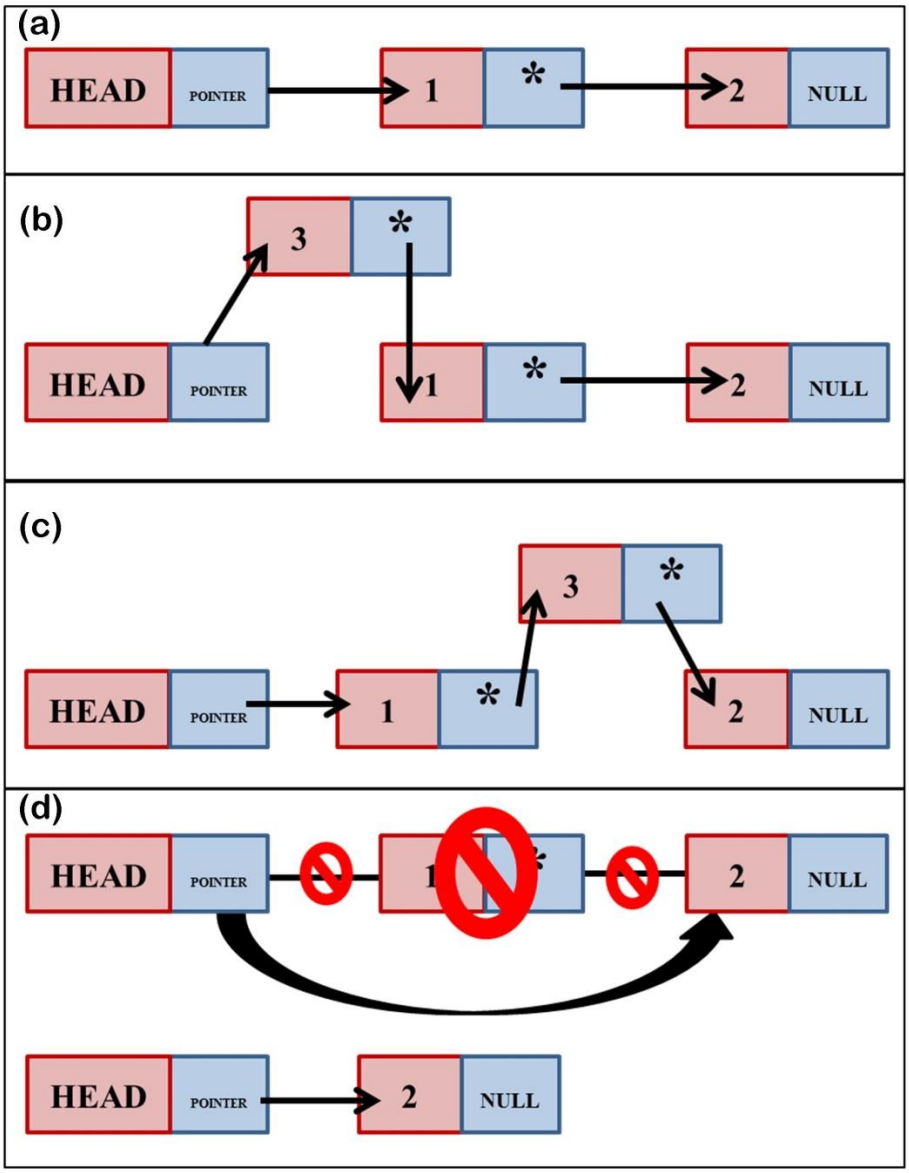

Figure 5-3: Schematic of Linked List Insertion and deletion (a) Linked List containing head and 2 nodes (b) Insertion of a node "3" after the head node (c) Insertion of a node "3" between nodes 1 and 2 depicting the dynamic insertion ability of the Linked List architecture (d) Deletion of node "1", redirecting the pointer of the head node to point to the address of node 2 to maintain continuity.

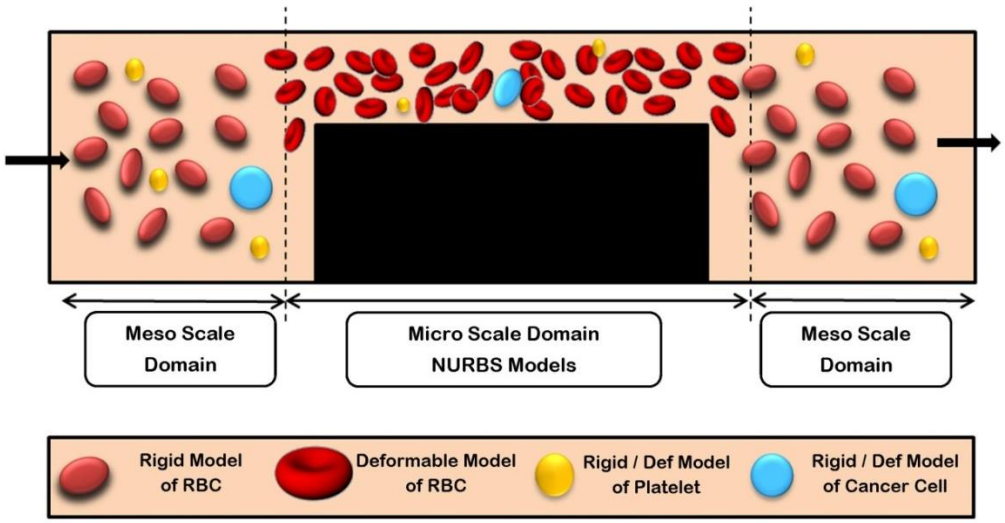

Figure 5-4: Schematic depicting a typical computational domain to be simulated, including the meso-scale and the micro-scale regions. RBCS and other cells should smoothly transition from being modeled as a rigid body model in the meso-scale regions (left and right) to being modeled as deformable cells in the micro-scale region (center).

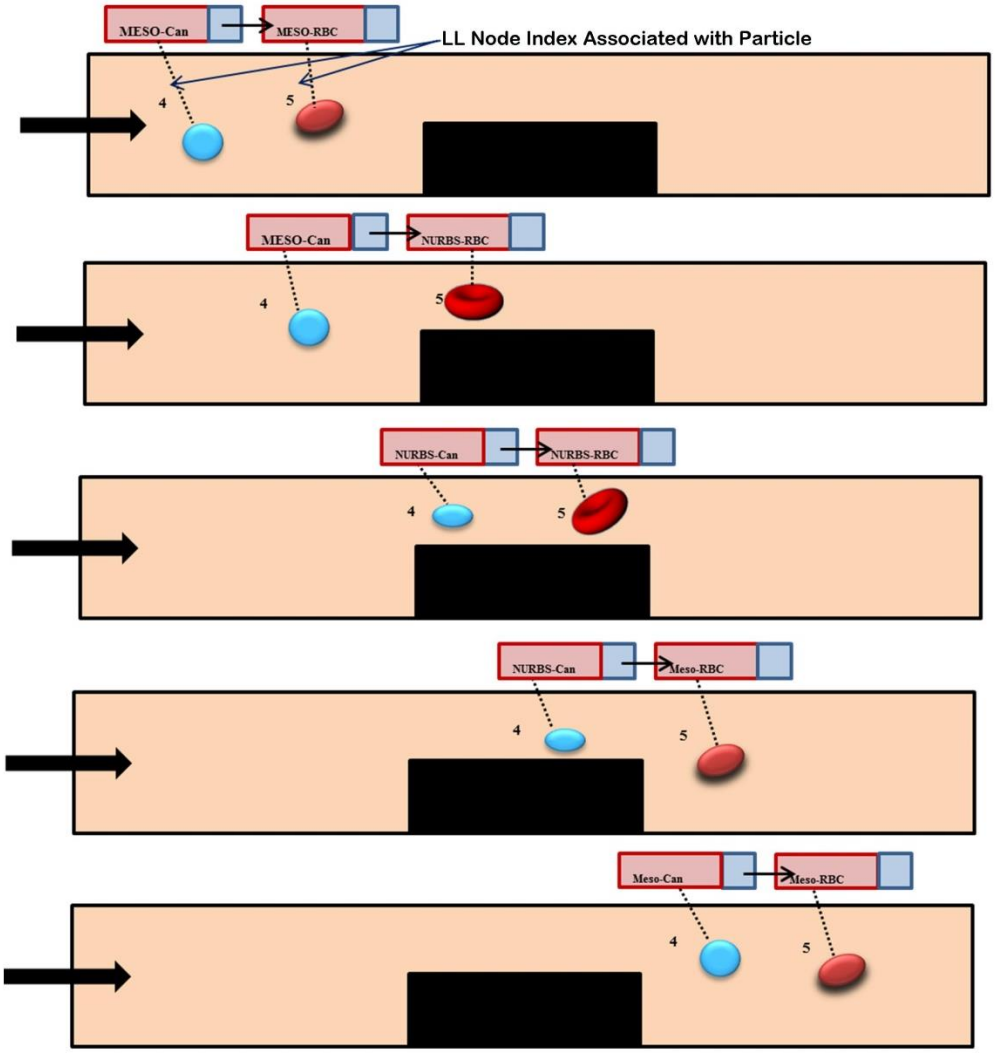

Figure 5-5: Different stages of a RBC and Cancer cell model existence. (a) Both meso-scale (B) RBC micro, Cancer cell meso (c) Both Micro (d) RBC back to meso, cancer cell still micro (e) both meso.

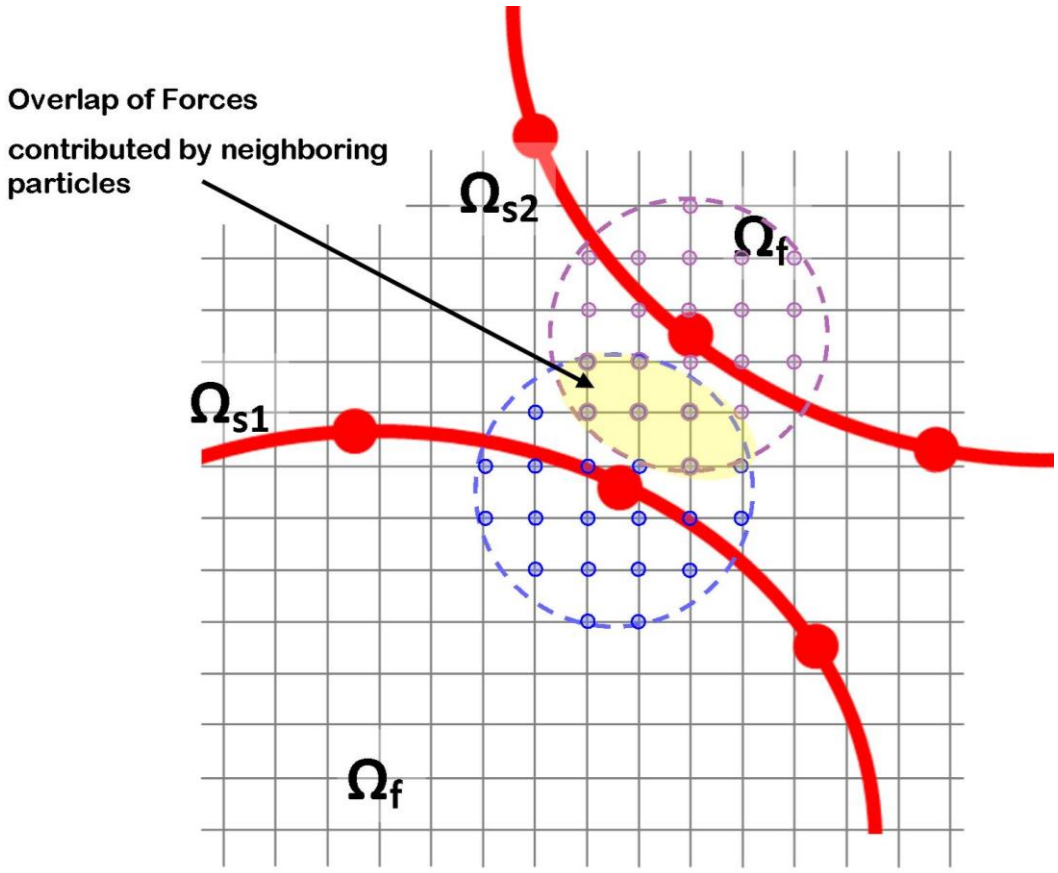

Figure 5-6: 2-D Schematic showing overlap of force distribution contributed by neighboring particles. Some of the fluid points are recruited for both particles 1 and 2, with the formation of an overlap zone where the vector sum of forces is calculated. Only the contributions from the fluid points inside the two spheres of influence shown contribute towards the boundary condition determination at the solid points.

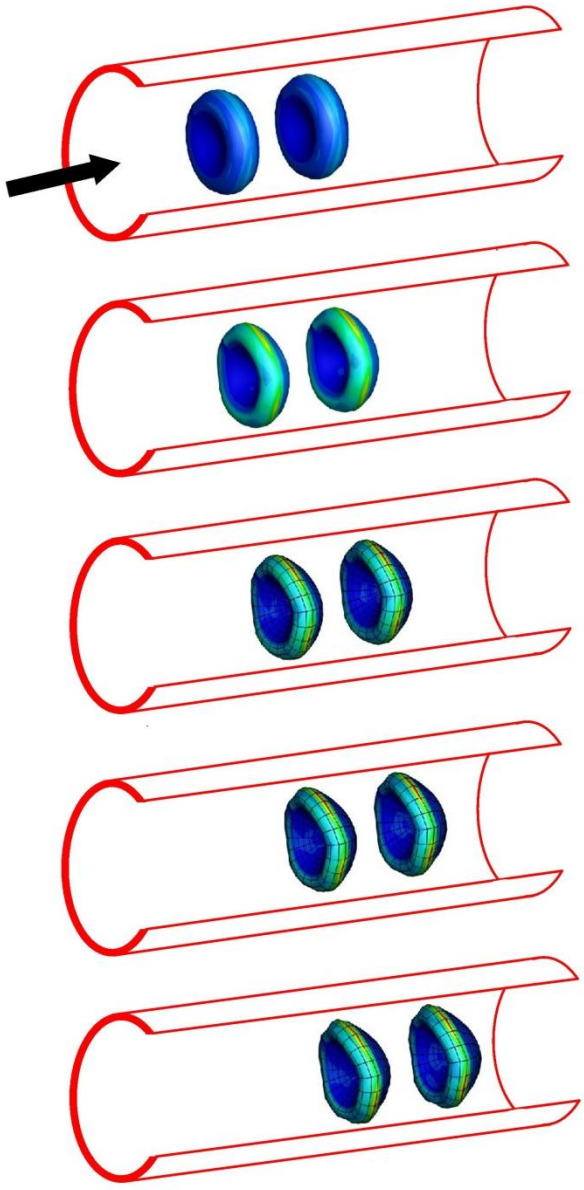

Figure 5-7: 3-D Sequence of deformation of 2 RBCs initially placed at a fixed distance apart in a fully developed Poiseuille flow profile. The contours show the membrane force generated, and the black arrow denotes the direction of flow. The RBCs achieve a steady state shape (and membrane force) beyond which they are simply convected like rigid bodies.

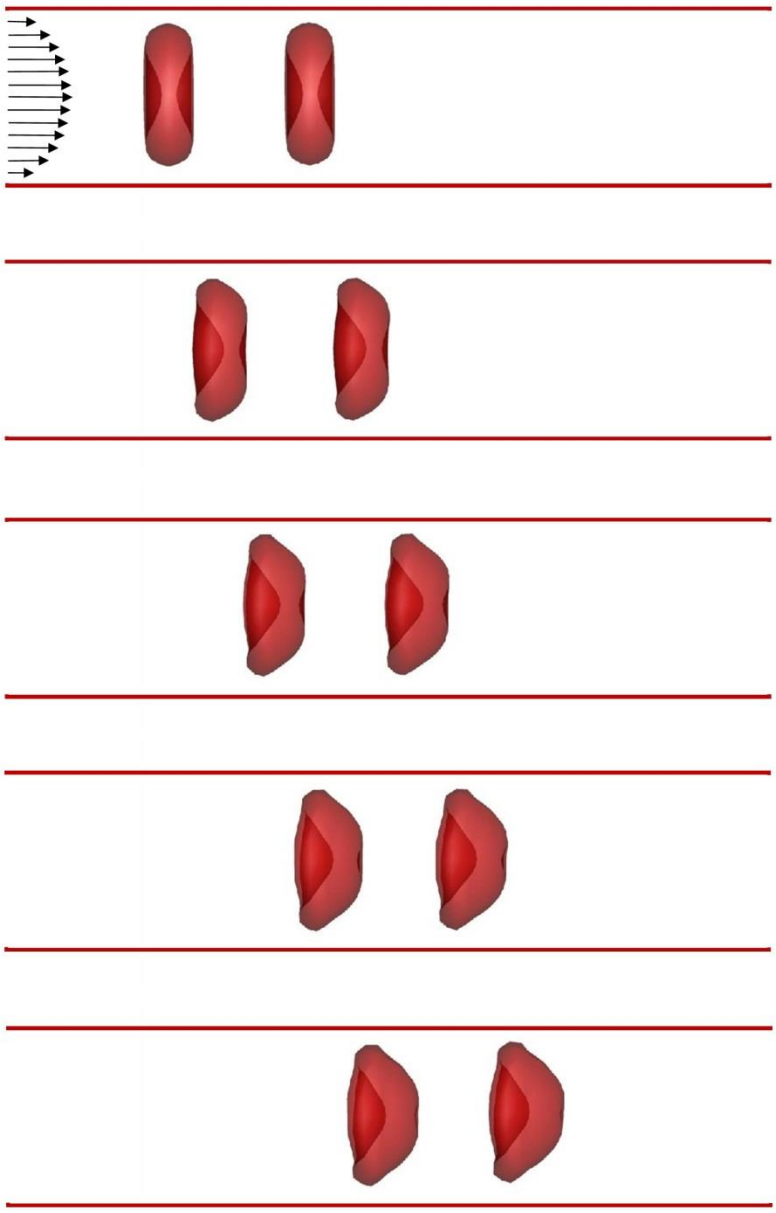

Figure 5-8: Cross-sectional views of sequence of deformation of 2 RBCs initially placed at a fixed distance apart in a fully developed Poiseuille flow profile. The black arrows (top) denote the flow profile. The RBCs achieve a steady state shape beyond which they are simply convected like rigid bodies.

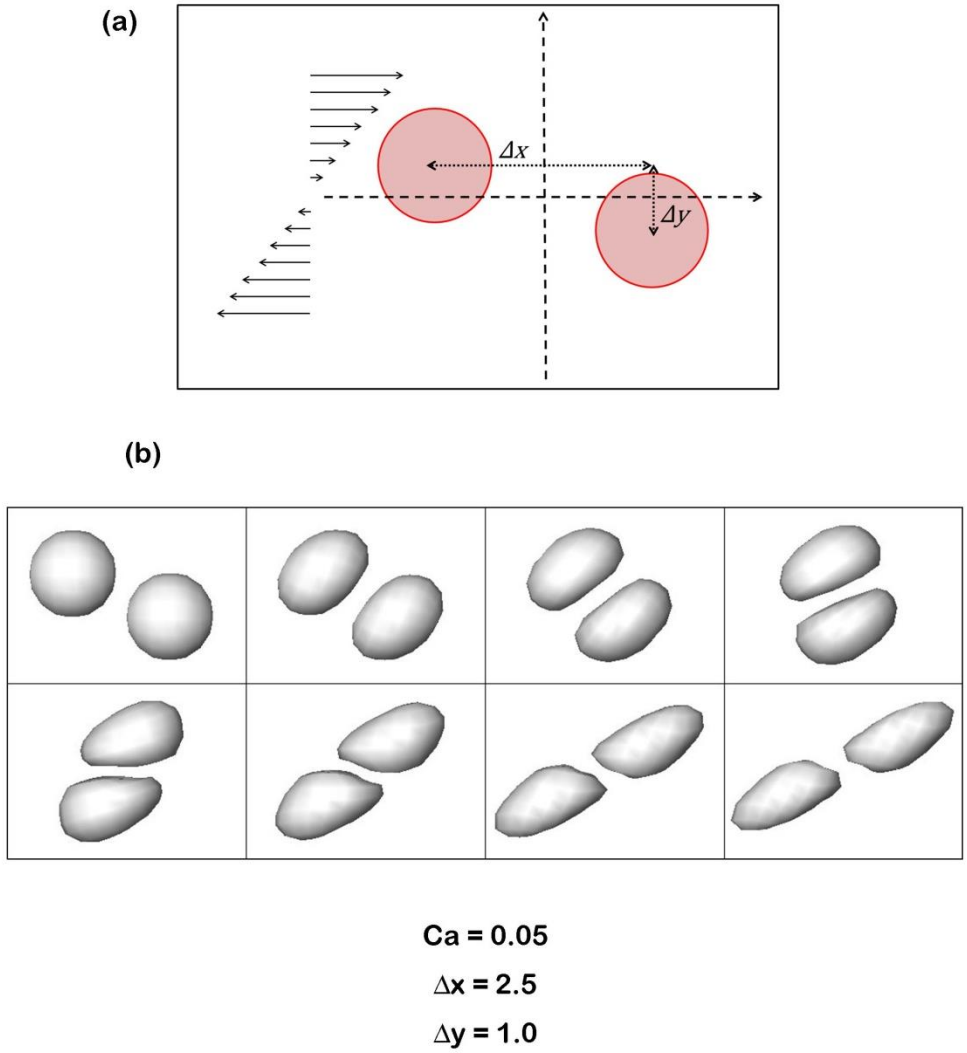

Figure 5-9: Behavior of two spheres approaching each other in linear shear flow (a) Schematic for simulating the interaction of two spheres in linear shear flow (b) stages of interaction and deformation of two identical spheres placed at a distance of $\Delta x=2.5$ and $\Delta y=1.0$ for $Ca=0.1$. The montage consists of snapshots of the positions of the spheres at equal intervals of time. The spheres approach each other, are deviated away from their original path due to the presence of the other sphere and undergo asymmetric deformation with the portion of the spheres facing each other flattening. The spheres regain their curvatures after they have passed each other.

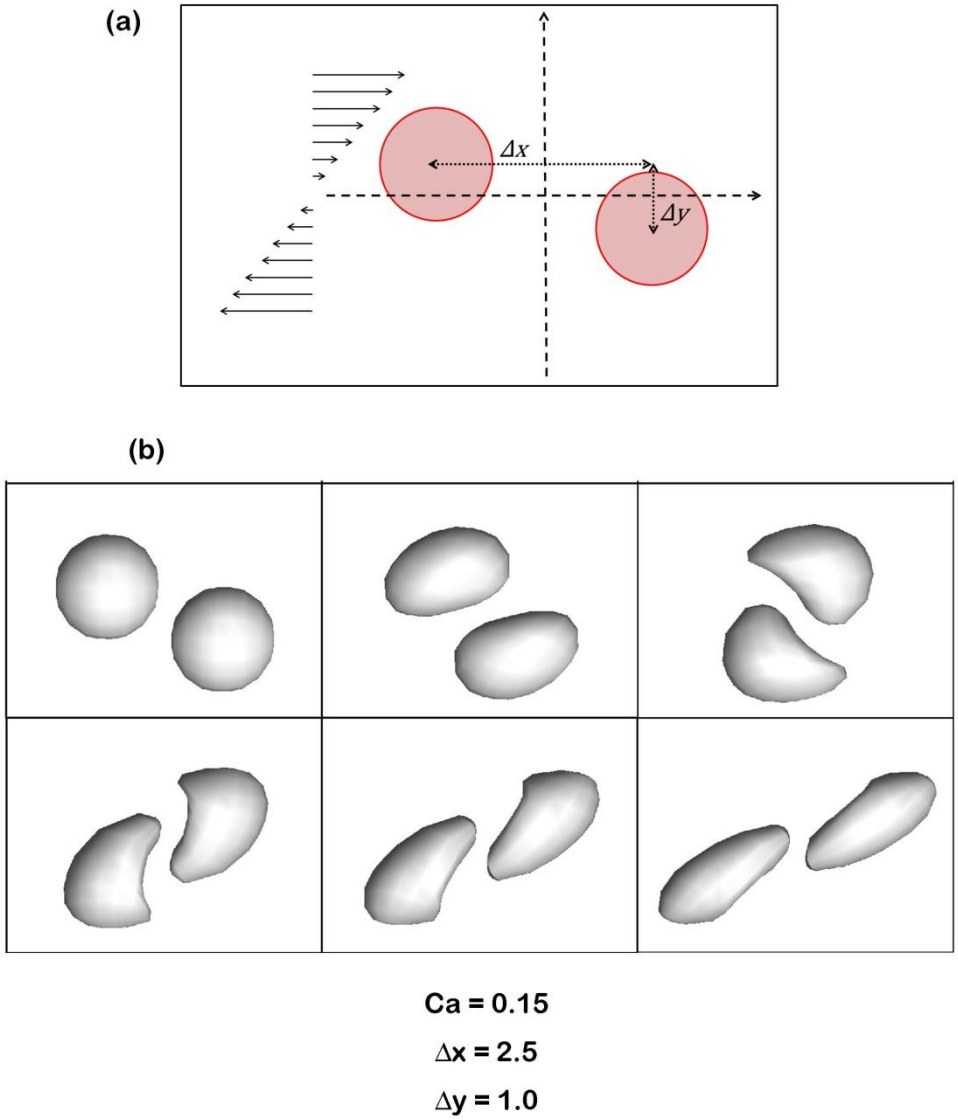

Figure 5-10: Behavior of two spheres approaching each other in linear shear flow (a) Schematic for simulating the interaction of two spheres in linear shear flow (b) stages of interaction and deformation of two identical spheres placed at a distance of Δx=2.5 and Δy=1.0 for Ca=0.15. The montage consists of snapshots of the positions of the spheres at equal intervals of time. Due to the high Ca and the close proximity of the two spheres at the beginning, the spheres do not have enough time to achieve steady deformation shapes and hence jump over one another.

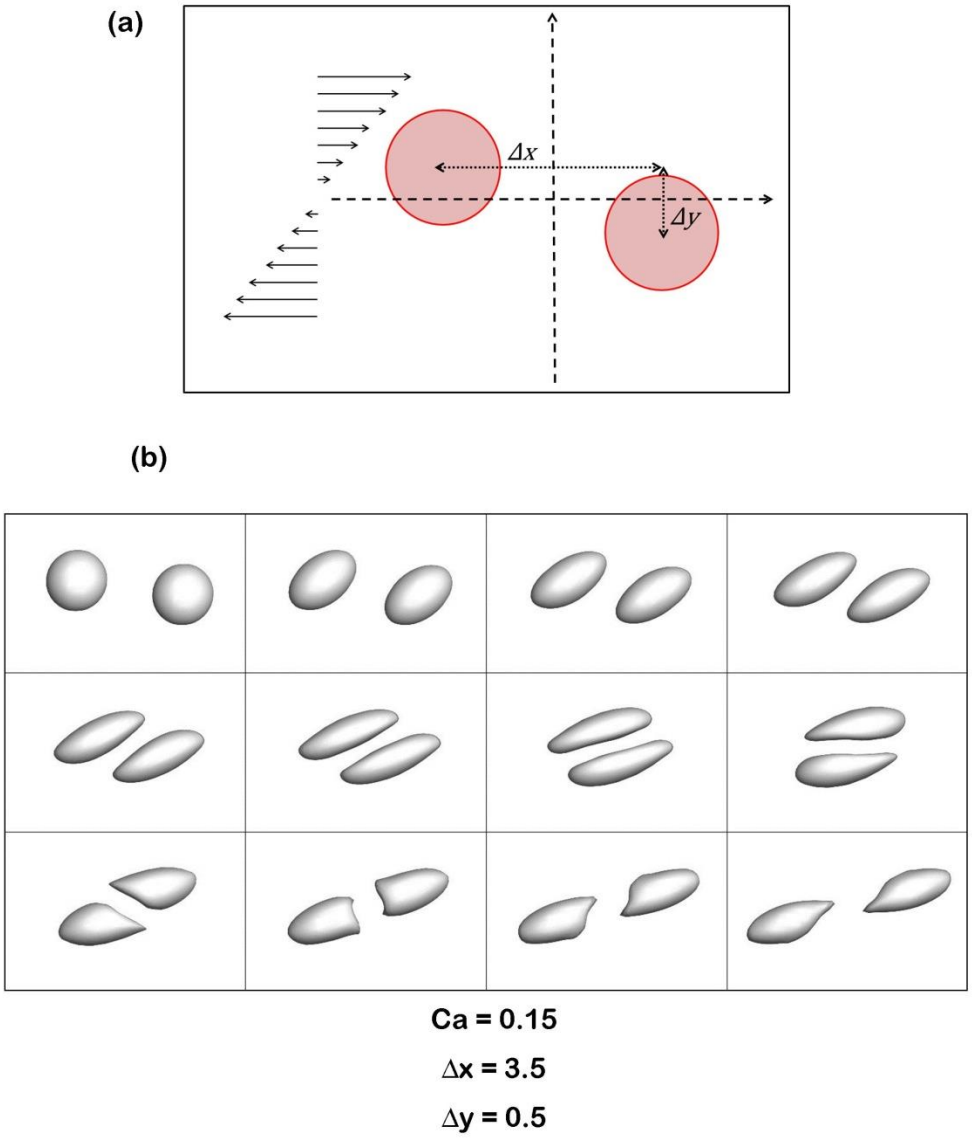

Figure 5-11: Behavior of two spheres approaching each other in linear shear flow (a) Schematic for simulating the interaction of two spheres in linear shear flow (b) stages of interaction and deformation of two identical spheres placed at a distance of $\Delta x=3.5$ and $\Delta y=0.5$ for $Ca=0.15$. The montage consists of snapshots of the positions of the spheres at equal intervals of time. The spheres approach each other, are deviated away from their original path due to the presence of the other sphere and undergo asymmetric deformation with the portion of the spheres facing each other flattening. The spheres regain their curvatures after they have passed each other.

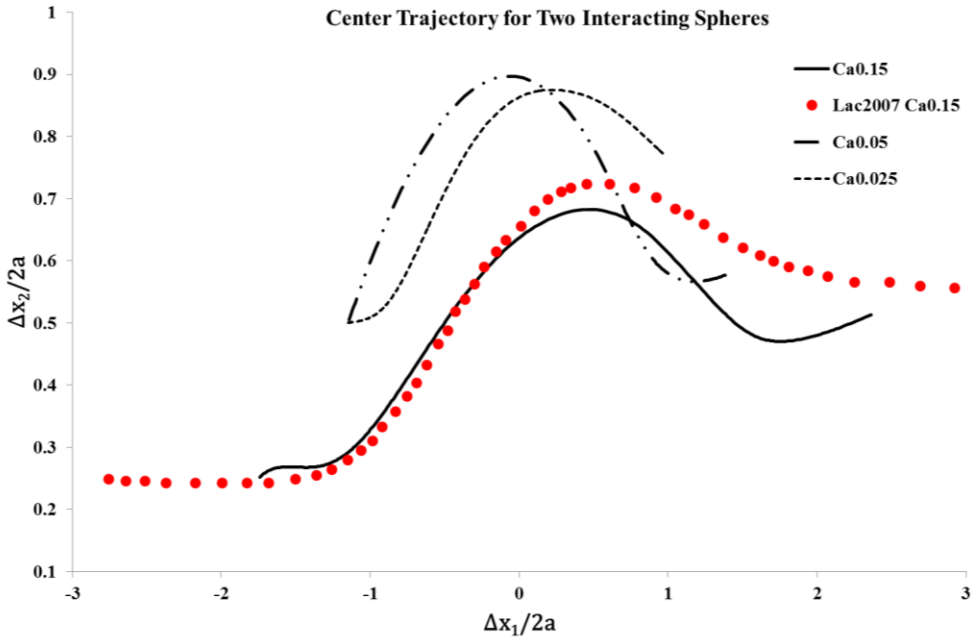

Figure 5-12: Plot of trajectory of the centers of the interacting spheres in linear shear flow. The x-axis depicts the difference in the x-locations of the two centers and the y-axis depicts the difference between the y-locations of the two centers. The center trajectories are shown for Ca = 0.025, Ca = 0.05 and Ca = 0.15 with different initial positions. Also shown is the center trajectory from [132] for Ca=0.15

CHAPTER 6

TOWARDS MODELING BLOOD FLOW: CONCLUSION AND FUTURE WORK

6.1 Introduction

The NURBS based isogoemetric analysis framework presented thus far was developed with a vision of performing simulations of ensembles of blood particulates in a novel and efficient manner. One of the many applications of this framework was to try and simulate the flow of cancer cells in the micro circulation to investigate cancer metastasis. Other potential applications directly relevant to the simulations performed so far are testing what happens to the circulatory behavior during disease states such as malaria or sickle cell anemia where the deformability of RBCs are altered. The linked list architecture enables inserting and deleting particulates from the computational domain and the immersed boundary method provides a simple yet effective means of communication between the solid and the fluid, even for multiple cells. This chapter summarizes the aforementioned capabilities and provides a perspective of the future work needed to achieve large scale simulations of blood particulates.

6.2 Summary of Capabilities Developed in Current Work

Recall the objectives of the current research from Chapter 1:

OBJ-I. To develop and validate a modeling approach that efficiently captures the complexities of individual blood cell dynamics

OBJ-II. To characterize the material properties of epithelial cancer cells in order to model ensembles of cancer cells along with blood cells

OBJ-III. To implement a cost-effective framework that captures the interactions of multiple cells

OBJ-IV. To determine how cancer cell properties impact their behavior in the circulation

6.2.1 OBJ-I: Developing a Modeling Approach to Capture Complexities of Individual Blood Cells

Simulating physiologically realistic micro-scale blood flow is a yet-to-be realized dream of researchers due to the ironically large scale of the micro-scale problem. A single drop of human blood contains over a million RBCs, not to mention WBCs and platelets. This has fostered the development of multiple methods to simulate blood particulate flows. However many of the aforementioned methods rely on finite element models of individual cells which render the system extremely computationally intensive simply because of the large number of elements per cell. The current research approaches the modeling problem from the perspective of less is more, i.e. if it is possible to use fewer elements for an individual cell then it is possible to model large number of cells with the same computational resources. With this end in mind, the NURBS based isogeometric analysis framework was developed. NURBS enables the geometric modeling of blood particulates (RBCs, WBCs, etc.) using very few elements per cell while preserving the important geometric differences across the different particulate models. Moreover, the methodology used to create the geometric models provides the foundation for performing membrane mechanics analysis, thereby enabling the creation of a holistic geometric modeling and membrane mechanics analysis system. Using the NURBS isogoemetric analysis framework, models for the characteristic biconcave RBC, spherical WBC and spherical cancer cell were created using as few as 176 elements for the sphere and 440 elements for the RBC. Moreover, the development of this framework was modular thus enabling the use of different constitutive models to describe the membrane mechanics, making it a specialized and cell-type specific framework. The development of a modular architecture was necessary as the mechanical properties of RBCs vary vastly from WBCs which in turn vary greatly from other cells in the circulation viz. platelets and cancer cells. The behavior of blood at the macro-scale is a manifestation of the characteristic behaviors of the different individual particulates at the

micro-scale, and the framework developed in this research attempts to maintain that equality with nature.

While geometrically accurate models have been developed and validated for RBCs and spherical cells, there are a few areas which can be improved. The current method used to interpolate the boundary conditions on the surface of the NURBS cell is a simple least squares approach. This can be improved with more accurate approaches to specify the boundary conditions [59]. Also, the current geometric models can be improved by testing new/updated models with improved surface knot placement to better distribute the surface mesh. The current models have a convergent pole in the center which is an impediment to the implementation of some fluid-structure interaction methodologies and also results in highly skewed meshes. Better geometric models can be developed which obviate the need of a convergent pole, thereby achieving a uniform mesh distribution over the surface of the NURBS model. The current NURBS model for blood cells is constructed with the use of a single NURBS patch, i.e. a single NURBS sheet which is bent and deformed to achieve the curvatures of the models created. Multi-patch models can also be created which could potentially remove the problems with both the convergent pole and uneven, skewed meshes. Alternately, the NURBS models can be used as a stepping stone to develop models using T-Splines [133] which enable the development of any model with an unstructured mesh having T-junctions. This could provide a way to possibly increase mesh density on the fly based on conditions like complex fluid structures, increased contact between surrounding cells, etc. The constitutive model used to describe the membrane mechanics can be improved with the use of new, advanced models which bring in an element of biochemistry along with pure mechanics [36].

6.2.2 OBJ-II: Characterization of material properties of epithelial cancer cells

Cancer is one of the world's deadliest diseases as it spreads through the human body beyond the primary stage, which makes it extremely difficult and almost impossible to combat it. This metastasizing of cancer has been a focus of researchers for years [4,134] but it is only in the past decade that work has increased on examining the mechanical properties of metastasizing cancer cells [83,135,136] to gain further insights into the physics of cancer. Like any other biological problem, the current work approaches this problem from both experimental and computational perspectives. The experimental approach was necessary in order to characterize the mechanical properties of cancer cells in the suspension and more importantly, analyzing the response of cancer cells when subjected to fluid shear stresses. This is pertinent to the metastasizing of cancer cells where they use the circulation to travel to secondary sites. Moreover, they are known to suffer from metastatic inefficiency, i.e. not all the cancer cells that enter the circulation survive [4]. Most of the studies undertaken thus far on determining mechanical properties of cancer cells were conducted on cancer cells in an adherent state using atomic force microscopy. However, in order to determine the behavior of cancer cells in circulation, the mechanical properties were needed to be obtained when the cancer cell was suspended in fluid, and not in an adhered state. Hence it was decided to undertake a secondary project to determine the mechanical properties of cancer cells in suspension using a micropipette aspiration technique. This also enabled the investigation of the effects of fluid shear on cancer cells. Using the micropipette aspiration technique, material properties of cancer cells were characterized. More importantly, the cancer cells were found to adapt to fluid shear and showed a graded or acquired response to the levels of fluid shear for the range of shear stress tested. Previous work [87] had determined that the viability of cancer cells showed a biphasic response to increasing exposure to fluid shear stress. The shear protocol involved passing the suspension of cancer cells 10 times

through a syringe pump. While a large number of cancer cells died in the initial 2-3 passes, the survival rates asymptoted off at around 50% between the 4^{th} and the 10^{th} passage, indicating adaptation of cancer cells. Our experiments on the material properties of cancer cells showed that the elastic modulus of cancer cells increased by ~80% after exposure to high shear as compared to a rest state in suspension. This increased elastic modulus was also found to be present at lower rates of shear, but the response was graded to the shear levels. Interestingly, the acquired response of stiffening was limited to transformed cells only; non-transformed cells did not show any significant change in their elastic modulus prior to and after exposure to fluid shear.

The experiments enabled initial characterization of mechanical properties of cancer cells both at rest and after exposure to fluid shear stress. Our study was the first to use *micropipette aspiration* in conjunction with fluid shear studies to examine the effects of mechanical stimuli on cancer cells in suspension. However, characterizing the elastic modulus is only the first step towards understanding the mechanics of cancer cells. The logical next step would be to examine the visco-elastic properties of the cancer cells tested thus far. This would involve upgrading the experimental setup to include a better camera and improved suction apparatus to apply increasing suction pressures in a smooth manner. There are many mechanical models that have been used to characterize the properties and behavior of living cells [72], and using an improved model than the one currently employed may shed more light on the mechanics. The use of improved models to experimentally investigate the behavior of cancer cells would translate to the use of improved models for computations. At present the cancer cell was modeled in our preliminary simulations as a membrane encapsulated capsule using an equivalent cortical tension obtained from the elastic modulus [69]. Advanced experiments would lead to the use of improved constitutive models in computations which would, in turn, shed more light on the physics of cancer metastasis.

6.2.3 OBJ-III: Implementation of a framework to model and capture the interactions of multiple cells

The simulation of a blood cell (eg.RBC) in flow is a fluid-structure interaction problem where the structure (the RBC) is influenced by the flow of the surrounding fluid; and in turn influences the surrounding fluid on account of restoring forces set up in the membrane due to deformation. Since the underlying fluid flow solver was a Cartesian solver, it was decided to use the IBM to communicate between the structure and the fluid. The main advantage of the IBM was that it would enable efficient communication between the fluid and the structure and that the principles of the method stay the same for multiple cells. This made the task of implementing architecture to model both single and multiple cells efficient and without added complexity for modeling multiple cells.

As mentioned earlier, achieving physiologically realistic simulations of blood flow is a large scale problem due to the particulate nature of blood and the extremely large number of blood cells even in a small (mL) volume of blood. In order to progress towards achieving simulations of large ensembles of blood cells, an efficient computational architecture is required. The architecture has to be efficient, dynamic and scalable in terms of number of cells and in terms of parallelization. For the purposes of this research, a linked-list based computational architecture was implemented as it fulfilled the above criteria of being dynamic, scalable and very computationally efficient. One of the many advantages of the linked list is that it is capable of dynamically allocating memory based on the distribution of computational resources unlike an array-based architecture which is not dynamic and needs a continuous chunk of memory. Moreover, the linked list architecture can handle the insertion of new cells in the computational domain and deletion of old cells from the computational domain as required. Most importantly, the linked list architecture was implemented in order to communicate with various models of meso and micro-scale in the future, where it is envisioned that a cell (eg.RBC) would pass through computational domains of meso-

scale resolution where only the general particle dynamics are required, into a region of micro-scale resolution where the cell would need to be resolved completely using the NURBS based isogeometric analysis method. This would enable efficient computations to be performed across dynamic scenarios such as a mechanical heart valve, in the region of a stent-graft, atherosclerosis, etc.

While the IBM for communication between the fluid and the solid is a good first step, it does not work very efficiently for unstructured meshes. One of the biggest advantages of using NURBS is the ability to use very few elements for a single cell. This results in meshes that are quite coarse and uneven mesh distribution over the NURBS model. The models created in the current research have a convergent pole at the center and highly skewed quad meshes closer to the pole. This presents a challenge for IBM as it results in over estimation or under estimation of the membrane force being communicated to the fluid in regions of high and low mesh density, respectively. In addition, the use of coarse meshes for the NURBS models mandate the use of very coarse meshes for the fluid domain on account of the formulation of IBM. This presents challenges especially when attempting to simulate the flow of cells in tubes having comparable of lesser diameter than the cells due to the lack of a sufficiently fine fluid mesh. More importantly, IBM does not allow for physical contact between two cells. In actuality however, the blood cells (RBCs, WBCs, platelets, etc.) experience a large number of collisions as they traverse through the circulation. In order to model and replicate the colliding nature of blood cells, a contact model has to be implemented. This was also one of the motivations for developing the NURBS based analysis method, as NURBS provides a platform for very efficient contact algorithms [45,47,137]. The ability of NURBS models to replicate the geometry and dynamics of tortuous cells with very few elements enables the contact algorithms to be very quick in searching for areas of contact between cells. The use of contact algorithms would necessitate the need to

implement other fluid-structure interaction algorithms in order to completely exploit the advantages presented by NURBS based isogeometric analysis.

6.3 Conclusion

In summary, the contributions of the current work presented in this dissertation are:

1. A novel NURBS-based isogeometric modeling and analysis procedure has been developed and implemented to model blood cells (RBCs, WBCs, platelets and cancer cells) in the micro circulation. The use of NURBS enables highly coarse meshes while preserving the important geometric features characteristic to different cells like the biconcavity of RBC, resulting in the creation of NURBS models describing the shape of the RBCs using as few as 84 elements.
2. A modular architecture has been utilized in the development of the aforementioned NURBS based architecture to enable the use of different constitutive models for different cell types, each with their own characteristics.
3. The mechanical properties of epithelial cancer cells have been characterized with a view to computationally model the behavior of cancer cells in the circulation during cancer metastasis. The micropipette aspiration technique was used to determine the elastic modulus of cancer cells at rest and after exposure to fluid shear stress. It was found that cancer cells adapted to fluid shear by stiffening themselves, and that this response was graded based on the levels of fluid shear. Moreover, this adaptation was not seen in non-transformed cells after exposure to fluid shear.

4. Fluid-structure interaction modeling was achieved through the implementation of the Immersed Boundary Method in conjunction with an in-house developed Cartesian grid fluid flow solver. The interaction method enabled simple and efficient implementation of communication between the solid and the surrounding fluid for both single and multiple cells without any additional complexity for multiple cells due to its formulation.
5. A linked-list based architecture was implemented to enable the simulation of multiple cells in a dynamic environment. The architecture was implemented using Object Oriented Programming principles which enables the inheritance of properties across various levels of hierarchy of blood cells. The linked list architecture also enables efficient use of computational resources while providing a dynamic and scalable platform to model multiple cells of various genres.
6. The NURBS models developed in this research were validated against canonical flow situations like shear flows and parabolic flow using very few NURBS elements to describe the RBC and spherical models. A parameteric study was also conducted to investigate the effect of different membrane constitutive relationships on the behavior of flowing cells. Preliminary simulations were also performed for cancer cells in flow using material properties derived from the micropipette aspiration experiments.

A schematic of the capabilities developed and implemented in this research is shown in Figure 6-1.

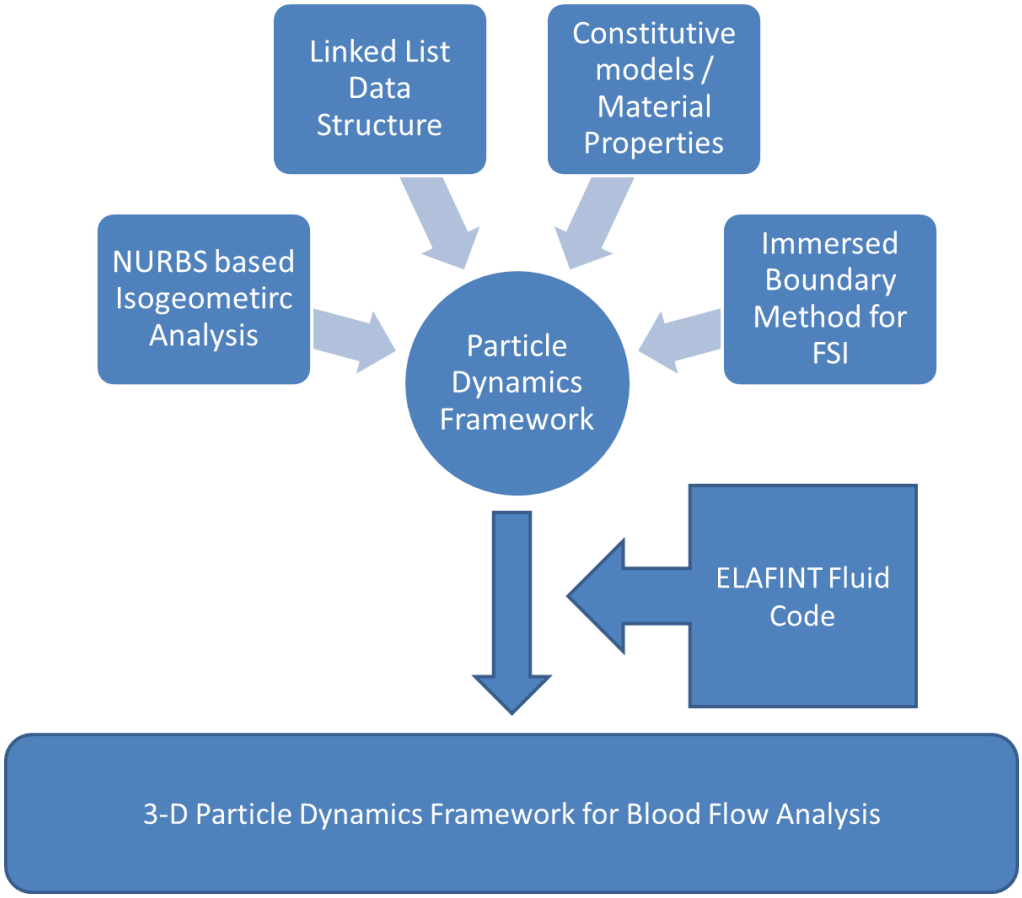

Figure 6-1: Schematic of contribution of various modules presented in this work and their contribution towards development of a 3-D particle dynamics framework for blood flow analysis

REFERENCES

[1] R. Widmaier, H. Raff, K. Strang, Vander's human physiology: the mechanisms of body function with aris, (2007).

[2] K. Chandran, S. Rittgers, A. Yoganathan, Biofluid mechanics: the human circulation, CRC Press, 2012.

[3] S. Paget, The distribution of secondary growths in cancer of the breast. 1889., Cancer Metastasis Reviews. 8 (1989) 98–101.

[4] I. Fidler, The pathogenesis of cancer metastasis: the "seed and soil"hypothesis revisited, Nat Rev Cancer. (2003).

[5] D. Bluestein, K. Chandran, K. Manning, Towards non-thrombogenic performance of blood recirculating devices, Annals of Biomedical Engineering. 38 (2010) 1236–1256.

[6] S. Einav, D. Bluestein, Dynamics of blood flow and platelet transport in pathological vessels., Annals of the New York Academy of Sciences. 1015 (2004) 351–66.

[7] S.R. Keller, R. Skalak, Motion of a tank-treading ellipsoidal particle in a shear flow, Journal of Fluid Mechanics. 120 (1982) 27–47.

[8] D. Barthes-Biesel, H. Sgaier, Role of membrane viscosity in the orientation and deformation of a spherical capsule suspended in shear flow, Journal of Fluid Mechanics. 160 (1985) 119–135.

[9] R. Fahraus, T. Lindqvist, THE VISCOSITY OF THE BLOOD IN NARROW CAPILLARY TUBES, Am J Physiol -- Legacy Content. 96 (1931) 562–568.

[10] C. Sun, L.L. Munn, Particulate nature of blood determines macroscopic rheology: a 2-D lattice Boltzmann analysis., Biophysical Journal. 88 (2005) 1635–45.

[11] P. Bagchi, Mesoscale simulation of blood flow in small vessels., Biophysical Journal. 92 (2007) 1858–77.

[12] C.S. Peskin, Numerical analysis of blood flow in the heart, Journal of Computational Physics. 25 (1977) 220–252.

[13] F. Janoschek, F. Toschi, J. Harting, Simplified particulate model for coarse-grained hemodynamics simulations, Physical Review E. 82 (2010) 056710.

[14] T. AlMomani, H.S. Udaykumar, J.S. Marshall, K.B. Chandran, Micro-scale dynamic simulation of erythrocyte-platelet interaction in blood flow., Annals of Biomedical Engineering. 36 (2008) 905–20.

[15] J. Sethian, Level set methods and fast marching methods: evolving interfaces in computational geometry, fluid mechanics, computer vision, and materials science, Cambridge University Press, 1999.

[16] S. Ramanujan, C. Pozrikidis, Deformation of liquid capsules enclosed by elastic membranes in simple shear flow: large deformations and the effect of fluid viscosities, Journal of Fluid Mechanics. 361 (1998) 117–143.

[17] a R. Pries, T.W. Secomb, P. Gaehtgens, Biophysical aspects of blood flow in the microvasculature., Cardiovascular Research. 32 (1996) 654–67.

[18] M.M. Dupin, I. Halliday, C.M. Care, L.L. Munn, Lattice Boltzmann modelling of blood cell dynamics, International Journal of Computational Fluid Dynamics. 22 (2008) 481–492.

[19] Y. Sui, Y.T. Chew, P. Roy, Y.P. Cheng, H.T. Low, Dynamic motion of red blood cells in simple shear flow, Physics of Fluids. 20 (2008) 112106.

[20] D. a Fedosov, B. Caswell, G.E. Karniadakis, A multiscale red blood cell model with accurate mechanics, rheology, and dynamics., Biophysical Journal. 98 (2010) 2215–25.

[21] C. Pozrikidis, Numerical Simulation of the Flow-Induced Deformation of Red Blood Cells, Annals of Biomedical Engineering. 31 (2003) 1194–1205.

[22] C. Pozrikidis, Modeling and Simulation of Capsules and Biological Cells (Google eBook), CRC Press, 2003.

[23] V. Cristini, G.S. Kassab, Computer modeling of red blood cell rheology in the microcirculation: a brief overview., Annals of Biomedical Engineering. 33 (2005) 1724–7.

[24] W.K. Liu, Y. Liu, D. Farrell, L. Zhang, X.S. Wang, Y. Fukui, et al., Immersed finite element method and its applications to biological systems., Computer Methods in Applied Mechanics and Engineering. 195 (2006) 1722–1749.

[25] S. Xu, Z.J. Wang, An immersed interface method for simulating the interaction of a fluid with moving boundaries, Journal of Computational Physics. 216 (2006) 454–493.

[26] R. Mittal, G. Iaccarino, Immersed Boundary Methods, Annual Review of Fluid Mechanics. 37 (2005) 239–261.

[27] T.D. AlMomani, S.C. Vigmostad, V.K. Chivukula, L. Al-zube, O. Smadi, S. BaniHani, Red Blood Cell Flow in the Cardiovascular System: A Fluid Dynamics Perspective, Critical Reviews™ in Biomedical Engineering. 40 (2012) 427–440.

[28] D. Barthès-Biesel, Motion of a spherical microcapsule freely suspended in a linear shear flow, Journal of Fluid Mechanics. 100 (1980) 831–853.

[29] D. Barthès-Biesel, J.M. Rallison, The time-dependent deformation of a capsule freely suspended in a linear shear flow, Journal of Fluid Mechanics. 113 (1981) 251–267.

[30] C.D. Eggleton, a. S. Popel, Large deformation of red blood cell ghosts in a simple shear flow, Physics of Fluids. 10 (1998) 1834.

[31] S. Doddi, P. Bagchi, Three-dimensional computational modeling of multiple deformable cells flowing in microvessels, Physical Review E. 79 (2009) 1–14.

[32] W.K. Liu, Y. Liu, D. Farrell, L. Zhang, X.S. Wang, Y. Fukui, et al., Immersed finite element method and its applications to biological systems., Computer Methods in Applied Mechanics and Engineering. 195 (2006) 1722–1749.

[33] L. Zhang, A. Gerstenberger, X. Wang, W.K. Liu, Immersed finite element method, Computer Methods in Applied Mechanics and Engineering. 193 (2004) 2051–2067.

[34] W.R. Dodson, P. Dimitrakopoulos, Tank-treading of erythrocytes in strong shear flows via a nonstiff cytoskeleton-based continuum computational modeling., Biophysical Journal. 99 (2010) 2906–16.

[35] R. Skalak, A. Tozeren, R.P. Zarda, S. Chien, Strain energy function of red blood cell membranes., Biophysical Journal. 13 (1973) 245–64.

[36] T. Klöppel, W.A. Wall, A novel two-layer, coupled finite element approach for modeling the nonlinear elastic and viscoelastic behavior of human erythrocytes., Biomechanics and Modeling in Mechanobiology. 10 (2011) 445–59.

[37] E. Lac, D. Barthès-Biesel, N. a. Pelekasis, J. Tsamopoulos, Spherical capsules in three-dimensional unbounded Stokes flows: effect of the membrane constitutive law and onset of buckling, Journal of Fluid Mechanics. 516 (2004) 303–334.

[38] M. Dao, C.T. Lim, S. Suresh, Mechanics of the human red blood cell deformed by optical tweezers, Journal of the Mechanics and Physics of Solids. 51 (2003) 2259–2280.

[39] T.J.R. Hughes, J. a. Cottrell, Y. Bazilevs, Isogeometric analysis: CAD, finite elements, NURBS, exact geometry and mesh refinement, Computer Methods in Applied Mechanics and Engineering. 194 (2005) 4135–4195.

[40] L. Peigl, W. Tiller, THE NURBS BOOK, Springer, 1997.

[41] M. Šuleji, B-spline and NURBS Curves, (2011).

[42] Y. Bazilevs, V.M. Calo, Y. Zhang, T.J.R. Hughes, Isogeometric Fluid–structure Interaction Analysis with Applications to Arterial Blood Flow, Computational Mechanics. 38 (2006) 310–322.

[43] Y. Zhang, Y. Bazilevs, S. Goswami, C.L. Bajaj, T.J.R. Hughes, Patient-Specific Vascular NURBS Modeling for Isogeometric Analysis of Blood Flow., Computer Methods in Applied Mechanics and Engineering. 196 (2007) 2943–2959.

[44] J. Lu, Circular element: Isogeometric elements of smooth boundary, Computer Methods in Applied Mechanics and Engineering. 198 (2009) 2391–2402.

[45] J. Lu, Isogeometric contact analysis: Geometric basis and formulation for frictionless contact, Computer Methods in Applied Mechanics and Engineering. 200 (2011) 726–741.

[46] J. Lu, G. Yang, J. Ge, Blending NURBS and Lagrangian representations in isogeometric analysis, Computer Methods in Applied Mechanics and Engineering. 257 (2013) 117–125.

[47] İ. Temizer, P. Wriggers, T.J.R. Hughes, Contact treatment in isogeometric analysis with NURBS, Computer Methods in Applied Mechanics and Engineering. 200 (2011) 1100–1112.

[48] J.A. Cottrell, T.J.R. Hughes, Y. Bazilevs, Isogeometric Analysis, (2009).

[49] X. Zhou, J. Lu, NURBS-Based Galerkin Method and Application to Skeletal Muscle Modeling, 1 (2005) 71–78.

[50] I. V Pivkin, G.E. Karniadakis, Accurate Coarse-Grained Modeling of Red Blood Cells, 118105 (2008) 1–4.

[51] J.P. Mills, L. Qie, M. Dao, C.T. Lim, S. Suresh, Nonlinear elastic and viscoelastic deformation of the human red blood cell with optical tweezers., Mechanics & Chemistry of Biosystems : MCB. 1 (2004) 169–80.

[52] W. Ma, J. Kruth, Parameterization of randomly measured points for least squares fitting of B-spline curves and surfaces, Computer-Aided Design. 27 (1995) 663–675.

[53] W. Ma, P. He, B-spline surface local updating with unorganized points, Computer-Aided Design. 30 (1998) 853–862.

[54] D. Brujic, M. Ristic, I. Ainsworth, Measurement-based modification of NURBS surfaces, Computer-Aided Design. 34 (2002) 173–183.

[55] S.-M. Hu, Y.-F. Li, T. Ju, X. Zhu, Modifying the shape of NURBS surfaces with geometric constraints, Computer-Aided Design. 33 (2001) 903–912.

[56] J.H. Ferziger, M. Peric, Computational Methods for Fluid Dynamics, Springer, 2013.

[57] E. a Evans, R. Waugh, L. Melnik, Elastic area compressibility modulus of red cell membrane., Biophysical Journal. 16 (1976) 585–95.

[58] T. Belytschko, W.K. Liu, B. Moran, Nonlinear Finite Elements for Continua and Structures, Wiley, 2000.

[59] P. Costantini, C. Manni, F. Pelosi, M.L. Sampoli, Quasi-interpolation in isogeometric analysis based on generalized B-splines, Computer Aided Geometric Design. 27 (2010) 656–668.

[60] I. Pivkin, G. Karniadakis, Accurate Coarse-Grained Modeling of Red Blood Cells, Physical Review Letters. 101 (2008) 1–4.

[61] Y.C. Fung, Biomechanics: Mechanical Properties of Living Tissues, Second Edition, Springer, 1993.

[62] E. Evans, Y.C. Fung, Improved measurements of the erythrocyte geometry., Microvascular Research. 4 (1972) 335–47.

[63] E. a Evans, R.M. Hochmuth, Membrane viscoelasticity., Biophysical Journal. 16 (1976) 1–11.

[64] E. Evans, a Yeung, Apparent viscosity and cortical tension of blood granulocytes determined by micropipet aspiration., Biophysical Journal. 56 (1989) 151–60.

[65] R. Waugh, E.A. Evans, Thermoelasticity of red blood cell, 26 (1979) 115–131.

[66] R.P. Rand, a. C. Burton, Mechanical Properties of the Red Cell Membrane, Biophysical Journal. 4 (1964) 115–135.

[67] R.M. Hochmuth, N. Mohandas, P.L. Blackshear, Measurement of the elastic modulus for red cell membrane using a fluid mechanical technique., Biophysical Journal. 13 (1973) 747–62.

[68] E. Widmaier, H. Raff, K. Strang, Vander's human physiology: the mechanisms of human body function, McGraw-Hill, 2006.

[69] R.M. Hochmuth, Micropipette aspiration of living cells., Journal of Biomechanics. 33 (2000) 15–22.

[70] C. Dong, R. Skalak, K.-L.P. Sung, G.W. Schmid-Schönbein, S. Chien, Passive Deformation Analysis of Human Leukocytes, Journal of Biomechanical Engineering. 110 (1988) 27.

[71] D. Needham, R.M. Hochmuth, A sensitive measure of surface stress in the resting neutrophil Cell preparation, 61 (1992).

[72] C.T. Lim, E.H. Zhou, S.T. Quek, Mechanical models for living cells--a review., Journal of Biomechanics. 39 (2006) 195–216.

[73] M. Radmacher, M. Fritz, C.M. Kacher, J.P. Cleveland, P.K. Hansma, Measuring the viscoelastic properties of human platelets with the atomic force microscope, Biophysical Journal. 70 (1996) 556–567.

[74] H. Zhao, E.S.G. Shaqfeh, V. Narsimhan, Shear-induced particle migration and margination in a cellular suspension, Physics of Fluids. 24 (2012) 011902.

[75] T.M. Fischer, C.W. Haest, M. Stöhr-Liesen, H. Schmid-Schönbein, R. Skalak, The stress-free shape of the red blood cell membrane., Biophysical Journal. 34 (1981) 409–22.

[76] H. Kan, H.S. Udaykumar, W. Shyy, R. Tran-son-tay, Hydrodynamics of a compound drop with application to leukocyte modeling Hydrodynamics of a compound drop with application to leukocyte modeling, 760 (1998).

[77] C. Dong, J. Cao, E. Struble, H. Lipowsky, Mechanics of Leukocyte Deformation and Adhesion to Endothelium in Shear Flow, Anna. 27 (1999) 298–312.

[78] S. V. Marella, H.S. Udaykumar, Computational analysis of the deformability of leukocytes modeled with viscous and elastic structural components, Physics of Fluids. 16 (2004) 244.

[79] D. Barthès-Biesel, A. Diaz, E. Dhenin, Effect of constitutive laws for two-dimensional membranes on flow-induced capsule deformation, Journal of Fluid Mechanics. 460 (2002) 211–222.

[80] E.C. Faria, N. Ma, E. Gazi, P. Gardner, M. Brown, N.W. Clarke, et al., Measurement of elastic properties of prostate cancer cells using AFM., The Analyst. 133 (2008) 1498–500.

[81] S.E. Cross, Y.-S. Jin, J. Tondre, R. Wong, J. Rao, J.K. Gimzewski, AFM-based analysis of human metastatic cancer cells., Nanotechnology. 19 (2008) 384003.

[82] D. Wirtz, K. Konstantopoulos, P.C. Searson, The physics of cancer: the role of physical interactions and mechanical forces in metastasis., Nature Reviews. Cancer. 11 (2011) 512–22.

[83] S. Kumar, V.M. Weaver, Mechanics, malignancy, and metastasis: the force journey of a tumor cell., Cancer Metastasis Reviews. 28 (2009) 113–27.

[84] V. Thamilselvan, M.D. Basson, Pressure activates colon cancer cell adhesion by inside-out focal adhesion complex and actin cytoskeletal signaling, Gastroenterology. 126 (2004) 8–18.

[85] V. Thamilselvan, D.H. Craig, M.D. Basson, FAK association with multiple signal proteins mediates pressure-induced colon cancer cell adhesion via a Src-dependent PI3K/Akt pathway., FASEB Journal : Official Publication of the Federation of American Societies for Experimental Biology. 21 (2007) 1730–41.

[86] A. von Sengbusch, P. Gassmann, K.M. Fisch, A. Enns, G.L. Nicolson, J. Haier, Focal adhesion kinase regulates metastatic adhesion of carcinoma cells within liver sinusoids., The American Journal of Pathology. 166 (2005) 585–96.

[87] J.M. Barnes, J.T. Nauseef, M.D. Henry, Resistance to fluid shear stress is a conserved biophysical property of malignant cells., PloS One. 7 (2012) e50973.

[88] A.L. Weisenhorn, M. Khorsandi, S. Kasas, V. Gotzos, H.-J. Butt, Deformation and height anomaly of soft surfaces studied with an AFM, Nanotechnology. 4 (1993) 106–113.

[89] J. Dai, The Secretion-coupled Endocytosis Correlates with Membrane Tension Changes in RBL 2H3 Cells, The Journal of General Physiology. 110 (1997) 1–10.

[90] J.M. MITCHISON, M.M. SWANN, The Mechanical Properties of the Cell Surface: I. The Cell Elastimeter, J. Exp. Biol. 31 (1954) 443–460.

[91] R.P. Rand, a C. Burton, Mechanical Properties of the Red Cell Membrane. I. Membrane Stiffness and Intracellular Pressure., Biophysical Journal. 4 (1964) 115–35.

[92] F. Guilak, W.R. Jones, H.P. Ting-Beall, G.M. Lee, The deformation behavior and mechanical properties of chondrocytes in articular cartilage., Osteoarthritis and Cartilage / OARS, Osteoarthritis Research Society. 7 (1999) 59–70.

[93] D.P. Theret, M.J. Levesque, M. Sato, R.M. Nerem, L.T. Wheeler, The application of a homogeneous half-space model in the analysis of endothelial cell micropipette measurements., Journal of Biomechanical Engineering. 110 (1988) 190–9.

[94] D.B. Agus, J.F. Alexander, W. Arap, S. Ashili, J.E. Aslan, R.H. Austin, et al., A physical sciences network characterization of non-tumorigenic and metastatic cells., Scientific Reports. 3 (2013) 1449.

[95] L.M. Rebelo, J.S. de Sousa, J. Mendes Filho, M. Radmacher, Comparison of the viscoelastic properties of cells from different kidney cancer phenotypes measured with atomic force microscopy., Nanotechnology. 24 (2013) 055102.

[96] S.E. Cross, Y.-S. Jin, J. Rao, J.K. Gimzewski, Nanomechanical analysis of cells from cancer patients., Nature Nanotechnology. 2 (2007) 780–3.

[97] I. Zeidman, Fate of Circulating Tumor Cells III. Comparison of Metastatic Growth Produced by Tumor Cell Emboli in Veins and Lymphatics, Cancer Research. (1965).

[98] I. Zeidman, M. McCutcheon, D. Coman, Factors affecting the number of tumor metastases experiments with a transplantable mouse tumor, Cancer Research. (1950).

[99] I. Zeidman, Metastasis: a review of recent advances, Cancer Research. (1957).

[100] R. Kalluri, R.A. Weinberg, The basics of epithelial-mesenchymal transition., The Journal of Clinical Investigation. 119 (2009) 1420–8.

[101] C.L. Chaffer, R.A. Weinberg, A perspective on cancer cell metastasis., Science (New York, N.Y.). 331 (2011) 1559–64.

[102] J.P. Thiery, J.P. Sleeman, Complex networks orchestrate epithelial-mesenchymal transitions., Nature Reviews. Molecular Cell Biology. 7 (2006) 131–42.

[103] A.M. Malek, Hemodynamic Shear Stress and Its Role in Atherosclerosis, JAMA. 282 (1999) 2035.

[104] T.W. Secomb, B. Styp-Rekowska, A.R. Pries, Two-dimensional simulation of red blood cell deformation and lateral migration in microvessels., Annals of Biomedical Engineering. 35 (2007) 755–65.

[105] C.S. Peskin, The immersed boundary method, Acta Numerica. 11 (2003) 479–517.

[106] S.O. Unverdi, G. Tryggvason, A Front-Tracking Method for Viscous , Incompressible , Multi-fluid Flows, Journal of Computational Physics. 100 (1992) 25–37.

[107] W. Yue, C.-L. Lin, V.C. Patel, Numerical simulation of unsteady multidimensional free surface motions by level set method, International Journal for Numerical Methods in Fluids. 42 (2003) 853–884.

[108] J. Mousel, A massively parallel adaptive sharp interface solver with application to mechanical heart valve simulations, The University of Iowa, 2012.

[109] E. Lac, D. Barthès-biesel, Deformation of a capsule in simple shear flow : Effect of membrane prestress Deformation of a capsule in simple shear flow : Effect of membrane prestress, Physics of Fluids. 17 (2005) 072105.

[110] S.K. Doddi, P. Bagchi, Lateral migration of a capsule in a plane Poiseuille flow in a channel, International Journal of Multiphase Flow. 34 (2008) 966–986.

[111] Q. Queguiner, D. Barthes-Biesel, Flow of capsules into small pores, Transactions on Modelling and Simulation. 10 (1995).

[112] C. Quéguiner, D. Barthès-Biesel, Axisymmetric motion of capsules through cylindrical channels, Journal of Fluid Mechanics. 348 (1997) 349–376.

[113] J. Zhang, P.C. Johnson, A.S. Popel, Effects of erythrocyte deformability and aggregation on the cell free layer and apparent viscosity of microscopic blood flows, Microvascular Research. 77 (2009) 265–272.

[114] a R. Pries, D. Neuhaus, P. Gaehtgens, Blood viscosity in tube flow: dependence on diameter and hematocrit., The American Journal of Physiology. 263 (1992) H1770–8.

[115] X. Gong, K. Sugiyama, S. Takagi, Y. Matsumoto, The deformation behavior of multiple red blood cells in a capillary vessel., Journal of Biomechanical Engineering. 131 (2009) 074504.

[116] F. Risso, F. Collé-Paillot, M. Zagzoule, Experimental investigation of a bioartificial capsule flowing in a narrow tube, Journal of Fluid Mechanics. 547 (2006) 149.

[117] C. Pozrikidis, Axisymmetric motion of a file of red blood cells through capillaries, Physics of Fluids. 17 (2005) 031503.

[118] G.Y.H. Lee, C.T. Lim, Biomechanics approaches to studying human diseases., Trends in Biotechnology. 25 (2007) 111–8.

[119] N. Mohandas, J.A. Chasis, S.B. Shohet, The influence of membrane skeleton on red cell deformability, membrane material properties, and shape., Seminars in Hematology. 20 (1983) 225–42.

[120] P.P. Klug, Rheological Aspects of Sickle Cell Disease, Archives of Internal Medicine. 133 (1974) 577.

[121] E. Lac, D. Barthès-Biesel, Deformation of a capsule in simple shear flow: Effect of membrane prestress, Physics of Fluids. 17 (2005) 072105.

[122] D. Wang, J. Xuan, An improved NURBS-based isogeometric analysis with enhanced treatment of essential boundary conditions, Computer Methods in Applied Mechanics and Engineering. 199 (2010) 2425–2436.

[123] A.K. Chakroborty, T.C. Ho, S.M. Hosseini, J.J. Feng, A particle-based model for the transport of erythrocytes in capillaries, Chemical Engineering Science. 64 (2009) 4488–4497.

[124] J.K.W. Chesnutt, J.S. Marshall, Effect of particle collisions and aggregation on red blood cell passage through a bifurcation, Microvascular Research. 78 (2009) 301–313.

[125] J. Zhang, P.C. Johnson, A.S. Popel, Red blood cell aggregation and dissociation in shear flows simulated by lattice Boltzmann method, Journal of Biomechanics. 41 (2008) 47–55.

[126] P. Bagchi, P.C. Johnson, A.S. Popel, Computational Fluid Dynamic Simulation of Aggregation of Deformable Cells in a Shear Flow, Journal of Biomechanical Engineering. 127 (2005) 1070.

[127] C. Pozrikidis, Effect of membrane bending stiffness on the deformation of capsules in simple shear flow, Journal of Fluid Mechanics. 440 (2001) 269–291.

[128] C. Pozrikidis, Numerical Simulation of Cell Motion in Tube Flow, Annals of Biomedical Engineering. 33 (2005) 165–178.

[129] M. Dupin, I. Halliday, C. Care, L. Alboul, L. Munn, Modeling the flow of dense suspensions of deformable particles in three dimensions, Physical Review E. 75 (2007) 066707.

[130] L.L. Munn, M.M. Dupin, Blood cell interactions and segregation in flow., Annals of Biomedical Engineering. 36 (2008) 534–44.

[131] H. Noguchi, G. Gompper, Shape transitions of fluid vesicles and red blood cells in capillary flows., Proceedings of the National Academy of Sciences of the United States of America. 102 (2005) 14159–64.

[132] E. Lac, A. Morel, D. Barthès-Biesel, Hydrodynamic interaction between two identical capsules in simple shear flow, Journal of Fluid Mechanics. 573 (2007) 149.

[133] Y. Bazilevs, V.M. Calo, J.A. Cottrell, J.A. Evans, T.J.R. Hughes, S. Lipton, et al., Isogeometric analysis using T-splines, Computer Methods in Applied Mechanics and Engineering. 199 (2010) 229–263.

[134] C.L. Chaffer, R.A. Weinberg, A perspective on cancer cell metastasis., Science (New York, N.Y.). 331 (2011) 1559–64.

[135] E.C. Faria, N. Ma, E. Gazi, P. Gardner, M. Brown, W. Clarke, et al., Measurement of elastic properties of prostate cancer cells using AFM, (2008) 1498–1500.

[136] M. Manimaran, F.E.H. Tay, K.C. Chaw, Cell Deformation in Cancer Metastasis: a BioMEMS Based Approach, Journal of Physics: Conference Series. 34 (2006) 1143–1147.

[137] İ. Temizer, P. Wriggers, T.J.R. Hughes, Three-dimensional mortar-based frictional contact treatment in isogeometric analysis with NURBS, Computer Methods in Applied Mechanics and Engineering. 209-212 (2012) 115–128.